博士論文

Wireless Power Transfer for Moving Electric Vehicles

（走行中電気自動車への給電をめざした
ワイヤレス電力伝送）

コー　キム　エン
Koh Kim Ean

Abstract

This thesis focuses on designing and evaluating various wireless power transfer design for charging while moving of electric vehicles. Vehicle electrification has become a recognized solution to oil shortage and pollution problems from engine-driven vehicle. Electric vehicles are also cleaner, quiet and more energy efficient. Renewable energy sources can be used especially with the recent development of distributed energy system. However, energy storage is a bottleneck for rapid development and wide adoption of electric vehicles. Batteries for supporting the same or close to the driving range of drivers used to enjoy are costly, heavy and with long charging time.

Wireless power transfer alleviates above mentioned problems by providing a safer and more convenient charging method compared to plug-in charging. For charging while parking, the wireless charging facility is more durable, space saving and does not pollute the city view with overhead electricity grid. Current development of wireless power transfer technology enables the possibility of dynamic charging on highways and roads. The wireless power transfer system is constructed to support certain distance and vehicles pick up power while moving along the road. The challenges of constructing the system include complexity of the wireless powering network underneath the ground, cost, transfer gap, efficiency and power levels.

In this work, wireless power transfer configurations which consist of combination of multi-receiver and repeaters are proposed for dynamic charging. Power division method between receivers with different amount of coupling to the transmitters is proposed. On the other hand, repeaters are also used in a system to extend the effective range. New methods

for power division and impedance matching are derived and then generalized for arbitrary number of receivers and repeaters including cross coupling consideration. Impedance inverter representation is used to simplify the analysis and calculation. Additionally, a special case where the existence of repeaters causes dead zone is analyzed. The simplicity of using impedance inverter representation compared to only solving conventional equivalent circuit equations is further demonstrated in the analysis of this special case. All the methods proposed are validated using simulations and experiments.

Above mentioned work generalized the analysis of wireless power transfer using impedance inverter representations of coupling for arbitrary combinations of receiver and repeaters. Using this theory as basis, a dynamic charging system using two transmitters simultaneously powering a receiver to achieve even magnetic field and therefore constant power level during running is proposed. Mutual inductance is calculated using Neumann formula. Maximum efficiency depends on the ratio of mutual inductance to the coil resistance if the frequency is fixed. When using long transmitters, the mutual inductance is similar to using short transmitters but the coil resistance is larger. Therefore multiple short transmitters are connected in parallel to the power source via impedance inverter circuit is proposed. The coupling design which depends on the size and turns of the transmitters, and receiver size determines the power level. Spacing between transmitters is also designed to achieve even magnetic field. Additionally, cross coupling between the transmitters does not affect the power level due to the impedance inverter circuit. The hardware setup for this even magnetic field system including the transmitter module, the receiver module and the magnetic sensors for sensing the position of the receiver is shown in the last chapter.

In the next chapter, the steady state and transient analysis of one-to-one wireless power transfer are discussed. In series-series compensated wireless power transfer, the maximum efficiency depends on both the receiver and the transmitter. However the maximum power depends dominantly on the transmitter. This characteristic is exploited to achieve a flatter efficiency curve across different power levels as different power is required when the vehicle is at different moving speeds. A design flow is then proposed using efficiency vs. power level curve. The design method is discussed using round spiral coils and the

AC resistance is approximated using extended Dowell formula. However the method can be applied to other coils once the AC resistance calculation method is developed. The transient of the wireless power transfer is then studied using general state space averaging (GSSA).

Acknowledgements

Firstly, I would like to express my deepest gratitude to Professor Yoichi Hori who supervised and supported me throughout my master and PhD course. From him, I have learned the skills, not only in the technical aspects but also interpersonal skills. I received my training as a researcher throughout my years in Hori-Fujimoto laboratory, from having an interest to know, to finding the research direction, performing the investigation till sharing the new knowledge via writings and presentations.

Secondly, I would like to thank Professor Hiroshi Fujimoto who always has the insights into research directions. He is also the teacher who is willing to spend hours with students and guide them from the big picture down to the tiniest variable in an equation. I am truly fortunate to be able to receive guidance from both Professor Hori and Professor Fujimoto who always prioritize their time for the students.

Of course, I cannot omit thanking Professor Takehiro Imura in successfully completing this dissertation. I first started working with him when he was a post-doctoral researcher and now he is an assistance professor who is leading a large and successful team researching wireless power transfer in this laboratory. He is kind and fair, not to mention always providing tireless help and guidance for all students despite of his busy schedule.

I want to thank all the members of Hori-Fujimoto laboratory. You are the one who made my time here worthwhile. The endless discussion inspired many ideas. I would also like to convey my special thanks to Professor Kai Song who worked with me during my final year of my PhD course.

Also I would like to express my appreciation to Professor Takafumi Koseki, Akira Hirose, Makoto Takamiya and Yoshihiro Kawahara of the University of Tokyo who are the members of the judging committee of my doctoral degree together with Professor Yoichi

Contents

List of Figures

List of Tables

Chapter 1

Introduction

This dissertation aims at developing theory of wireless power transfer network which consists of arbitrary number of coils and application to the dynamic charging system.

In this chapter, research backgrounds of related theories and applications of wireless power transfer are first introduced. Then, motivations of this research are explained. The outline of this dissertation is then provided in the last section.

1.1   Research Background

The idea of using wireless power transfer was first conceived and explored in 1899 by Nikola Tesla [1]. His experiment in Colorado Springs consists of a gigantic coil in a large square building which rose a 60 m mast with a 1 m diameter copper ball at the top. The coil was resonated at frequency of 150 kHz and 300 kW power was fed to the mast. RF potential approaching 100, 000, 000 V was produced on the sphere. Fast forward to not too long ago, in year 2007, Witricity team from Massachusetts Institute of Technology demonstrated wireless power transfer based on near field and magnetic resonance is able to transfer power across mid-range gap, which is a distance of one-time up a to few-times the diameter of the coils [2, 3]. Fig. 1.1 shows the team positioned themselves between the experimental source coil and the power receiver coil as 60 watts of power are being safely transferred across a distance of 2.5 m to illuminate the light bulb. The demonstration generates a wave of interest in wireless power transfer technology due to practicality for current

Figure 1.1: Witricity team positioned themselves in a wireless power transfer demonstration [4].

and near future applications. Due to electrical grid is able to transport electricity almost everywhere, medium range wireless power transfer would have many new applications in homes, factories, and public facilities. Some examples including charging portable devices [5]-[7], powering medical implantable devices [8]-[10], position sensing [11], power supply in remote locations using aerial vehicles [12], power supply for underground nuclear waste storage to achieve complete isolation [13]-[15], factory automation [16]-[18] and charging electric vehicles [19]-[22].

Coupled mode theory [2, 3] was proposed to model the wireless power transfer system. The power transfer medium is omnidirectional but stationary or non-lossy near field. Medium range wireless power transfer can be achieved if the system is designed to operate in a regime of "strong coupling" where the coupling rate is much faster than the loss rate in terms of coupled mode theory. Coils are conductive loops of high quality factors and capacitive-loaded to achieve resonance. When a resonator is excited by a power source, cyclic energy exchange occurs from the electric field inside the capacitor, due to voltage across it, and to the magnetic field in free space, due to the current in the wire. If the resonator is ideal, energy is driven back into the source with no loss [2, 23]. When a receiver with a load is placed nearby, energy can be transferred to the load via magnetic field. This reactive near field responds to coupled loads and does not radiate energy to the free space due to the size of resonator coils used are usually less than 0.1 wavelength of the electromagnetic field [24]. Therefore, by controlling the impedance, the amount of power

extracted by the load can be controlled. Equivalent circuit model which is in terms of voltage, current and impedance can also be used to model the wireless power transfer which can be approximated as lumped element model. Using equivalent circuit model [25], various wireless power transfer configurations are studied for example using repeaters [26] to extend the transfer distance and multiple receivers [27, 28] to transfer power to multiple loads simultaneously. Transfer equations are complex and the wireless power transfer phenomena is difficult to be analyzed [29, 30]. Band-pass filter representation [31, 32] is then proposed. The design equations are simple even with many repeaters. The model however cannot be applied to multiple receivers. Furthermore, all the gaps between resonators need to be controllable. Efficiency analysis and tuning algorithm for multiple receivers can be found in [5, 27, 28]. In Chapter 2 and Chapter 3 of this work, new methods for power division and impedance matching are derived and then generalized for arbitrary number of receivers and repeaters including cross coupling consideration. Impedance inverter representation is used to simplify the analysis and calculation. Analysis of a special case where the repeater causes dead zone is also included. The simplicity of using impedance inverter representation compared to only solving conventional equivalent circuit equations is further demonstrated in the analysis of this special case.

The research and development of wireless power transfer for electric vehicles has gain the fastest traction compared to other applications. Growing world population and urbanization has increased the number of vehicles on the road. Electrification of vehicles reduces environmental pollution and relaxes oil depletion issues. However, heavy on-board battery storage and long charging times remain as barriers. The benefits of using wireless power transfer include mobility, safety, high reliability and low maintenance. For EV applications, the operating frequencies are typically in several tens of kilohertz. For ease of use, tolerance of misalignment and large transfer gap are needed between the transmitter and receivers. The coupling strength is therefore small to achieve transfer distance comparable to the coil diameter. Compensation circuits are then used to achieve resonance and desired power at high efficiency can be transferred. The equivalent circuit modeling is therefore similar with magnetic resonant coupling method, except that only the operating frequency is in kilohertz range. There are four basic compensation topologies [33] for primary and

secondary sides: SS compensation, SP compensation, PP compensation and PS compensation, where S denotes series connection of the coil with the capacitor and P denotes parallel connection of the coil with the capacitor. SS compensation capacitors do not depends on the mutual inductance and effective load and therefore is suitable for many applications [34, 35]. SS compensation has inverting characteristic, that is if the load has high resistance, the reflected impedance seen by the power supply will be low and more current will be drawn from a constant voltage source supply. As the resistance reduces, the current drawn is reduced when the load is taken away, the series compensated transmitter acts like a short circuit to the power supply. In order to mitigate this issue, a more advanced compensation technique, impedance inverter [36, 37] circuit is used at the transmitter side. This way, not only the reactive power is compensated, the current in the transmitter is also constant regardless of the mutual inductance and load resistance. The power drawn from the power supply increases when the receiver is closer and the load resistance is smaller.

Wireless power transfer has been researched since 30 years ago for charging electric vehicles [38]. The power transmitter portion is composed of an inverter to convert DC power into the operating frequency, 85 kHz, which is the frequency proposed by Society of Automotive Engineers for electric vehicle usage [39]. The power receiver portion is comprised of pick-up module, rectifier and regulator. The pick-up module receives power via magnetic flux from the transmitter, the rectifier converts AC power to DC power. In dynamic charging, regulator controls the output voltage which is supplying to the motors and batteries. Some of the transferred power is used to drive the motors and the remainder is used to charge the batteries. During static charge, all of the power is used to charge the batteries. Several aspects of WPT have been studied, such as magnetic coupler design techniques, compensation topologies, control methods, foreign object detection algorithms, and the radiation safety issues [40]. In this work, coupler design and impedance inverter compensation method for configuration of multiple coils are studied for dynamic charging.

1.2 Wireless Power Transfer while Stopping

Electric vehicles (EV) are cleaner, quieter and more efficient compared to internal combustion engine vehicles. Although the initial purchase cost is higher, price per distance
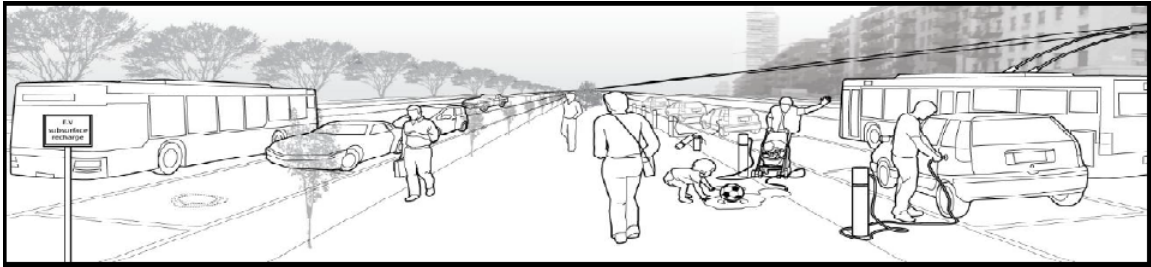
Figure 1.2: Comparison between wireless charging and wired charging [41].

traveled is significantly lower for EVs considering the difference between the electricity and gasoline price. Using EVs is therefore more cost effective. Furthermore, with the advancement of wireless power transfer, the requirement for high storage batteries will be relaxed and thus the price will be even more competitive. More importantly, the energy for EVs can be generated from renewable sources such as solar power and wind power. With the development of distributed systems, these renewable energy generators can be located close to the charging facilities and provide energy for electric vehicles.

On the other hand, contactless charging increases ease of use and safety for EV users. Instead of depleting the battery storage energy, the vehicle battery can be topped off frequently while parked at home or at work, when shopping and at traffic lights. Cables and cords are eliminated, so as the range anxiety of the users. As shown in Fig. 1.2, the plugged in charging facilities include the risk of vandalism and added clutter in an urban environment. Wireless charging facility is safer, more durable, save space and does not pollute the view with cables. Frequent charge in between usages is also possible in this mode of charging. Example of currently available wireless charge module is shown in Fig. 1.3. HaloIPT, a New Zealand based company acquired by Qualcomm Incorporated, also produced a 7 kW charger for Rolls Royce Phantom 102 Ex experimental EV and Delta EV. The PLUGLESS system offered by Evatran and Bosch provides 3.3 kW wireless charge for Nissan Leaf and Chevrolet Volt.

The input power to the system is usually either from the AC mains which is converted to DC in an AC/DC rectifier block, or alternatively, a DC voltage directly from a battery or other DC supply. In high power applications a power factor correction stage may also be included in this block. A high efficiency switching amplifier converts the DC voltage into

Figure 1.3: Halo IPT charging pad [42].

Figure 1.4: Online electric vehicle (OLEV) tram in Seoul Grand Park [43].

an RF voltage waveform used to drive the source resonator. The magnetic field generated by the source resonator couples to the device resonator or receiver. This energy from the nearby receiver is then used to charge the battery, usually via an impedance transformation network or DC/DC converter to control the charging current. Stationary charging has better coupling, tuning, lateral alignment and higher efficiency than moving charging methods.

1.3 Dynamic Wireless Power Transfer

As mentioned, there is a growing interest in EVs due to low environmental impact and high energy efficiency. Battery and charger systems play a critical role in the development of EVs. Costly and heavy on-board battery storage and long charging time are the bottlenecks of widely adoption of electric vehicles. The benefits of wireless power transfer charging include mobility, safety, high reliability and low maintenance. This type of system transfers power from a stationary primary source embedded under the road to moving secondary

load. With good alignment, high efficiency and high power wireless power transfer can be achieved.

Compared to static wireless power transfer, constraints on storage and charging problem can be relaxed with dynamic wireless power transfer. If the facility is widely available, the requirements of high capacity, heavy and costly batteries in EVs can be reduced. Dynamic charging is accomplished by installing transmitter coils under the roadbed and the EVs with receiver pickup can be charged while moving along the road. One example system is implemented by [34, 43]. The online electric vehicle (OLEV) tram shown in Fig. 1.4 runs in a 2.2 km loop in Seoul Grand Park of which 370 meter is installed with transmitter coil. Using the charging system, the tram runs with a 40% smaller capacity battery and 6% lighter in weight. The long charging time in plugged-in or static wireless power transfer can also be reduced using dynamic charging.

According to the proposal from Ministry of Land, Infrastructure, Transport and Tourism of Japan, the transmitter coils should be buried 60-80 cm below the ground as the road surface is subject to frequent digging and refurbish for maintenance [44]. In [45], the vertical gap achieved is 50 cm at 78% coil to coil efficiency. Coils with ferrite cores [34] or bars [46] to improve coupling are costly and fragile [47]. Multiphase tracks are used to maintain the power level with misalignment however mutual inductance between tracks disrupts the operation of the power supply and causing additional loss in the inverter [48, 49]. Various multi-coil configurations such as double-D (DD), double-D quadrature (DDQ) and bipolar BP [50] has been explored to increase the misalignment tolerance. Though there is improvement, the misalignment is still limited to 30 cm. Buried coils under the road can act as sensors to guide the vehicles to stay within the lane and maintain in optimum charging position. The voltage or current generated at the receiver can be continually measured by the receiving sides on board the vehicle and position deviation can be detected. This information can then be used for autonomous or semi-autonomous vehicle controls. Researches such as [51, 52] aim at automated guidance for the driver to stay within the lane. Apart from the misalignment issue, dynamic charging system also needs a long charging area [53] so that the moving vehicles can receive sufficient power. Different coil configurations such as spaced loops [22, 54], sectional loops [55], or long wire loops [56, 57] have been explored
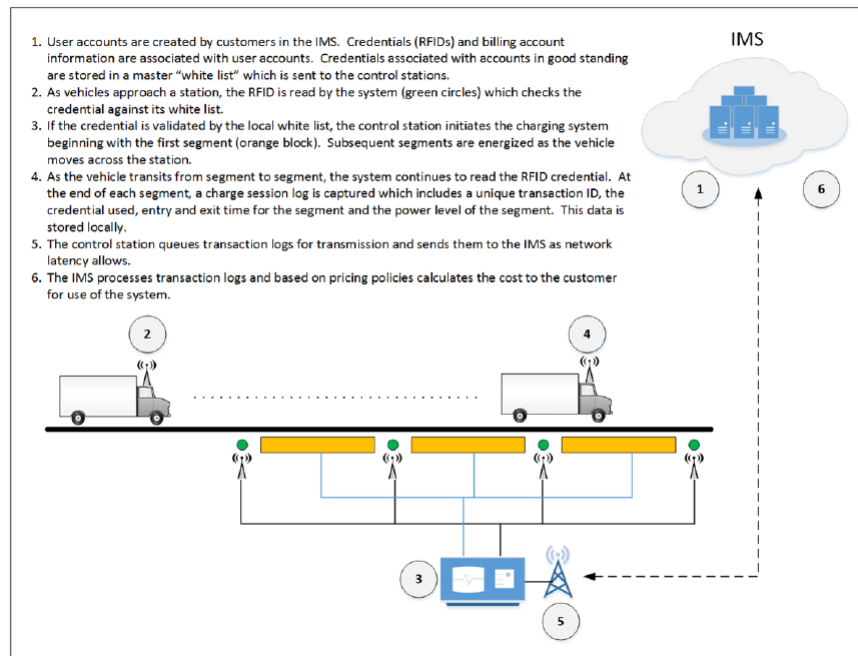
Figure 1.5: Infrastructure management system for activation of transmitters [59]. Magnetic sensors are used in placed of the RFID TAG for experimental purpose.

for dynamic charging. Long track distance leads to low coupling due to large leakage flux [55] and possibility of energizing and heating unwanted loads [58].

In this work, generalized theory of wireless power transfer system is first proposed. Then, configuration which is suitable for practical on-road implementation is proposed. Multiple small coils are used to achieve high transfer efficiency, and are activated only when the vehicle is approaching. Additionally, stable power level is obtained via even magnetic field design. Magnetic sensors are used to control the turn-on and turn-off of the transmitters for experimental purpose. In real highway, vehicle identification is also needed for charging and authentication. Therefore a RFID TAG system which can store information can be used to turn on the transmitters ahead. Fig. 1.5 shows an example of infrastructure management system (IMS) using RFID TAG to activate the transmitters and for billing purpose [59]. Here, magnetic sensors are used to demonstrate the activation and deactivation of the transmitters for dynamic charging.

1.4 Motivation

As aforementioned, wireless power transfer has become a practical technology in home and industrial environment due to growing usage of portable devices, electric vehicles and automation in factories. Wireless power transfer plays a critical role in the development of EVs. Convenient charging facilities allow frequent charge and dynamic charging reduces the long waiting time to refill. Both static and dynamic charging could potentially eliminate the bottleneck in the development of EVs which is costly and high capacity battery.

Using resonance, WPT system can transfer power effectively across gap with size of one to two times the dimension of the coils. The size of the receiver is usually restricted due to space constraint of the devices and EVs. Although the static transmitters can be larger, the transferable distance will still be limited by the receiver size. Therefore repeaters are used to extend both the vertical and horizontal effective areas. With larger effective area, the system should be able to support multiple receivers. Chapter 2 and Chapter 3 deal with the mathematical model for wireless power transfer with arbitrary number of repeaters and receivers. Impedance matching and power division methods are also proposed. Compared to past works, inverter representation is able to model a complex wireless power transfer system into multiple power flow paths, therefore various phenomena such as dead zone, power division and efficiency can be understood and generalized.

Compared to static charging, dynamic charging has more technical issues such as lower coupling coefficient, misalignment, efficiency, on-line activation of transmitters and power flow control. The research in Korea Advanced Institute of Science and Technology (KAIST) focuses on large vehicles [34] and public transportation where the traffic flow is constant. Oak Ridge National Laboratory (ORNL) uses ultra-capacitor to achieve power flow smoothing [60] whereas the University of Auckland [61] proposed pulse charging. In this work, even magnetic field is achieved via the coupled coil design and the power transferred can used to power motors directly. Multiple small transmitters are used to ensure high transfer efficiency.

Lastly the effect of impedance inverter characteristic to transferable power range and efficiency is studied using one-to-one and series-series compensated wireless power transfer. In practical, different power levels are needed when the vehicle is in different speeds or

accelerating. Therefore a flatter efficiency curve across different power range is proposed by exploiting the inverting characteristic of wireless power transfer. Future work includes applying the flat efficiency design for even-magnetic field configuration. Basic transient study is also performed using the widely known general state-space averaging (GSSA) for AC signals.

1.5 Dissertation Outline

The outline of this dissertation is illustrated in Fig. 1.6. The research is divided into theory portion and practical implementation portion. The details of this dissertation are summarized as follows:

1) Research background

- In Chapter 1, the history of wireless power transfer and application for electric vehicles are reviewed. Then the motivation and structure of this dissertation are also explained.

2) Theory of wireless power transfer

- In Chapter 2, impedance inverter representation of coupling is proposed. Then the generalized theory for arbitrary number of receivers and repeaters are explained.

- In Chapter 3, a special phenomenon when using repeaters in wireless power transfer for dynamic charging is explained. Using derived method from Chapter 2, the dead zone case is generalized into two different cases which are the even repeater and odd repeater.

3) Practical dynamic configuration

- In Chapter 4, a practical wireless power transfer method is proposed using multiple transmitters to one receiver to achieve even magnetic field. Neumann formula, maximum efficiency and AC resistance calculation method are also explained in this chapter.

- In Chapter 5, the effect of impedance inverting characteristic to power level and efficiency is studied. Design method is proposed to achieve flat efficiency across different power level. GSSA modeling method to study wireless power transfer small signal transient is also presented in this chapter.

- In Chapter 6, the hardware built for even magnetic field experiment is described.

4) Conclusion

- Chapter 7 lists the conclusion and future works of this dissertation.
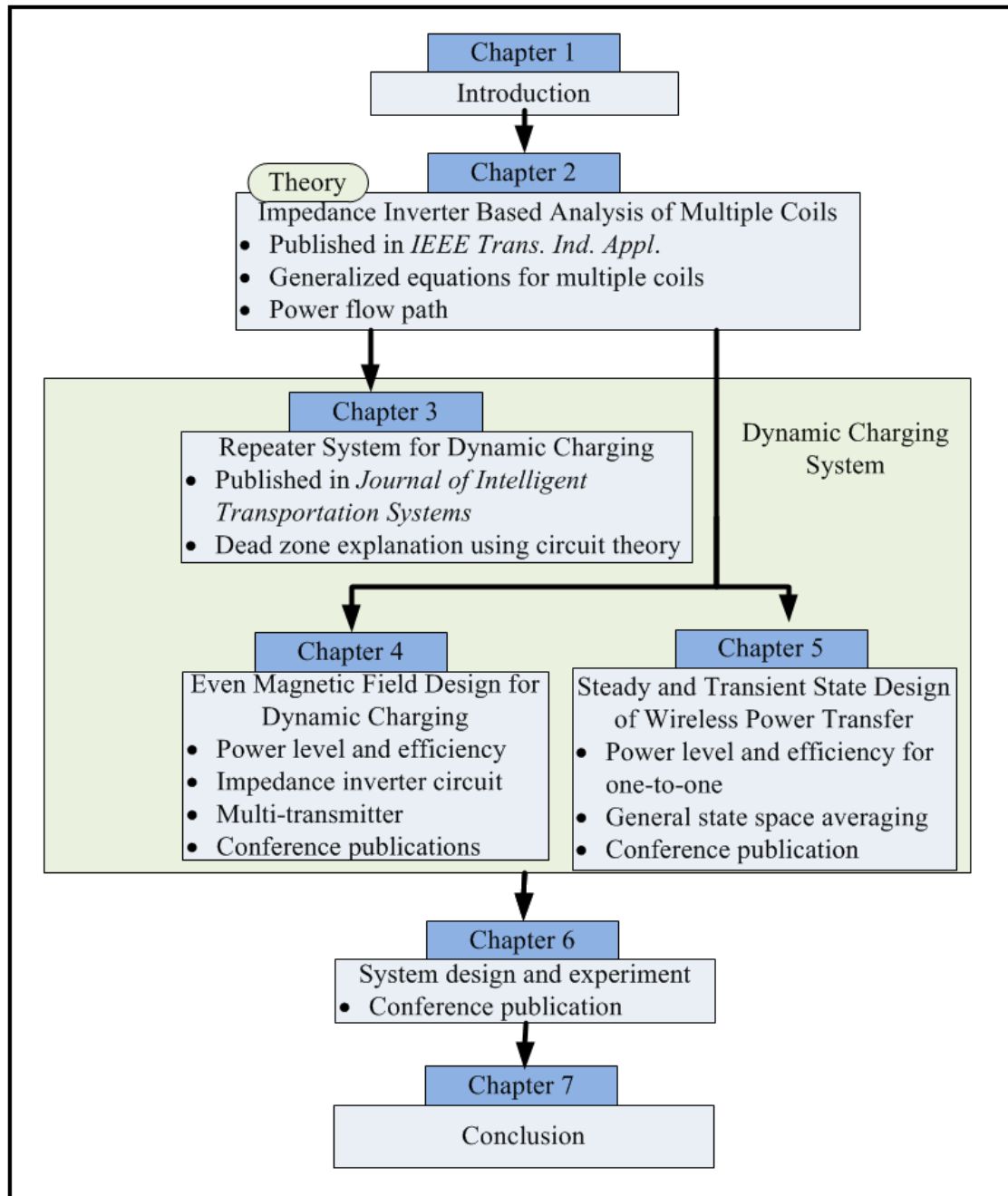
Figure 1.6: Dissertation structure.

Chapter 2

Impedance Inverter Based Analysis of Multiple Coils

Nomenclature

ω_0 Resonant angular frequency.

C_0 Capacitance of transmitter.

L_0 Inductance of transmitter.

R_0 Power supply output resistance.

k_{e0} External coupling coefficient of transmitter.

C_{ij} Capacitance of ith coil in jth transmission path.

L_{ij} Inductance of ith coil in jth transmission path.

k_{ij} Coupling coefficient of ith coil with $(i-1)$th coil in jth transmission path.

L_{mij} Mutual Inductance of ith coil with $(i-1)$th coil in jth transmission path.

K_{ij} Coupling of ith coil with $(i-1)$th coil
in jth transmission path represented with
characteristic impedance.

$R_{\mathrm{L}j}$ Load resistance of jth receiver.

$k_{\mathrm{e}j}$ External coupling coefficient of jth receiver.

$K_{\mathrm{e}j}$ Inverter characteristic impedance in jth receiver.

$C_{\mathrm{e}j}$ Capacitance in jth receiver's inverter circuit.

L_{ej} Inductance jth receiver's inverter circuit.

η_0 Loss in ith transmitter coil.

η_{ij} Loss in ith coil in jth transmission path.

η_{ej} Loss in inductor of jth receiver's inverter circuit.

2.1 Introduction

An ideal wireless power transfer must be able to transfer power efficiently regardless of the receiving end in the effective region. However magnetic resonant coupling method is efficient only in a fixed distance and orientation. When the receiver is moved away from its optimal operating point, the efficiency falls off rapidly [63]. Furthermore, in a wireless power transfer consisting of multiple receivers, receivers nearer to the transmitter tend to absorb more power [64]. Many past papers have proposed different ways to resolve the efficiency issue but not on power distribution.

Papers [27, 28, 65] explore the possibilities of multi-receiver system using either equivalent circuit or coupled mode theory. Efficiency analysis for different conditions is provided but methods for improving efficiency and power distribution are not proposed. Often wireless power transfer is analyzed using equivalent circuit [30],[65]-[70], however the equations for system with more coils quickly becomes complex or rigorous to be analyzed [30, 65]. Therefore, band-pass filter representation is proposed by [31, 32]. The design equations are simple even with many repeaters added in the power transfer system. The method is impractical due to inapplicable to multi-receiver and position of each coil need to be controllable.

Other attempts include adding and adjusting a medium coil to improve the transfer efficiency [71], [72]. The method however is limited to specific case. Frequency tracking method where the frequency of the source is varied for different conditions has also been proposed [63, 73, 74]. In practical applications, the wireless power transfer should stay inside an allowable industrial, scientific and medical band which is narrow. Therefore, tuning frequency is not a feasible method for wireless power transfer. In [67, 75], impedance matching circuit is inserted in the transmitter side based on equivalent circuit model. Transfer efficiency is optimized regardless of the receiving end. However controllable power distribution is not possible using this method.

In a multi-receiver system, not only the transfer efficiency is important but also the power distribution among the receivers. Power distribution depends on both the load impedance and relative positions of receivers to the transmitter. Assuming identical load connected to each receiver, the receiver nearest to the transmitter tends to absorb most of the power while the furthest receiver may not obtain enough to function properly. In this paper, method for impedance matching and controllable power division for a 13.56 MHz system [76, 77] is proposed. The design equations are derived and then generalized for arbitrary number of receivers and arbitrary number of repeaters. Simulations using LTspice and experiments are performed to validate the new method.

2.2 Multi-receiver and Repeater Wireless Power Transfer

2.2.1 Impedance Inverter

Impedance inverter is a type of circuit which has input impedance inversely proportional to the impedance connected at the other end. There are many applications and many types of impedance inverter [78]. In this paper, impedance inverter is used to represent the coupling between coils and impedance transformation.

Consider the equivalent circuit of one-transmitter and one-receiver wireless power transfer shown in Fig. 2.1. When coupling strength, k_{11} is expressed in mutual inductance terms [79], the equivalent circuit can be redrawn into Fig. 2.2 where:

$$k_{11} = \frac{L_{m11}}{\sqrt{L_0 L_{11}}} \qquad (2.1)$$

The components in the dashed rectangular forms an impedance inverter circuit and impedance Z_1, viewed from the transmitter towards the load, is:

$$
\begin{aligned}
Z_1 &= -j\omega_0 L_{m11} + [j\omega_0 L_{m11} // (-j\omega_0 L_{m11} + R_{L1})] \\
&= \frac{(\omega_0 L_{m11})^2}{R_{L1}} \\
&= \frac{K_{11}{}^2}{R_{L1}} \qquad (2.2)
\end{aligned}
$$

Provided that the internal resistance of each coil is small enough and can be ignored, and the system is in resonance. Therefore:

$$
\begin{aligned}
j\omega_0 L_0 + \frac{1}{j\omega_0 C_0} &\approx 0 \\
j\omega_0 L_{11} + \frac{1}{j\omega_{11} C_{11}} &\approx 0 \qquad (2.3)
\end{aligned}
$$

Magnetic resonant coupling coils have low internal resistance [2]. For simplicity, small impedance of the resonators is omitted in the design equations and dissipation loss calculation is performed afterwards.

Term K_{11} is the characteristic impedance of inverter [80] in Fig. 2.2. Relating coupling coefficient, k_{11} in (2.1) and K_{11} in (2.2), inverter characteristic impedance can be used to represent the coupling strength in between two coils.

$$
\begin{aligned}
K_{11} &= \omega_0 L_{m11} \\
&= \omega_0 k_{11} \sqrt{L_0 L_{11}} \qquad (2.4)
\end{aligned}
$$

The advantage of using inverter characteristic impedance representation is equation of form (2.2) simplifies impedance calculation in magnetic resonant circuit.
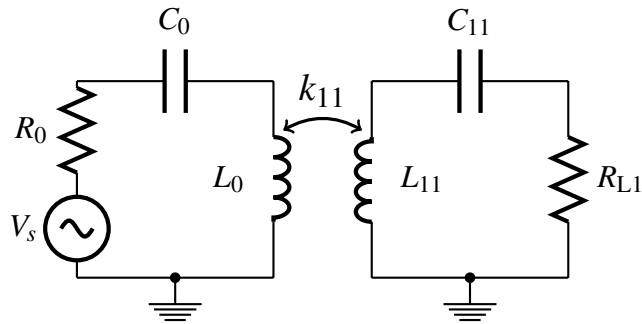
Figure 2.1: One-transmitter and one-receiver wireless power transfer.
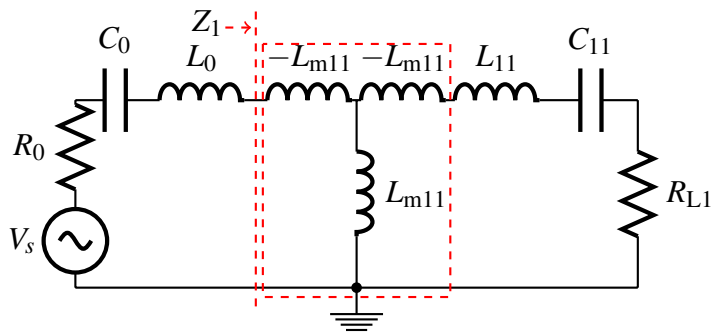
Figure 2.2: Impedance inverter as coupling strength representation.
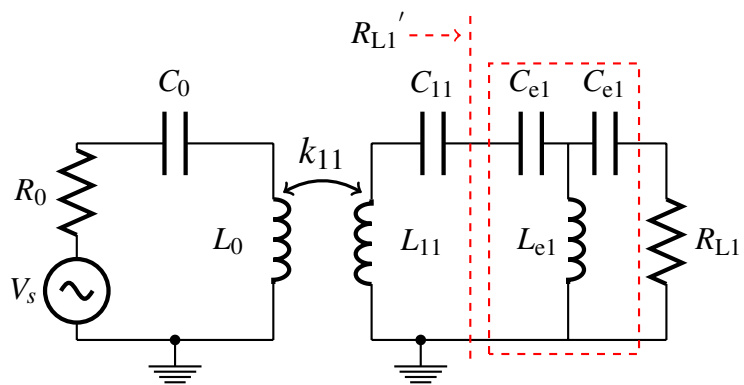
Figure 2.3: Impedance inverter for impedance transformation.

Besides coupling representation, inverter circuit is also used for impedance transformation. Fig. 2.3 is the same one-transmitter and one-receiver system in Fig. 2.1 except that an inverter circuit is implemented in between the receiver and load.

External coupling coefficient is defined as the ratio of each resonator termination resistance to the resonator "reactance slope parameter" [31, 80]. External coupling coefficients of transmitter, k_{e0}, and the receiver, k_{e1} for the one-transmitter and one-receiver system before implementing load impedance transformation are:

$$k_{e0} = \frac{R_0}{\omega_0 L_0} \qquad k_{e1} = \frac{R_{L1}}{\omega_0 L_{11}} \tag{2.5}$$

After impedance transformation using the inverter circuit in dashed rectangular of Fig. 2.3, the new k_{e1} is:

$$
\begin{aligned}
k_{e1} &= \frac{R_{L1}{}'}{\omega_0 L_{11}} \\
&= \frac{\left(K_{e1}{}^2/R_{L1}\right)}{\omega_0 L_{11}}
\end{aligned} \tag{2.6}
$$

The derivation and calculation of required receiver external coupling coefficients are given in subsequent sections.

Lumped inductors and capacitors are used in the impedance inverter circuit shown in the dashed rectangular in Fig. 2.3. The configuration is chosen so that the number of inductors can be minimized and the inverter circuit will be smaller. From (2.6), the required characteristic impedance of the inverter, K_{e1} is determined and is realized using an inductor and two capacitors with values [80]:

$$K_{e1} = \omega_0 L_{e1} = \frac{1}{\omega_0 C_{e1}} \tag{2.7}$$

2.2.2 System with Multi-receiver

Fig. 2.4 shows an equivalent circuit of a two-receiver wireless power transfer. Both receivers are coupled to the transmitter but cross coupling is not considered in this method.
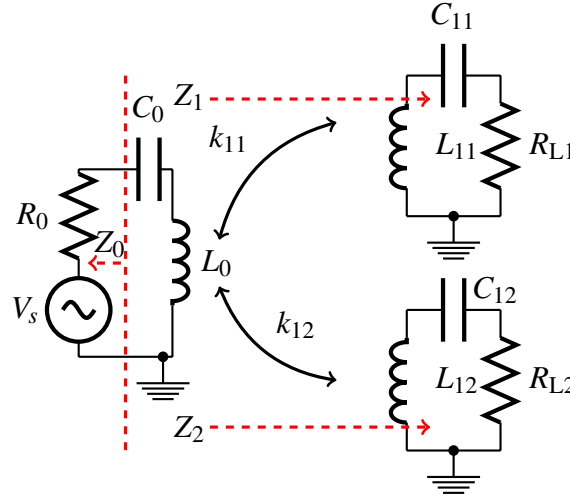
Figure 2.4: Equivalent circuit of a two-receiver system.

In actual applications, receivers are integrated into electric vehicles or other devices. The receivers therefore will not be overlapping and will be separated at least by 10% of the largest dimension. In this case, cross coupling will be significantly weaker compared to the coupling with transmitter [81].

The external coupling coefficients of this two-receiver system before impedance transformation are:

$$k_{e0} = \frac{R_0}{\omega_0 L_0} \qquad k_{e1} = \frac{R_{L1}}{\omega_0 L_{11}} \qquad k_{e2} = \frac{R_{L2}}{\omega_0 L_{12}} \tag{2.8}$$

Assuming all the coils are similar and the power source is operating at their resonant frequency, the impedance of coils is therefore ignored in the design equations for simplification. Deducing from (2.2), (2.4):

$$
\begin{aligned}
Z_1 &= \frac{K_{11}{}^2}{R_{L1}} \\
Z_2 &= \frac{K_{12}{}^2}{R_{L2}} \\
K_{11} &= \omega_0 k_{11} \sqrt{L_0 L_{11}} \\
K_{12} &= \omega_0 k_{12} \sqrt{L_0 L_{12}}
\end{aligned}
\tag{2.9}
$$

Where Z_1 is the impedance looking from transmitter to the first receiver in Fig. 2.4 and Z_2 is the impedance looking from transmitter to the second receiver. Substituting (2.8) into (2.9), the power supply output impedance, Z_0, Z_1 and Z_2 in terms of coupling coefficients and external coupling coefficients are:

$$
\begin{aligned}
Z_0 &= R_0 = k_{e0}\omega_0 L_0 \\
Z_1 &= \frac{k_{11}{}^2}{k_{e1}}\omega_0 L_0 \\
Z_2 &= \frac{k_{12}{}^2}{k_{e2}}\omega_0 L_0
\end{aligned}
\tag{2.10}
$$

Circuit in Fig. 2.4 is redrawn into Fig. 2.5 with mutual inductance terms to derive impedance matching and power division equations. Deducing from (2.1):

$$
k_{11} = \frac{L_{m11}}{\sqrt{L_0 L_{11}}} \qquad k_{12} = \frac{L_{m12}}{\sqrt{L_0 L_{12}}}
\tag{2.11}
$$

The current loop equations for Fig. 2.5 are given as:

$$
\begin{aligned}
V_s &= I_1 R_0 - I_2 j\omega_0 L_{m11} - I_3 j\omega_0 L_{m12} \\
0 &= I_2 R_{L1} - I_1 j\omega_0 L_{m11} \\
0 &= I_3 R_{L2} - I_1 j\omega_0 L_{m12}
\end{aligned}
\tag{2.12}
$$

Solving current I_2 and I_3 in terms of I_1:

$$
\begin{aligned}
I_2 &= \frac{j\omega_0 L_{m11}}{R_{L1}} \times I_1 \\
I_3 &= \frac{j\omega_0 L_{m12}}{R_{L2}} \times I_1
\end{aligned}
\tag{2.13}
$$
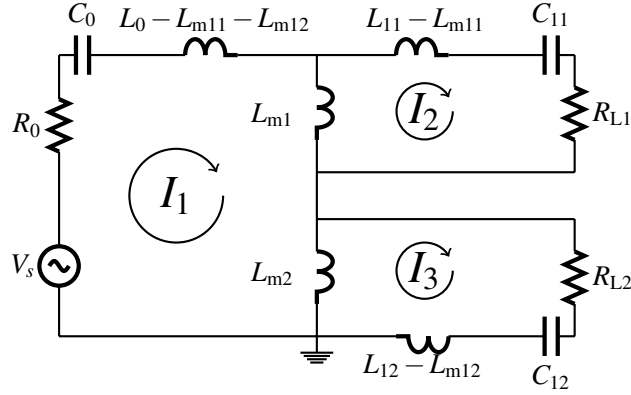
Figure 2.5: Circuit of two-receiver wireless power transfer in terms of mutual inductance.

Substituting (2.13) in the transmitter loop equation of (2.12), replacing load impedance with external coupling coefficient from (2.8) and mutual inductance with coupling coefficient from (2.11) :

$$
\begin{aligned}
\frac{V_s}{I_1} &= k_{e0}\omega_0 L_0 + \frac{k_{11}^2}{k_{e1}}\omega_0 L_0 + \frac{k_{12}^2}{k_{e2}}\omega_0 L_0 \\
&= Z_0 + Z_1 + Z_2
\end{aligned}
\tag{2.14}
$$

Equation (2.14) implies that circuit in Fig. 2.4 and Fig. 2.5 can be simplified into circuit shown in Fig. 2.6. The first term in (2.14) is the power supply output impedance, the second term is impedance Z_1 and the third term is impedance Z_2 in Fig. 2.4. Using maximum power transfer theorem [79], impedance matching is achieved when:

$$
\begin{aligned}
Z_0 &= Z_1 + Z_2 \\
k_{e0} &= \frac{k_{11}^2}{k_{e1}} + \frac{k_{12}^2}{k_{e2}}
\end{aligned}
\tag{2.15}
$$

Same current I_1 is flowing through impedance Z_1 and impedance Z_2 and both receivers are
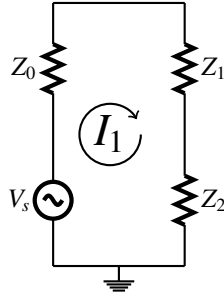
Figure 2.6: Simplified two-receiver circuit.

not coupled, therefore the power division ratio is:

$$P_1 \quad : \quad P_2$$

$$Z_1 \quad : \quad Z_2$$

$$\frac{k_{11}{}^2}{k_{e1}} \quad : \quad \frac{k_{12}{}^2}{k_{e2}} \tag{2.16}$$

where P_1 and P_2 are power across R_{L1} and power across R_{L2} respectively.

Power division ratio can also be derived using current flowing through each load. For system in Fig. 2.4 or Fig. 2.5, P_1 and P_2 are respectively:

$$P_1 \quad = \quad |I_2|^2 R_{L1}$$

$$P_2 \quad = \quad |I_3|^2 R_{L2} \tag{2.17}$$

Again using (2.8), (2.11) and (2.13):

$$P_1 \quad = \quad \frac{k_{11}{}^2}{k_{e1}} \times \omega_0 L_0 \times |I_1|^2$$

$$P_2 \quad = \quad \frac{k_{12}{}^2}{k_{e2}} \times \omega_0 L_0 \times |I_1|^2 \tag{2.18}$$

The power division ratio, $P_1 : P_2$ is therefore once again agreeing with (2.16).

For controllable power division and impedance matching without having to change the position of each coil, impedance inverter circuit as shown in Fig. 2.3 is used for impedance transformation. The new external coupling coefficients of receivers after impedance transformation are:

$$k_{e1} = \frac{R_{L1}'}{\omega_0 L_{11}}$$

$$= \frac{(K_{e1}^2/R_{L1})}{\omega_0 L_{11}} \tag{2.19}$$

$$k_{e2} = \frac{R_{L2}'}{\omega_0 L_{12}} \tag{2.20}$$

$$= \frac{(K_{e2}^2/R_{L2})}{\omega_0 L_{12}} \tag{2.21}$$

External coupling coefficient of transmitter, k_{e0} is fixed since impedance transformation is not implemented in the transmitter. Given the position of each coil, the required external coupling coefficient of every receiver is calculated by solving (2.15) and (2.16) where $P_1 : P_2$ is the desired power division ratio.

2.2.3 System with Repeaters

Although wireless power transfer via magnetic resonant coupling is able to transmit power more efficiently compared to induction method, the transmittable distance is still limited to a few meters. This range is extendable using repeater coils. However when more coils are added into the system, existing equivalent circuit equations become complicated. Paper [67] resorts to search algorithms and [30] uses computer aided design (CAD). Band-pass filter design method [31, 32] is simple but is impractical due to stringent conditions exerted by band-pass filter equations. New impedance matching method for wireless power transfer with repeaters is proposed. The new method combines the advantages of both existing equivalent circuit and band-pass filter method.

Consider the equivalent circuit of a wireless power transfer with a repeater coil in between transmitter and receiver shown in Fig. 2.7. Assuming impedance matching is to be carried out by transforming impedance Z_4:

$$Z_4 = Z_3 \tag{2.22}$$

The external couplings of this system before impedance transformation are:

$$
\begin{aligned}
k_{e0} &= \frac{R_0}{\omega_0 L_0} \\
k_{e1} &= \frac{R_{L1}}{\omega_0 L_{21}}
\end{aligned}
\tag{2.23}
$$

In order to satisfy (2.22), the required new k_{e1} is calculated. Assuming the system is in resonance and the impedance of each of the coils is ignored. Using equation of form (2.2) to calculate impedance in Fig. (2.7):

$$
\begin{aligned}
Z_1 &= R_0 \\
Z_2 &= \frac{K_{11}{}^2}{Z_1} \\
Z_3 &= \frac{K_{21}{}^2}{Z_2}
\end{aligned}
\tag{2.24}
$$

Deducing from (2.4):

$$
\begin{aligned}
K_{11} &= \omega_0 k_{11} \sqrt{L_0 L_{11}} \\
K_{21} &= \omega_0 k_{21} \sqrt{L_{11} L_{21}}
\end{aligned}
\tag{2.25}
$$

Substituting (2.22), (2.23) and (2.25) into (2.24), the required external coupling of the receiver is:

$$k_{e1} = k_{e0} \times \frac{k_{21}{}^2}{k_{11}{}^2} \tag{2.26}$$

An inverter circuit can then be inserted into the receiver side, similarly to Fig. 2.3, to realize the required external coupling coefficients.
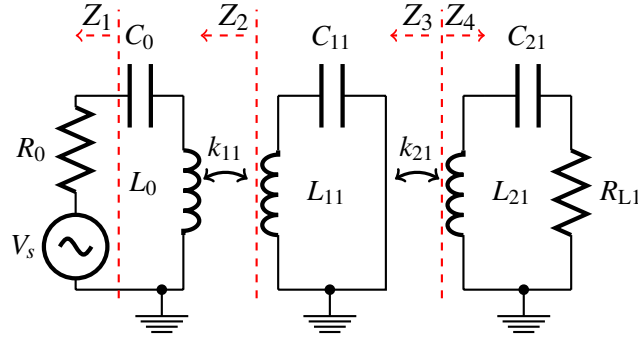
Figure 2.7: Equivalent circuit for wireless power transfer with repeater.

2.2.4 Generalized Equations for System with Both Multi-receiver and Repeaters

The equations derived in previous subsections are generalized for wireless power transfer with arbitrary number of repeaters and arbitrary number of receivers. Consider a wireless power transfer with m number of receivers and $n(j) - 1$ number of repeaters in between jth receiver and transmitter in Fig. 2.8.

Firstly, external coupling coefficient of the transmitter, k_{e0} is broken down into m-number of parts:

$$k_{e0} = \frac{R_0}{\omega_0 L_0} = \sum_{j=1}^{j=m} k_{e0,j} \tag{2.27}$$

Where $k_{e0,j}$ is the external coupling coefficient of the transmitter (k_{e0}) distributed to jth receiver. According to (2.16), the percentage of power received by jth receiver will be:

$$\%P_j \mid_{j=1 \ to \ m} = \frac{k_{e0,j}}{k_{e0}} \times 100\% \tag{2.28}$$

Finally, external coupling coefficient of each receiver has to be:

$$k_{ej} \mid_{j=1 \ to \ m} = k_{e0,j}^{(-1)^{n(j)}} \times \prod_{i=1}^{i=n(j)} k_{ij}^{2(-1)^{i+n(j)}} \tag{2.29}$$
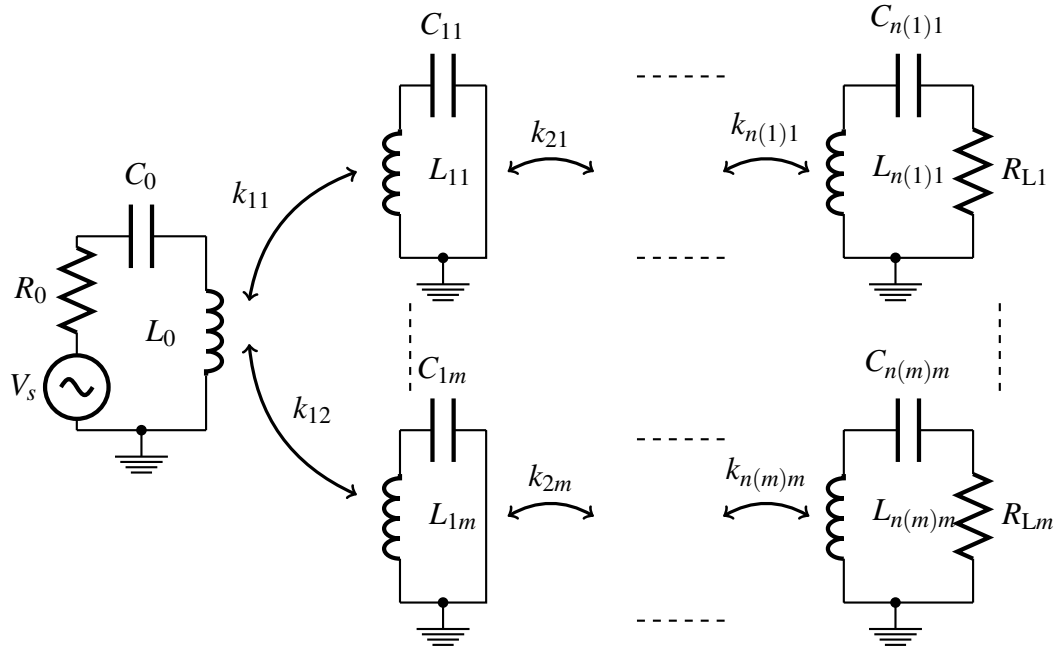
Figure 2.8: Wireless power transfer with arbitrary number of receivers and repeaters.

Where $k_{ej}\,|_{j=1\ to\ m}$ is realized using impedance inverters with characteristic impedance:

$$K_{ej}\,|_{j=1\ to\ m} = \sqrt{k_{ej}\omega_0 L_{n(j)j}R_{Lj}} \tag{2.30}$$

2.3 Simulation Results

Calculation and simulation results of multi-receiver and repeater are given in this section to demonstrate the proposed power division method. The equivalent circuit of a two-receiver system and with one repeater inserted between the first receiver and the transmitter is simulated using LTspice. Fig. 2.9 shows the simulation circuit after implementing impedance transformation at both receivers. The element values of the system are listed below:
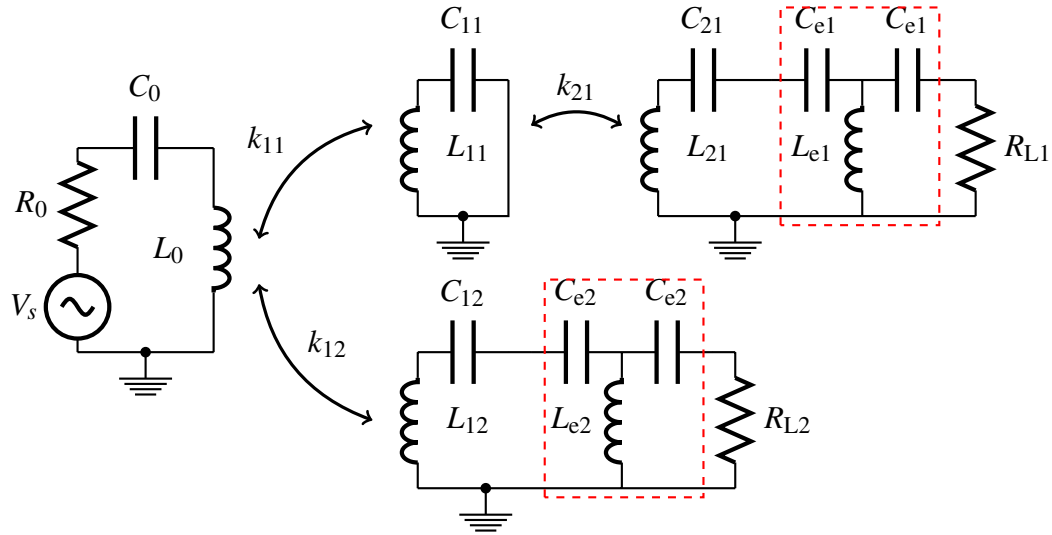
Figure 2.9: Simulation circuit.

$$\omega_0 = 2\pi \times 13.56\,\text{MHz}$$

$$L_0 = L_{11} = L_{21} = L_{12} = 9.4\,\mu\text{H}$$

$$C_0 = C_{11} = C_{21} = C_{12} = 14.7\,\text{pF}$$

$$R_0 = R_{\text{L1}} = R_{\text{L2}} = 50\,\Omega$$

$$k_{11} = k_{21} = 0.066$$

$$k_{12} = 0.084 \tag{2.31}$$

The internal resistance of each of the resonant coil is set to $1\,\Omega$ and the internal resistance of inductors in inverter circuits are set to $0.5\,\Omega$. The power ratio $P_1 : P_2$ for this first simulation is set to 1, where P_1 is the power received by load R_{L1} and P_2 is the power received by load R_{L2}. Using (2.27) to (2.30):

$$
\begin{aligned}
k_{e0} &= 0.062 \\
k_{e0,1} &= k_{e0,2} = 0.031 \\
k_{e1} &= 0.031 \\
k_{e2} &= 0.225 \\
K_{e1} &= 35\,\Omega \\
K_{e2} &= 95\,\Omega
\end{aligned}
\tag{2.32}
$$

Using (2.7), the element values in the dashed rectangles of Fig. 2.9 are:

$$
\begin{aligned}
C_{e1} &= 335\,\text{pF} \\
L_{e1} &= 0.41\,\mu\text{H} \\
C_{e2} &= 126\,\text{pF} \\
L_{e2} &= 1.1\,\mu\text{H}
\end{aligned}
\tag{2.33}
$$

Fig. 2.10(a) shows the simulation results before applying the method. Due to impedance mismatch, the reflection ratio, η_{11} is around 22% at the resonant frequency 13.56 MHz. The transmission ratio, η_{21} to the first receiver, which is separated with the transmitter by a repeater coil is around 27%. The transmission ratio, η_{31} to the second receiver is around 48%. The simulation results after inserting inverter circuits with characteristic impedance calculated above is shown in Fig. 2.10(b). Reflection ratio is reduced to almost none, and both receivers obtain almost equalized power as desired.

In the second simulation, power ratio $P_1 : P_2$ is set to be $\frac{7}{3}$. Using the same calculation steps as the previous simulation case, the characteristic impedance of the inverters and element values are:
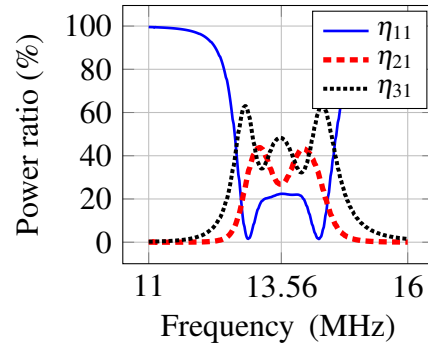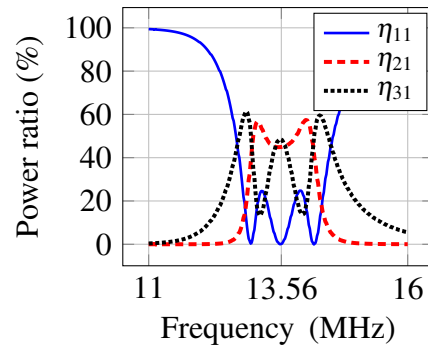
Figure 2.10: Simulation results of equal power division: a) before method b) after method.
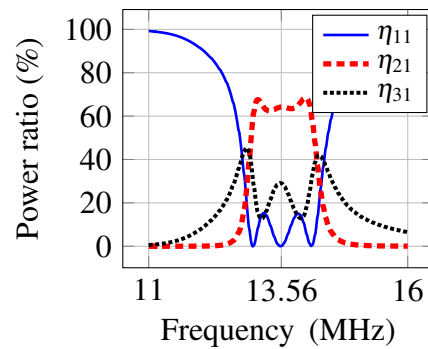
Figure 2.11: Simulation results of 70%-30% power division.

$$
\begin{aligned}
K_{e1} &= 42\,\Omega \\
K_{e2} &= 122\,\Omega \\
C_{e1} &= 281\,\text{pF} \\
L_{e1} &= 0.49\,\mu\text{H} \\
C_{e2} &= 96\,\text{pF} \\
L_{e2} &= 1.43\,\mu\text{H} \tag{2.34}
\end{aligned}
$$

Fig. 2.11 shows the simulation results after applying the method. Similar to equal power distribution case, reflection ratio, η_{11} is reduced to almost none. Transmission ratio, η_{21} to the first receiver is around 64% and transmission ratio, η_{31} to the second receiver is around 29% as desired.

2.4 Experiment Results

Experiments are performed for the simulation cases discussed in the previous section. The experiment setup is shown in Fig. 2.12. The equipment used is Agilent Technologies vector network analyzer E5061B (VNA). All the coils are open type helical, 150 mm in radius, 5 mm in pitch, five copper wire turns and with internal resistance around $1\,\Omega$. They are tuned to resonate at (13.56 ± 0.01) MHz. Transmitter, repeater and first receiver are arranged side by side horizontally. The second receiver is placed 16 cm vertically above the transmitter. Measurements of the coupling coefficients and coils are the same as the values given in the simulation results section. Port-1 of VNA which acts as source is connected to the transmitter. One receiver is connected to the port-2 of the VNA at a time to measure the power received. The other receiver is terminated by a RF $50\,\Omega$ as shown in Fig. 2.13. When measuring reflection coefficient, S_{11}, both receivers are terminated by RF $50\,\Omega$ resistor. Reflection coefficient, S_{11} and forward gain, S_{21} are then recorded from the VNA. The reflected power ratio η_{11}, power ratio for the first receiver η_{21}, and power ratio for the second receiver η_{31} are then calculated:
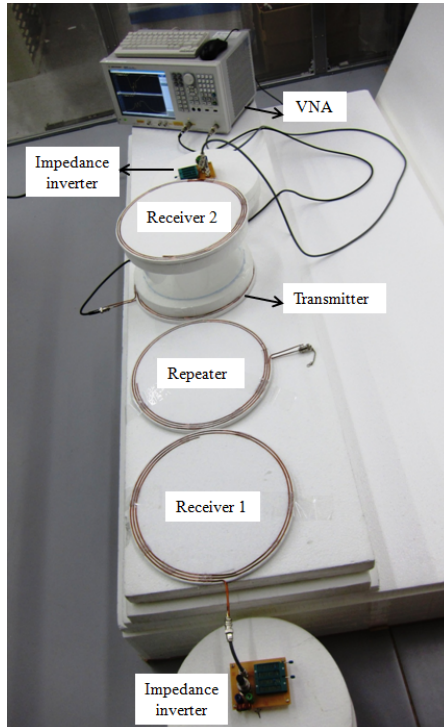
Figure 2.12: Experiment setup.

$$\eta_{11} = |S_{11}|^2 \times 100\%$$

$$\eta_{21} = |S_{21}|^2 \times 100\%$$

(first receiver connected to port-2)

$$\eta_{31} = |S_{21}|^2 \times 100\%$$

(second receiver connected to port-2)   (2.35)

Plots in Fig. 2.14(a) show the frequency response before applying method. At 13.56 MHz, reflected power η_{11} is 23%, η_{21} is 25% and η_{31} is 48%. Impedance transformation is applied at both receivers for impedance matching and equal power division. The capacitors in the inverter circuit shown in Fig. 2.13 are ceramics capacitors and the inductor is ferrite
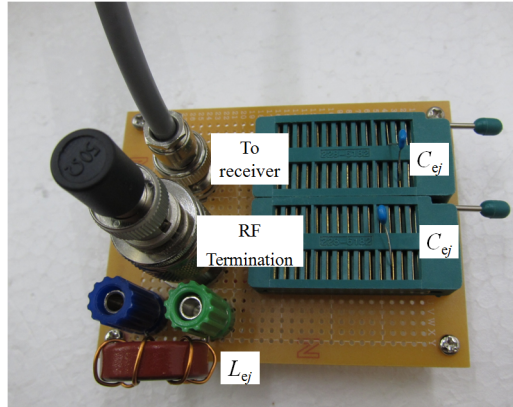
Figure 2.13: Inverter circuit.

core wounded with cooper wires. The internal resistance of each inductor is measured to be around 0.5 Ω. The capacitance and inductance chosen are close to the calculated values in (2.33). The plots in Fig. 2.14(b) show that the reflection ratio, η_{11} is reduced to around 4%, while η_{21} is 38% and η_{31} is 49% after implementing the proposed method.

In the second experiment, inverters with capacitance and inductance values listed in (2.34) are implemented in both receivers to obtain $P_1 : P_2$ ratio of 7:3. Reflection ratio, η_{11} is reduced to around 5%. Transmission ratio, η_{21} to the first receiver is around 55% and transmission ratio, η_{31} to the second receiver is around 31%.

Table 2.1 shows the summary simulation and experiment results of the system at the frequency of interest, 13.56 MHz. From simulation results, first receiver will suffer more loss as there is an additional repeater loss compared to second receiver. There are maybe other non-ideal parameters that cause lower η_{21} values compared to calculation for example the tolerance of capacitors and inductors in the impedance transformation circuits. In all experiment cases, the higher reflection coefficients compared to the simulation results may be due to a different connector interface used in VNA calibration from the connector interface used in actual measurement and the resonator coils do not have perfect 13.56 MHz resonant frequency.
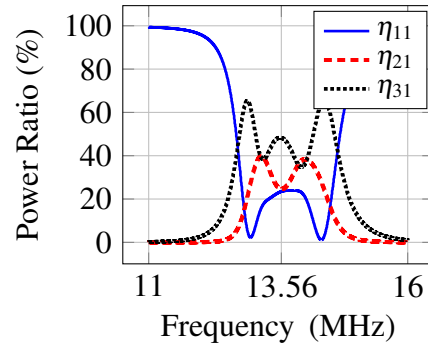
(a)
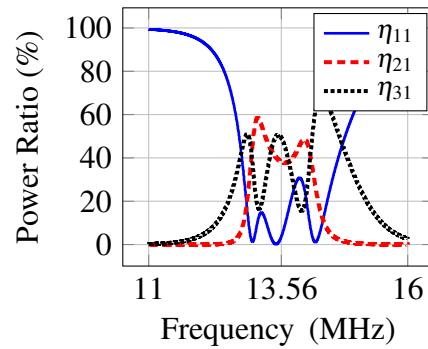
(b)

Figure 2.14: Experiment results of equal power division: a) before method, b) after method.
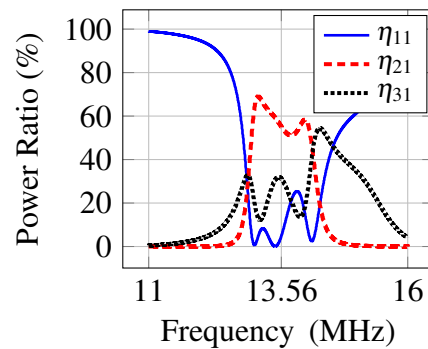
Figure 2.15: Experiment results of 70%-30% power division.

Table 2.1: Simulation and experiment results at 13.56 MHz.

	Simulation	Experiment
Before Method		
η_{11}	22%	23%
η_{21}	27%	25%
η_{31}	48%	48%
After 50%-50% division		
η_{11}	0%	4%
η_{21}	45%	38%
η_{31}	48%	49%
After 70%-30% division		
η_{11}	0%	5%
η_{21}	64%	55%
η_{31}	29%	31%

2.5 Discussion

2.5.1 Dissipation Loss in Coils

As can be seen in both the simulation and experiment results at 13.56 MHz, loss occurs in the system. Assuming the loss is caused by heat dissipation in internal resistance of coils in resonators and inverter circuits, and this internal resistance is in series with the coils. The loss can then be calculated using square of magnitude current flowing through the coils multiplied by internal resistance, $|I|^2 r$. Further assuming that the dissipation loss in capacitors is small and can be ignored, we can estimate where the bulk of loss is coming from by using the current measurement in simulations where the resonators coils are estimated to be having $1\,\Omega$ resistance and the inductors in inverter circuits are having $0.5\,\Omega$ resistance. Table 2.2 shows the percentage loss in all coils including the coils in inverter circuits for the 50%-50% case.

Table 2.2: Loss in coils for the 50%-50% division system.

	Percentage loss
η_0	1.9%
η_{11}	0.4%
η_{21}	1.9%
η_{12}	0.6%
η_{e1}	1.4%
η_{e2}	0.6%
Total	6.8%
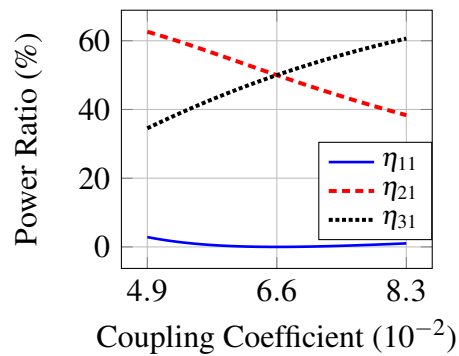
Figure 2.16: Method sensitivity toward coupling variations.

2.5.2 Sensitivity towards Coupling Variations

In actual applications, the position of transmitter and repeaters installed will be fixed. The coupling coefficient towards receiver however will vary each time the receiver is placed. A preliminary study of the sensitivity of proposed method towards small coupling variations is provided in this section. Using the 50%-50% case, plot in Fig. 2.16 shows the reflection coefficient, and percentage power received by both receivers when coupling coefficient, k_{21} is varying linearly from 0.049 to 0.083. Within the coupling coefficient range, reflection ratio is below 3%. However power received by each receiver varies from 30% to 60%.

2.5.3 Sensitivity towards Component Variations

Proposed method offers a simple and fast calculation method for impedance matching and power division for wireless power transfer consisting of multiple repeaters and receivers. In real implementation however, exact element values do not exist. A Monte Carlo simulation is performed to investigate the sensitivity of the proposed method towards component variations. Again the 50%-50% case is used as example. Assuming the components are normally distributed, with means given by the derived components formulas and with standard deviations σ such that at least a proportion of p=99% falls within the component tolerance. All the components at the second receiver are fixed. One of the capacitor in the inverter of the first receiver is simulated with tolerance 25% for three inductor values, the nominal value 0.41 μH and $\pm$25% from the nominal value.

Fig. 2.17(a) shows the distribution of reflected power ratio for 1000 samples of capacitors. For all three inductor values, the reflection is below 5%. As for the power distribution, an obvious pattern can be seen from 2.17(b) and 2.17(c). Increasing the inductance in the inverter circuit increases the impedance viewed towards first receiver. However this change has less impact on the reflection coefficient compared to power division between the two receivers. The distribution of the reflected power and power division for each inductor value only spreads slightly from the mean value with 0.33 μH showing the most dispersion.

Applying auto-tuning on the method depends on the requirement of each application. High frequency relays [67] can be used to switch between blocks of inverter circuits installed at the receiver sides. Based on Monte Carlo simulation results, the inductors used in actual applications can be built with tighter tolerance and capacitors within $\pm$25% tolerance are acceptable for the method. If high accuracy of power division ratio is required, a finer auto-tuning circuit can be built. Reflection coefficient on the other hand, is more robust towards coupling variations and component variations.

2.6 Chapter Summary

New impedance matching and power division method is proposed and generalized for arbitrary number of receivers and arbitrary number of repeaters. Due to uniform equations
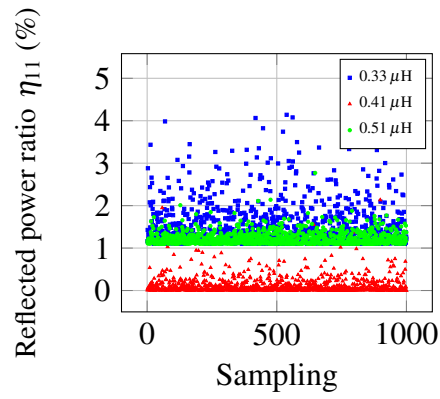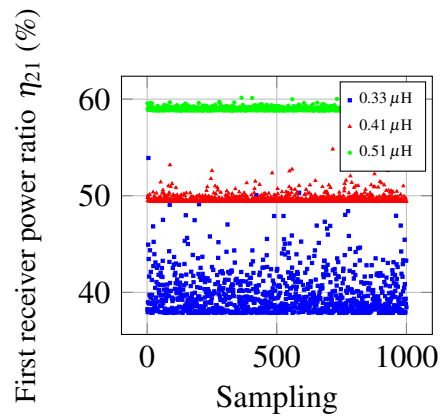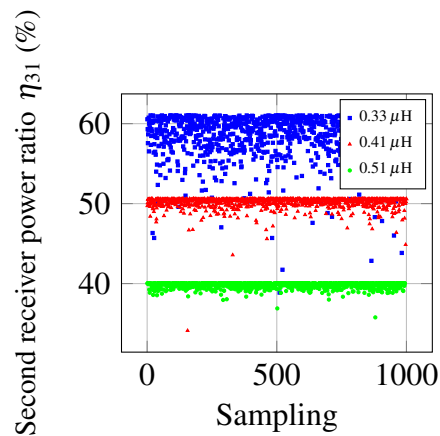
Figure 2.17: Power distribution for 25% component tolerance: a) reflected power ratio, b) power ratio of the first receiver, c) power ratio of the second receiver.

resulted when using impedance inverter representation, the design equations are simple. Impedance matching and power division conditions are expressed in terms of coupling coefficient which is the commonly used representation. In order to implement controllable power division without having to change the position of each coil, the external coupling coefficients of the receivers can be modified by inserting impedance inverter circuit in between receiver and the corresponding termination resistor.

Chapter 3

Repeater System for Dynamic Charging

Nomenclature

ω_0 Resonant angular frequency.

C_0 Capacitance of transmitter.

L_0 Inductance of transmitter.

R_0 Power supply output resistance.

k_{ij} Coupling coefficient between coil i and coil j.

K_{ij} Impedance inverter representations of k_{ij}.

L_i Inductance of coil i.

C_i Capacitance of coil i.

r_i Internal resistance of coil i.

$Z_{\mathrm{L}i}$ Load impedance of coil i if there are
multiple receivers.

Z_{L} Load impedance if there is only one receiver.

$Z_{\mathrm{c}i}$ Impedance sum of the inductor, capacitor and
internal resistance of coil i.

Z_i Impedance viewed from one point to one point
showed in the corresponding diagram

Z_{in} Input impedance viewed by the power supply
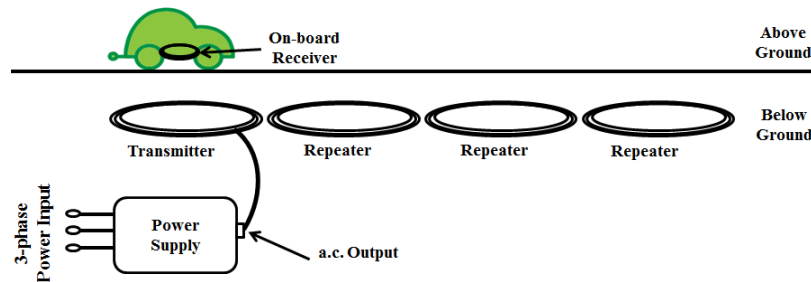
Figure 3.1: Conceptual wireless charging while moving system.

3.1 Introduction

Using wireless charging for electric vehicle is safe and convenient compared to plugging the vehicle into power outlet. This mid-range transfer method enables wireless charging while the vehicle is moving on the road and range extension can be achieved with repeater coils.

The wireless power transfer coils can be embedded beneath and arranged along the road. The car is then charged while moving on the road. However dead zones exist in certain positions where the power does not transfer to the load [82]. Conventional equivalent circuit equations is complex and difficult to understand due to number of coils involved [30, 65]. This paper analyzes the dead zone condition using impedance inverter representation of coupling and power division principle in wireless power transfer derived in Chapter 2. The analysis method can be easily extended for a section of road that consists of one transmitter and arbitrary number of repeaters. The conceptual wireless charging while moving system that will be studied in this paper is explained in the next section.

3.2 Conceptual Wireless Charging while Moving System

Fig. 3.1 shows the wireless charging system studied in this paper. Power supply receives power from the 3-phase transmission grid and performs frequency conversion to the resonant frequency of the wireless power transfer system. The power supply is connected to

the transmitter coil via cable and this coil will be referred as transmitter from here on. Receiver is the coil installed on-board of the electric vehicle to charge the battery. Repeater coils as shown in Fig. 3.1 can be used to expand the charging system coverage [83] while simplifying the underground connection network. Also, the transmitter and subsequent repeaters are placed side by side horizontally. Therefore, repeaters will not be overlapping each other as shown in Fig. 3.1. Assuming the transmitter and all the repeaters are the same, non-adjacent resonant coils will be separated at least one time the diameter. Coupling between non adjacent transmitter or repeater can be ignored in this case [81].

The analysis is limited to the cases where the receiver is coupled to either the transmitter only or one of the repeaters only. The case where the vehicle is between two resonator coils and receiving power simultaneously from both is not included in this investigation. A 13.56 MHz system [76], [77] is used as the case analysis in this paper. The findings are then generalized for arbitrary number of repeaters. Simulations using LTspice and experiments are performed to validate the mathematical analysis.

3.3 Derivation

This section provides the basis needed which are impedance inverter representation and power division equations to analyse the system. Five example analysis cases are then given in the subsequent sections.

An equivalent circuit of a two-receiver wireless power transfer system is shown in Fig. 3.2. The couplings between coils, k_{01} and k_{02} are expressible in terms of characteristic impedance of inverter, K_{01} and K_{02} respectively [80]:

$$k_{01} = \frac{K_{01}}{\omega\sqrt{L_0 L_1}} \qquad k_{02} = \frac{K_{02}}{\omega\sqrt{L_0 L_2}} \tag{3.1}$$

Impedance inverter, as the name implies, inverts the impedance connected to the inverter. Fig. 3.3 and (3.2) show the impedance Z_1 looking into a general impedance inverter with characteristic impedance, K that is connected to load, Z_L at the other end. Similar to the discussion in Chapter 2, impedance inverter is used to represent the couplings between coils given as in (3.1).
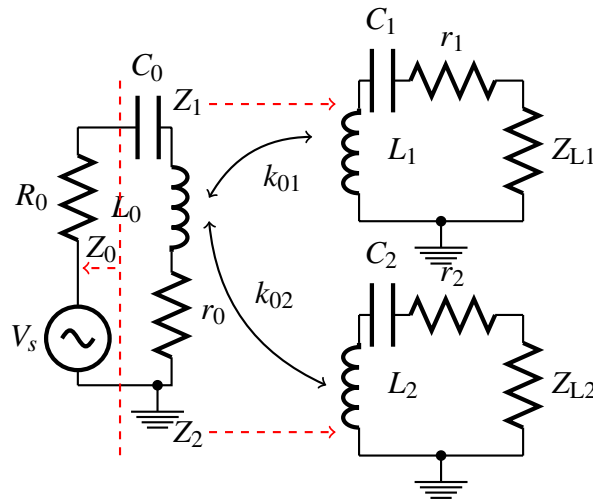
Figure 3.2: Equivalent circuit of a two-receiver system.
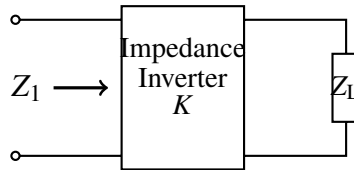
Figure 3.3: Operation of impedance inverter.
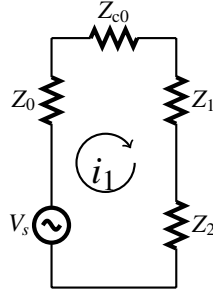
Figure 3.4: Simplified two-receiver circuit.

$$Z_1 = \frac{K^2}{Z_L} \tag{3.2}$$

From Fig. 3.2, (3.1) and (3.2):

$$Z_0 = R_0$$

$$Z_1 = \frac{K_{01}{}^2}{Z_{L1} + Z_{c1}}$$

$$Z_2 = \frac{K_{02}{}^2}{Z_{L2} + Z_{c2}}$$

$$Z_{c0} = r_0 + j(\omega L_0 - \frac{1}{\omega C_0})$$

$$Z_{c1} = r_1 + j(\omega L_1 - \frac{1}{\omega C_1})$$

$$Z_{c2} = r_2 + j(\omega L_2 - \frac{1}{\omega C_2}) \tag{3.3}$$

where Z_1 is the impedance looking from the transmitter to the top receiver in Fig. 3.2 and Z_2 is the impedance looking from the transmitter to the bottom receiver.

Impedance Z_{c0}, Z_1, and Z_2 appear in series connection when viewing from the source [84] and therefore circuit of Fig. 3.2 can be simplified into Fig. 3.4.
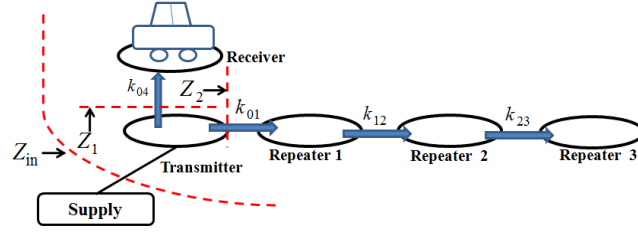
Figure 3.5: Case I analysis.

3.4 Case Analysis

A section of charging while moving wireless power transfer, which consists of a transmitter and three repeaters embedded beneath the road, is used as an example. Five different cases are considered in this section. The coil numbering convention applied in this section and subsequent sections is subscript 0 for the transmitter, 1, 2 and 3 for repeater 1, repeater 2 and repeater 3 respectively, and 4 for the receiver. For Case V, there is no repeater 3, but subscript 4 will still be used for the receiver.

Assuming the vehicle is at the beginning of the charging system and is coupled only to the transmitter as shown in Fig. 3.5, impedance Z_1 is the impedance looking from the transmitter towards the load through coupling k_{04}. Coupling k_{04} can be represented by an impedance inverter with characteristic impedance K_{04}. Therefore from (3.2),

$$Z_1 = \frac{K_{04}{}^2}{Z_L + Z_{c4}} \tag{3.4}$$

Again using impedance inverter representations for the impedance viewed from the transmitter towards the transmission path that contains all the repeaters:

$$Z_2 = \frac{K_{01}{}^2}{\frac{K_{12}{}^2}{\frac{K_{23}{}^2}{Z_{c3}} + Z_{c2}} + Z_{c1}} \tag{3.5}$$

Term Z_{c1}, Z_{c2} and Z_{c3} are the impedance sum of the inductor, capacitor and internal resistance of the first repeater, second repeater and third repeater respectively. In all cases
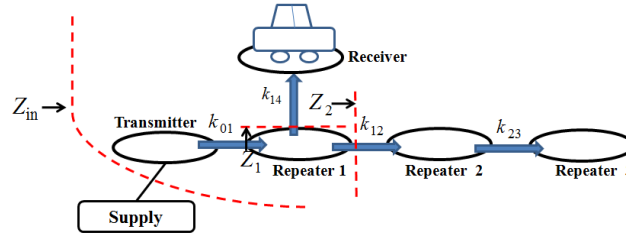
Figure 3.6: Case II analysis.

discussed in this paper, each of the coils is in resonance with the capacitor that is connected in series. Also internal resistance should be small for magnetic resonant coupling [2]. Both the real part and imaginary part of these impedance are small and impedance Z_2 will be large. If impedance Z_2 is assumed to be large enough compared to the power supply output impedance, this impedance can be assumed open-circuit. According to Sec. 3.3, impedance Z_1, Z_2 and Z_{c0} appear as series when seen from the power supply. The power supply input impedance is given by (3.6). The load appears as open-circuit to the supply and almost all the power is reflected back instead of traveling to the load.

$$Z_{in} = Z_1 + Z_2 + Z_{c0} \tag{3.6}$$

In case II analysis which is shown in Fig. 3.6, the vehicle is located above the first repeater and coupled to only that repeater, and the impedance becomes:

$$Z_1 = \frac{K_{14}^2}{Z_L + Z_{c4}}$$

$$Z_2 = \frac{K_{12}^2}{\frac{K_{23}^2}{Z_{c3}} + Z_{c2}}$$

$$Z_{in} = \frac{K_{01}^2}{Z_1 + Z_2 + Z_{c1}} + Z_{c0} \tag{3.7}$$

Impedance Z_2 is close to zero and is assumed short-circuit. This short-circuit impedance is in series with the load. The load impedance is seen by the power supply and power is able to be transferred to the load.
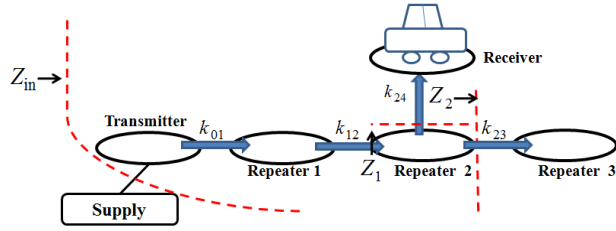
Figure 3.7: Case III analysis.
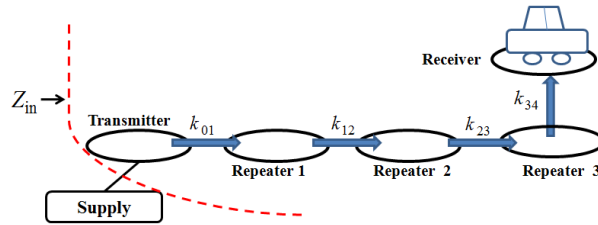
Figure 3.8: Case IV analysis.

Using the same argument as case I and case II, the impedance in case III shown in Fig. 3.7 which is when the vehicle is above the second repeater and coupled only to that repeater becomes:

$$Z_1 = \frac{K_{24}^2}{Z_L + Z_{c4}}$$

$$Z_2 = \frac{K_{23}^2}{Z_{c3}}$$

$$Z_{in} = \frac{K_{01}^2}{\frac{K_{12}^2}{Z_1 + Z_2 + Z_{c2}} + Z_{c1}} + Z_{c0} \tag{3.8}$$

Impedance Z_2 is again large and therefore impedance Z_{in} in (3.8) is also large compared to the power supply output impedance. Therefore the load appears as if open-circuit to the supply and almost all the power is reflected back instead traveling to the load.

In case IV shown in Fig. 3.8, the vehicle arrives above the third repeater and is coupled only to that repeater. The impedance seen by the supply is only impedance Z_L inverted
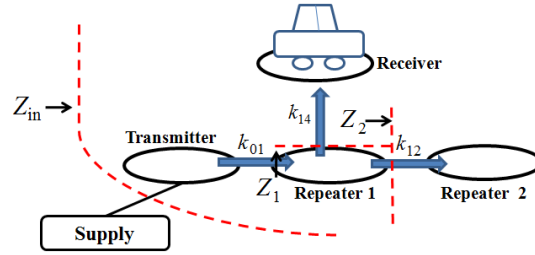
Figure 3.9: Case V analysis.

by each impedance inverter representations of coupling. Impedance Z_{in} is given by below equation and the power is transferred to the load.

$$Z_{in} = \cfrac{K_{01}^2}{\cfrac{K_{12}^2}{\cfrac{K_{23}^2}{\cfrac{K_{34}^2}{Z_L+Z_{c4}}+Z_{c3}}+Z_{c2}}+Z_{c1}}+Z_{c0} \qquad (3.9)$$

When the charging system contains even number of repeaters, the dead zones will occur as in to case I and case III. However the reason is not close to open-circuit condition but instead close to short-circuit condition. Case V as shown in Fig. 3.9 is an example of this condition. Impedance in this case can be calculated as:

$$
\begin{aligned}
Z_1 &= \frac{K_{14}^2}{Z_L+Z_{c4}} \\
Z_2 &= \frac{K_{12}^2}{Z_{c2}} \\
Z_{in} &= \frac{K_{01}^2}{Z_1+Z_2+Z_{c1}}+Z_{c0} \qquad (3.10)
\end{aligned}
$$

Impedance Z_2 is large and therefore impedance Z_{in} in (3.10) is close to zero. The power supply sees a close to short-circuit input impedance and therefore almost all power is reflected back and is not transferred to the load.

From above 5 analysis cases, when the charging system contains odd number of repeaters, the dead zones will occur when the receiver is coupled either only to the transmitter, second repeater or all other even number repeaters. On the other hand, when the

charging system contains even number of repeaters the dead zones will occur the receiver is coupled only to the first repeater or all other odd number of repeaters. This due to the open-circuit impedance is inverted odd number of times and the power supply will see an almost short-circuit input impedance.

3.5 Simulation Results

All five analysis cases are simulated using LTspice. Percentage reflected power, transferred power and power supply input impedance are plotted. Circuit parameters chosen are to be the same as experiment parameters given in the next section.

$$
\begin{aligned}
L_0 &= 9.2\,\mu\text{H} & C_0 &= 15\,\text{pF} \\
L_1 &= 9.3\,\mu\text{H} & C_1 &= 14.8\,\text{pF} \\
L_2 &= 9.1\,\mu\text{H} & C_2 &= 15.1\,\text{pF} \\
L_3 &= 9.65\,\mu\text{H} & C_3 &= 14.3\,\text{pF} \\
L_4 &= 9.2\,\mu\text{H} & C_4 &= 15\,\text{pF} \\
r_0 &= 1.1\,\Omega & r_4 &= 1\,\Omega \\
r_1 &= 1\,\Omega & R_0 &= 50\,\Omega \\
r_2 &= 1\,\Omega & Z_\text{L} &= 50\,\Omega \\
r_3 &= 1.1\,\Omega \\
\omega &= 2\pi \times 13.56\,\text{MHz} & & \text{(3.11)}
\end{aligned}
$$

The supply is outputting a.c power with 13.56 MHz resonant frequency. Term R_0 is the supply output impedance and all other symbols are the same as previous section.

3.5.1 Case I

The coupling coefficients in Fig. 3.5 are also chosen to be the same as the experiment:

$$\begin{aligned}
k_{01} &= k_{12} = k_{23} = 0.063 \\
k_{04} &= 0.065
\end{aligned}$$

From (3.1) and putting in all the parameters in (3.11), the characteristic impedance of the inverter representing each coupling coefficient is:

$$\begin{aligned}
K_{01} = 50\,\Omega \quad K_{23} = 50\,\Omega \\
K_{12} = 49\,\Omega \quad K_{04} = 51\,\Omega
\end{aligned}$$

The internal resistance of the coils at resonant frequency point:

$$\begin{aligned}
Z_{c0} = (1.1 + j1.4)\,\Omega \quad Z_{c3} = (1 + j1.4)\,\Omega \\
Z_{c1} = (1 - j0.7)\,\Omega \quad Z_{c4} = (1.1 + j1.4)\,\Omega \\
Z_{c2} = (1 - j2)\,\Omega
\end{aligned}$$

Putting in the values into (3.4) to (3.6), the calculated input impedance:

$$\begin{aligned}
Z_1 &= (51 - j1.4)\,\Omega \\
Z_2 &= (1152 - j378)\,\Omega \\
Z_{in} &= (1204 - j378)\,\Omega
\end{aligned}$$

From Fig. 3.10(a), reflection ratio η_{11} is high around frequency of interest, 13.56 MHz. The transfer ratio η_{21} to the load is nearly zero. This is due to high impedance seen by the supply as shown by the impedance plot in Fig. 3.10(b) and by above calculation.

3.5.2 Case II

The coupling coefficients in Fig. 3.6 are chosen to be:
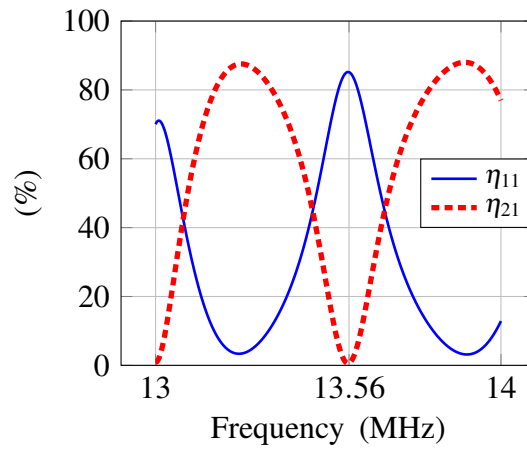
(a)
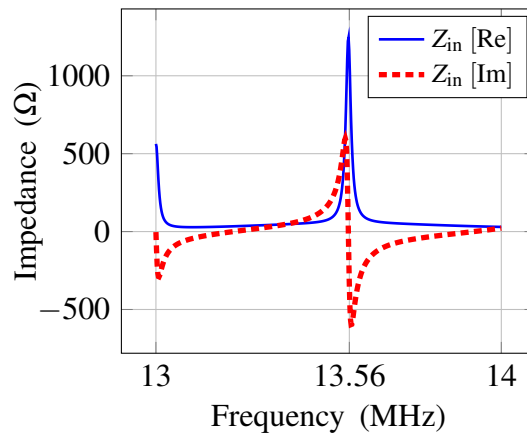
(b)

Figure 3.10: Simulation results of case I: a) transfer and reflection plot, b) input impedance.

$$k_{01} = k_{12} = k_{23} = 0.063$$
$$k_{14} = 0.065$$

Using the same calculation method as in Case I, the characteristic impedance of the inverter representing each coupling coefficient is:

$$K_{01} = 50\,\Omega \quad K_{23} = 50\,\Omega$$
$$K_{12} = 49\,\Omega \quad K_{14} = 51\,\Omega$$

Putting the values in (3.7), the calculated input impedance at resonant frequency point is:

$$Z_{\text{in}} = (48 + j2)\ \Omega.$$

In this case impedance seen by the supply is nearly 50 Ω at resonant frequency as shown by the impedance plot in Fig. 3.11(b) and by above calculation. Therefore reflection ratio η_{11} in Fig. 3.11(a) is close to zero. Most of the available power is being transferred to the load as shown by η_{21} plot. Some power is lost due to the internal resistance of the resonators.

3.5.3   Case III

The coupling coefficients in Fig. 3.7 are chosen to be:

$$k_{01} = k_{12} = k_{23} = 0.063$$
$$k_{24} = 0.065$$

The input impedance calculated for resonant frequency point is:

$$Z_{\text{in}} = (1163 - j344)\ \Omega$$
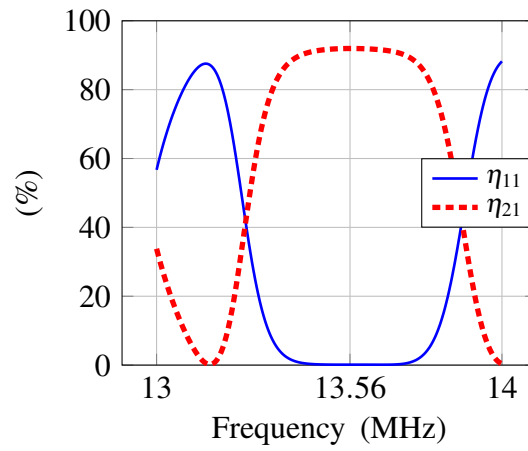
(a)
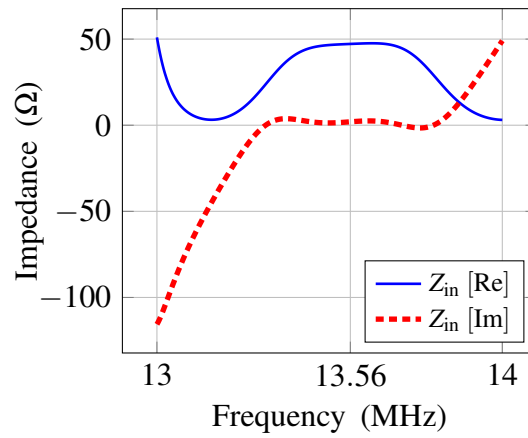
(b)

Figure 3.11: Simulation results of case II: a) transfer and reflection plot, b) input impedance.

Again the impedance seen by the power supply in this case is high compared to the output impedance as shown in Fig. 3.12(b). Therefore almost all the power is reflected as indicated by reflection ratio η_{11} plot in Fig. 3.12(a) and almost no power is being transferred to the load.

3.5.4 Case IV

The coupling coefficients of case IV are chosen to be:

$$
\begin{aligned}
k_{01} &= k_{12} = k_{23} = 0.063 \\
k_{34} &= 0.065
\end{aligned}
$$

In this case, the supply only sees one transmission path towards the load. The load impedance is inverted once with each repeater. Power is being transferred as indicated by the transmission ratio η_{21} plot in Fig. 3.13(a). As the input impedance is close to 50 Ω as shown in Fig. 3.13(b), the reflection ratio η_{11} is close to zero. Some power is lost due to the internal resistance of the resonators.

3.5.5 Case V

The coupling coefficients in Fig. 3.9 are chosen to be:

$$
\begin{aligned}
k_{01} &= k_{12} = 0.063 \\
k_{14} &= 0.065
\end{aligned}
$$

The input impedance calculated for resonant frequency point is:

$$
Z_{\text{in}} = (2.2 + j0.6) \ \Omega
$$

In this case, almost all the power is reflected as indicated by reflection ratio η_{11} plot in Fig. 3.14(a). Almost no power is transferred to the load as indicated by η_{21} plot. However the
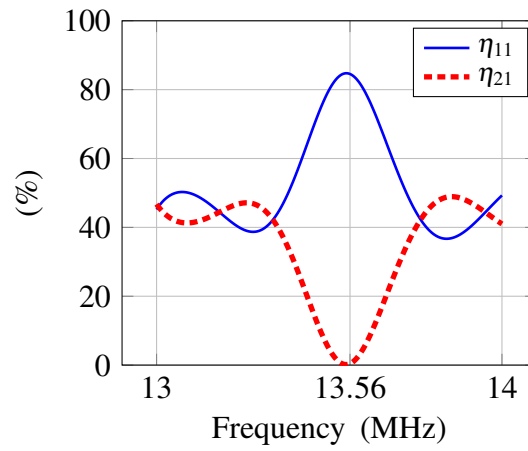
(a)
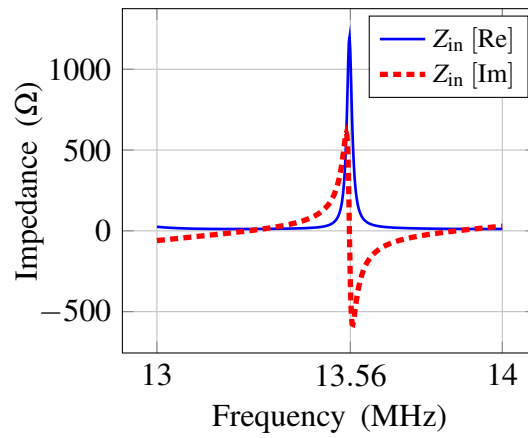
(b)

Figure 3.12: Simulation results of case III: a) transfer and reflection plot, b) input impedance.
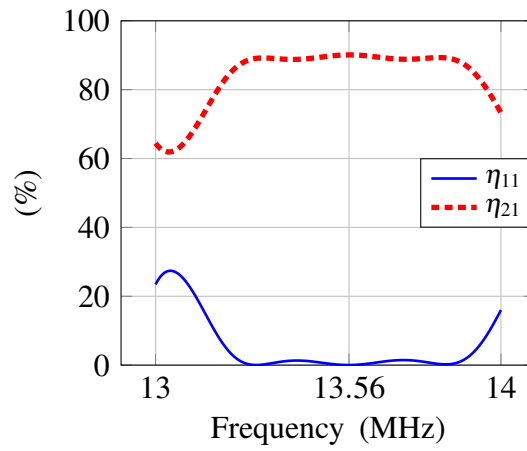
(a)
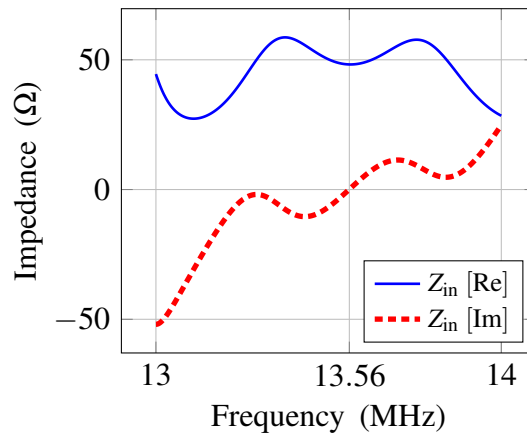
(b)

Figure 3.13: Simulation results of case IV: a) transfer and reflection plot, b) input impedance.

reason in this case is not due to high impedance but low impedance compared to output impedance seen by the power supply as shown by the plot in Fig. 3.14(b) and by above calculation.

3.6 Experiment Results

Experiments are performed for the simulated cases. The equipment used is Agilent Technologies vector network analyzer E5061B (VNA). All the coils are open type helical, 150 mm in radius, 5 mm in pitch, five copper wire turns and with internal resistance around $1\,\Omega$. They are tuned to resonate at $(13.56 \pm 0.01)\,$MHz. Transmitter and repeaters are arranged side by side horizontally to simulate a small section of charging lane. The experiment setup is shown in Fig. 3.15. The receiver is placed 19 cm vertically above the transmitter or each repeater for different cases. For case I to case IV, three repeaters are used and for case V, only two repeaters are used. Coupling coefficients and coil measurements are the same as the values given in the simulation results section. The repeaters are shorted using BNC shorting plug. Port-1 of VNA which acts as source is connected to the transmitter. The receiver is connected to the port-2 of the VNA to measure the power received. Reflected power ratio and input impedance are also read from the VNA. Two port calibration is performed to eliminate the cable effects and other errors [85]. The calibration kit used is Agilent 85032F Type N.

In actual experiment, the resonant frequency tends to shift when the system consists of more resonators as indicated in the plot of Fig. 3.16. This may be due to small cross coupling existing among the coils. Although all the coils are tuned before experiment, small shift in resonant frequency occurs when the polystyrene gap and receiver are placed on the transmitter or each repeater. In the experiment measurements, the peak impedance is shifted as shown in Fig. 3.10(b). Nevertheless, the input impedance, Z_{in} around the resonant frequency is still high compared to $50\,\Omega$ output impedance causing high reflection ratio and low transmission ratio. At 13.56 MHz point, Z_{in}, η_{11}, and η_{21} $(111 - j228)\,\Omega$, 72% and 14% respectively.
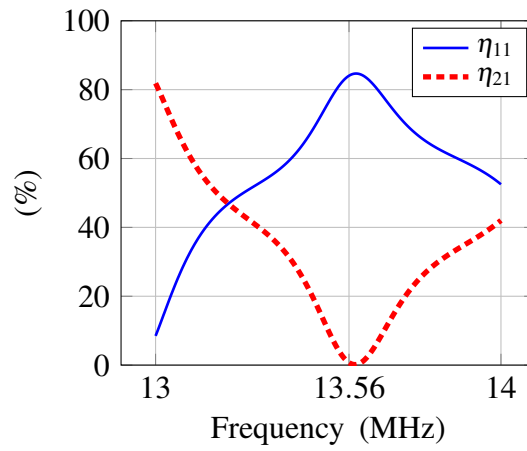
(a)
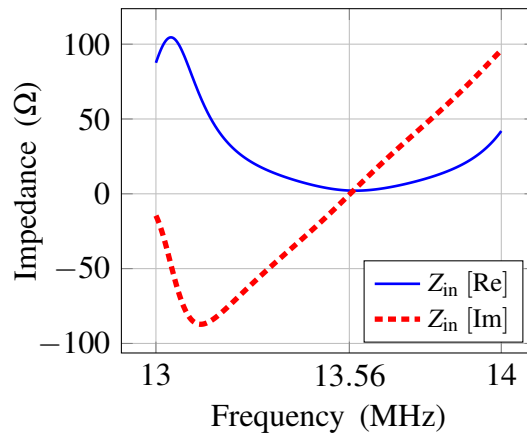
(b)

Figure 3.14: Simulation results of case V: a) transfer and reflection plot, b) input impedance.
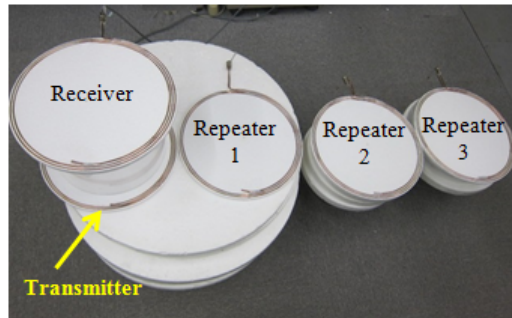
Figure 3.15: Experiment setup.

In case II, the repeater impedance path is close to zero. The power supply sees the impedance path towards the load which is close to $50\,\Omega$ around resonant frequency. Reflection ratio is close to none, and almost all available power is able to be transferred to the load as shown in Fig. 3.17

Similar to case I, the peak impedance in the experiment results is shifted. However, the high imaginary impedance in the region around resonant frequency causes most of the power being reflected and not transferred to the load as shown in Fig. 3.18. The input impedance seen by the power supply in this experiment is $(57 - j231)\,\Omega$, the reflection ratio is 83% whereas the transmission ratio is close to zero.

In case IV, the receiver is at the end of the charging system. The power supply only sees one impedance path towards the receiver which is close to $50\,\Omega$ as shown in Fig. 3.19. Almost all power is transferred to the load as shown by the reflection ratio and transmission ratio plot.

Only two repeaters are used in case V, and the receiver is above the first repeater. As shown in plot of Fig. 3.20, the transmission ratio is low at 13.56 MHz. However in this case, this is due to the low impedance seen by the power supply. Similar to above cases, the frequency response is shifted compared to simulation, and the input impedance is $(3 - j7)\,\Omega$ which is slightly higher than the calculations.
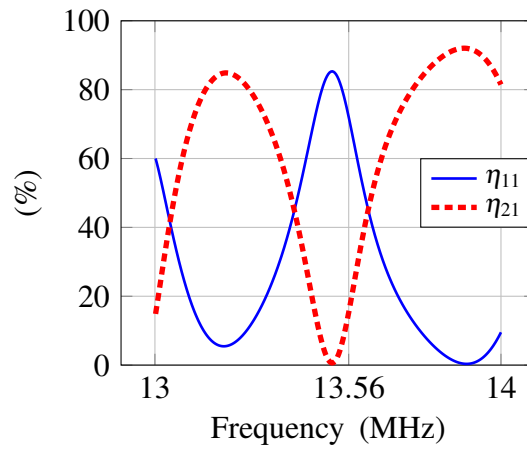
(a)
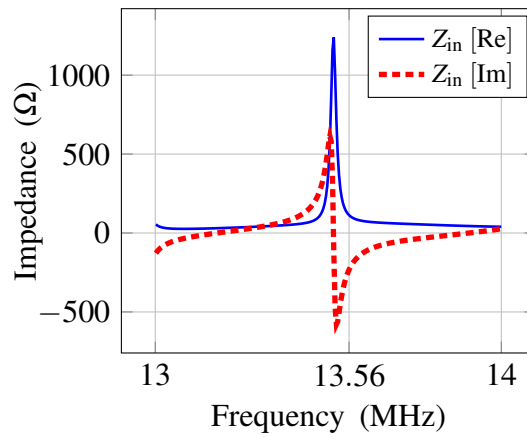
(b)

Figure 3.16: Experiment results of case I: a) transfer and reflection plot, b) input impedance.
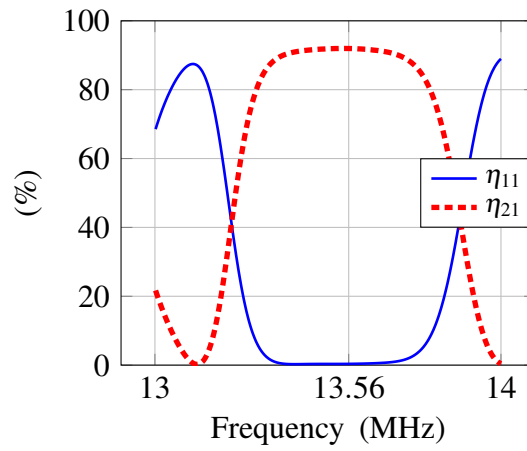
(a)
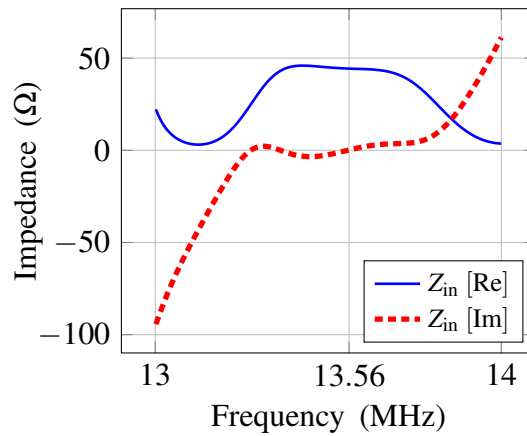
(b)

Figure 3.17: Experiment results of case II: a) transfer and reflection plot, b) input impedance.
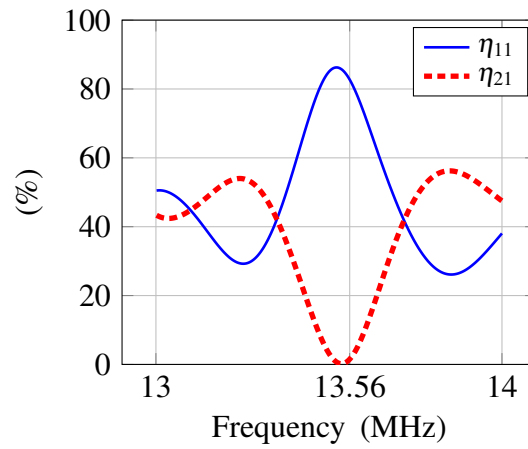
(a)
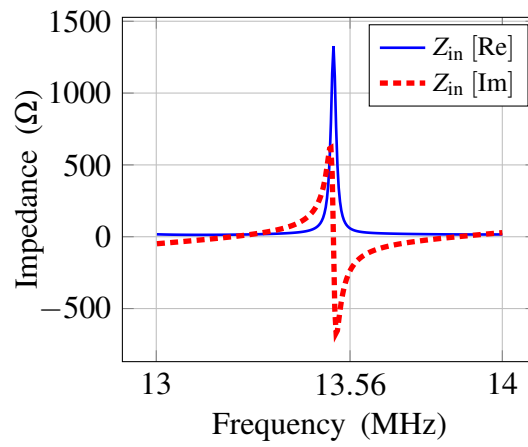
(b)

Figure 3.18: Experiment results of case III: a) transfer and reflection plot, b) input impedance.
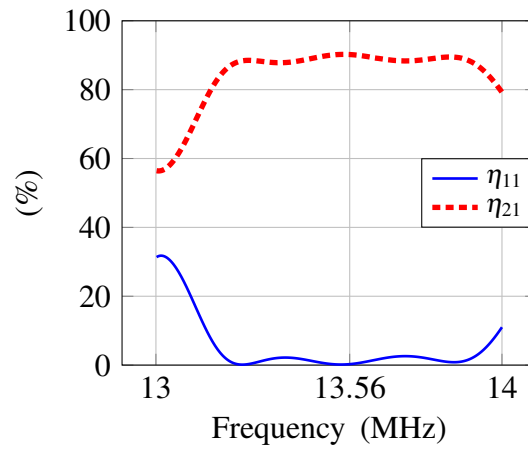
(a)
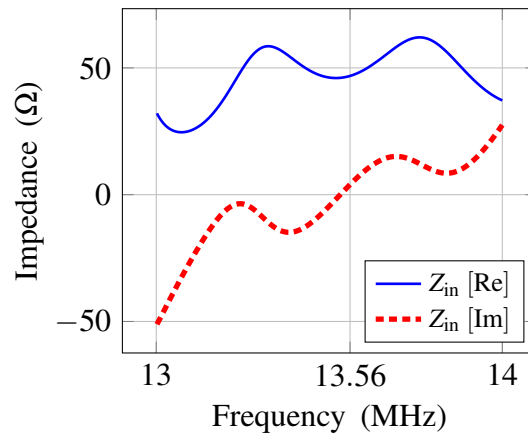
(b)

Figure 3.19: Experiment results of case IV: a) transfer and reflection plot, b) input impedance.
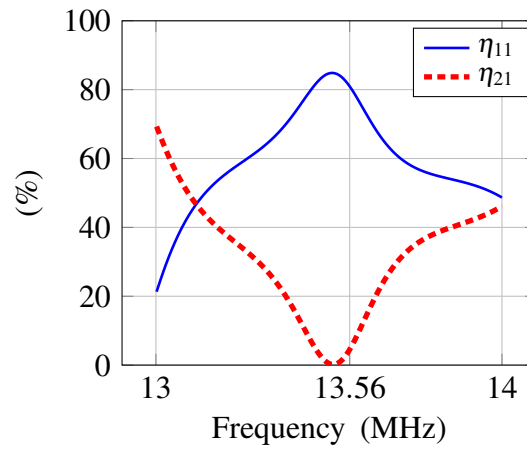
(a)
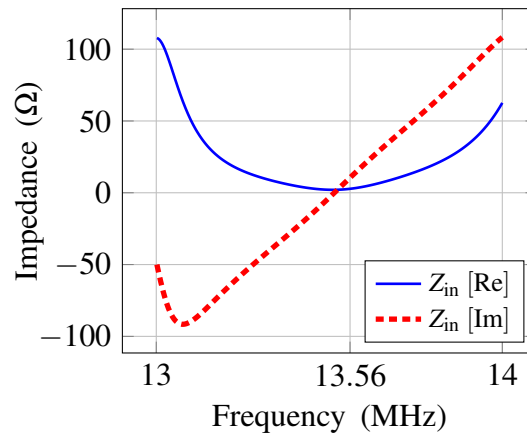
(b)

Figure 3.20: Experiment results of case V: a) transfer and reflection plot, b) input impedance.

3.7   Chapter Summary

This paper shows a mathematical explanation of the dead zones observed in a wireless power transfer system for moving vehicles containing repeaters. Wireless charging system for moving vehicle contains transmitter and repeaters arranged along the road. However, the mentioned dead zone condition appears when the vehicle is above interval of resonators. This paper provides mathematical explanation on the condition by using impedance inverter representations and generalizes the findings to arbitrary number of repeaters.

When the system contains odd number of repeaters and the receiver is coupled either only to the transmitter, or one of the even number repeaters, the small impedance of the repeaters is inverted and is in series with the load. The power supply views an almost open-circuit input impedance and therefore almost no power is being transferred to the load. When the charging system contains even number of repeaters and the receiver is coupled only to one of the odd number repeater, the small impedance of the repeaters is also inverted and is in series with the load. This series impedance is then inverted odd number of times towards the power supply and the total input impedance in this case will be close to short-circuit instead.

Although in actual experiment the resonant frequency of the system tends to shift, the input impedance, transmission ratio and reflection ratio in the region around the resonant frequency still agree with the mathematical findings. Future work of this study will include effect of internal resistance and cross coupling and combining the results to derive an optimized solution for the dead zone condition.

Chapter 4

Even Magnetic Field Design for Dynamic Charging

In this chapter, a practical configuration suitable for on-road implementation is proposed. Even magnetic field is achieved via the coupled coil design and the power transferred can be used to power motors directly. In real highways, RFID sensors can be used to activate transmitters when the vehicle is approaching and also for billing the users. Magnetic sensors are implemented in place of RFID sensors in this experiment to prove the method. Neumann formula and maximum efficiency formula are used to explain the relationship between the size of static transmitters and the efficiency of the wireless power transfer system. When coupling large transmitters with small receiver, the maximum efficiency is reduced compared to symmetry coils. Therefore, multiple small transmitters connected in parallel via impedance inverter LCL circuit to ensure high transfer efficiency is proposed. With impedance inveter, the current flowing in the transmitters is constant regardless of the load and cross coupling between transmitters. Design of the physical dimension of the coils to achieved desired nominal power level is also discussed. The gap between the transmitters is designed to achieve even magnetic field coupling to the receiver.
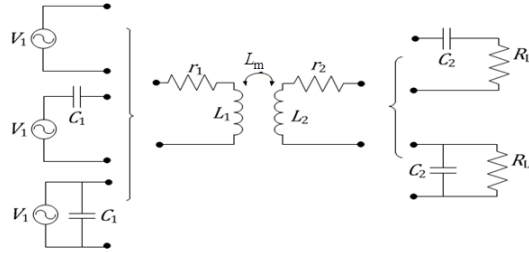
Figure 4.1: Compensation methods of wireless power transfer [86].

4.1 Coil Consideration in terms of Maximum Efficiency

4.1.1 Maximum Efficiency Formula

The equivalent circuits of six basic compensation methods are shown in Fig. 4.1. They are the series-series, series-parallel, parallel-series, parallel-parallel, uncompensated primary-series and uncompensated primary-parallel. The maximum efficiency of all six configurations is given in (4.1) [86].

$$\eta_{\text{max}} = \frac{X}{(1 + \sqrt{1 + X})^2} \tag{4.1}$$

where

$$X = k^2 Q_1 Q_2 = \frac{(\omega_0 L_{\text{M}})^2}{r_1 r_2} \tag{4.2}$$

and k is the coupling coefficient, Q_1 and Q_2 are the quality factors of the transmitter and receiver respectively.

Equation (4.1) tells us that the maximum efficiency will be close to 1 if X is much larger than 1. Mutual inductance, L_{M} is calculated using Neumann formula which will be explained in the next subsection. Coil resistance r_1 and r_2 are obtained from real measurements.
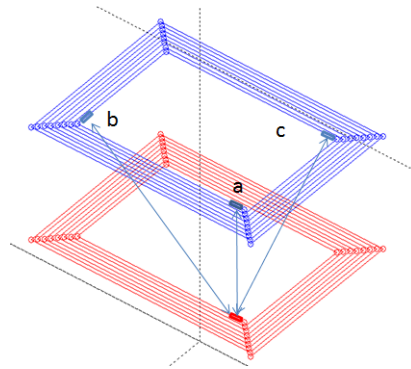
Figure 4.2: Neumann formula calculation method.

Figure 4.3: Fabricated three-meter coil and receiver coil.

4.1.2   Neumann Formula

Mutual inductance between two coupled coils is given in (4.3) where the coils are divided into small sections shown in Fig. 4.2.

$$L_{\mathrm{M}} = \frac{\mu_0}{4\pi} \oint_{C_1} \oint_{C_2} \frac{dl_1 . dl_2}{D} \tag{4.3}$$
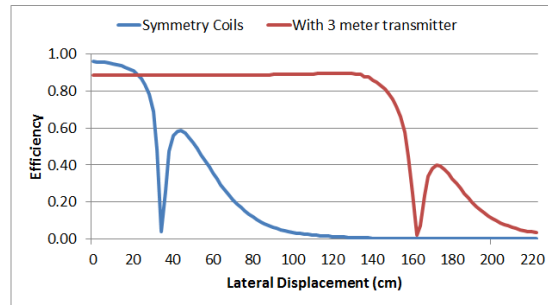
Figure 4.4: Plot of maximum efficiency vs. lateral displacement.

dl_1 and dl_2 are the differential length of these small sections of transmitter and receiver respectively. Term D is the distance between the sections. Mutual inductance is sum of mutual inductance contributed by each of these small sections.

The receiver coil is chosen to be 40 x 40 cm which is the size commonly used in both dynamic and static wireless power transfer at the vehicle side [59]. Transmitter length is extended to achieve larger charging coverage. The overlapping area of the coils is similar with using identical transmitter and receiver case. The resulted mutual inductance is similar, however with a longer transmitter, the coil resistance is larger. From Neumann calculations, when using identical coils and with 10 cm vertical gap, the mutual inductance is 22.98 μH and the coil resistance is measured to be 0.26 Ω. Therefore using (1) and (2), the maximum efficiency is 95.9%. A 10 turn, (40x300) cm transmitter shown in Fig. 4.2 is fabricated and the coil resistance is measured to be 1.52 Ω. The mutual inductance calculated using Neumann formula when placing the (40x40) cm receiver 10 cm above the middle of long transmitter is 19.41 μH and the maximum efficiency is reduced to 88.6%. Fig. 4.4 shows the efficiency plot vs. lateral displacement of the receiver when the vertical gap is 10 cm. The 0 cm point is referring to the center of transmitter. If longer transmitter is used, the maximum efficiency will tend to reduce further.

4.2 Two transmitters to One Receiver with LCL

Since coupling a long transmitter with small receiver results in low efficiency and may cause field leakage to the environment, simultaneous charging from two small transmitters
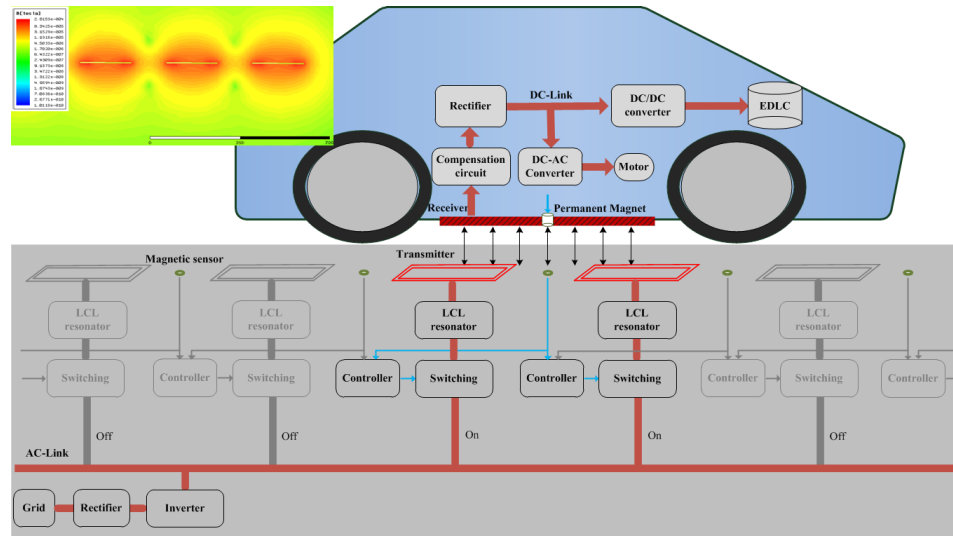
Figure 4.5: System overview of the proposed method.
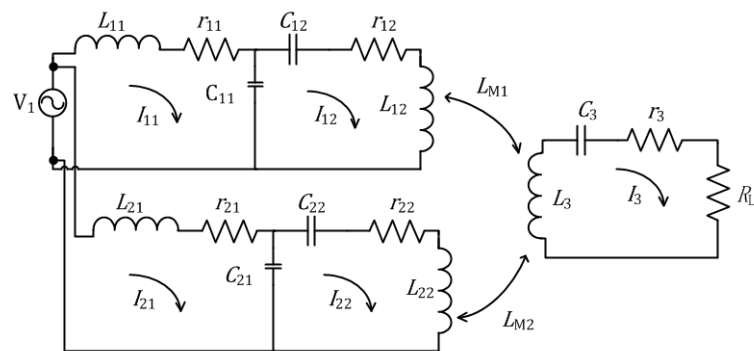
Figure 4.6: Equivalent circuit of the proposed method.

is proposed. Fig. 4.5 shows an illustration of the proposed method where the transmitter coils are arranged along the ground. When the receiver is above the first transmitter and second transmitter, these two transmitters are activated. When the receiver is moving towards the third transmitter, the second and third transmitter are activated and so on. LCL circuit is used for each transmitter to allow multiple small transmitters to be connected in parallel to a common inverter. Constant current is achieved in the transmitters and the low coupling condition or no-load condition will not short circuit the inverter. The combination of two transmitters results a flatten magnetic field coupled to the receiver as also shown in Fig. 4.5.

Fig. 4.6 shows the equivalent circuit of the proposed wireless power transfer system. The components at the primary side are designed such that:

$$
\begin{aligned}
\omega_0 L_{11} &= \frac{1}{\omega_0 C_{11}} = \omega_0 L_{12} - \frac{1}{\omega_0 C_{12}} \\
\omega_0 L_{21} &= \frac{1}{\omega_0 C_{21}} = \omega_0 L_{22} - \frac{1}{\omega_0 C_{22}} \\
Z_{11} &= r_{11} + j(\omega_0 L_{11} - \frac{1}{\omega_0 C_{11}}) \approx 0 \\
Z_{21} &= r_{21} + j(\omega_0 L_{21} - \frac{1}{\omega_0 C_{21}}) \approx 0
\end{aligned}
\tag{4.4}
$$

Resistor r_{11} and r_{21} are the parasitic resistance of the inductor L_{11} and L_{21} respectively and is assumed to be sufficiently small. Looking at the I_{11} and I_{21} current loop:

$$
\begin{aligned}
V_1 &= Z_{11} I_{11} + \frac{j}{\omega_0 C_{11}} I_{12} \\
V_1 &= Z_{21} I_{21} + \frac{j}{\omega_0 C_{21}} I_{22}
\end{aligned}
\tag{4.5}
$$

Since impedance Z_{11} and Z_{21} are zero, transmitter current I_{12} and I_{22} are constant. Furthermore applying the same design in every parallel branch and from the I_3 current loop:

$$
\begin{aligned}
I_{12} &= I_{22} \\
0 &= I_3(R_L + r_3) + j\omega_0 L_{M1} I_{12} + j\omega_0 L_{M2} I_{22} \\
I_3 &= -\frac{j\omega_0(L_{M1} + L_{M2})}{(R_L + r_3)} I_{12}
\end{aligned}
\tag{4.6}
$$

where secondary resonance is implemented:

$$
j\left(\omega_0 L_3 - \frac{1}{\omega_0 C_3}\right) = 0
\tag{4.7}
$$

Since the transmitter current is constant, receiver current I_3 will be constant if we can ensure the sum $(L_{M1} + L_{M2})$ is constant when the vehicle is moving along the dynamic charging lane. Thus power received by the load will also be constant.

4.2.1 Efficiency Analysis

The transfer efficiency is given in (4.8).

$$
\eta = \eta_{\text{pri}} \times \eta_{\text{sec}}
\tag{4.8}
$$

where

$$
\eta_{\text{sec}} = \frac{R_L}{R_L + r_3}
\tag{4.9}
$$

and

$$
\eta_{\text{pri}} = \frac{|I_3|^2(R_L + r_3)}{|I_3|^2(R_L + r_3) + |I_{12}|^2(r_{12}) + |I_{22}|^2(r_{22})}
\tag{4.10}
$$

Substituting (4.6) into (4.10) and cancelling the common terms, we obtain:

$$
\eta_{\text{pri}} = \frac{\frac{(\omega_0 L_{M1} + \omega_0 L_{M2})^2}{(R_L + r_3)}}{\frac{(\omega_0 L_{M1} + \omega_0 L_{M2})^2}{(R_L + r_3)} + r_{12} + r_{22}}
\tag{4.11}
$$

Equation (4.8), (4.9) and (4.11) have the same structure as the series-series wireless power transfer. Therefore the same maximum efficiency equation with modification can be
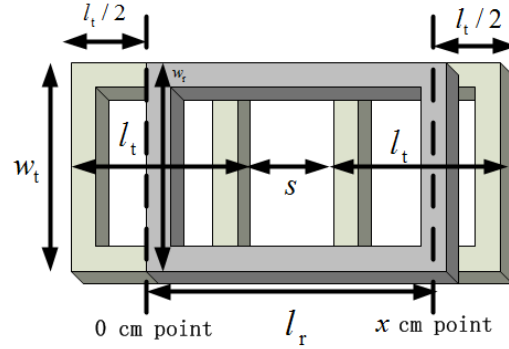
Figure 4.7: Coil dimension.

used. In this two transmitter case, the maximum efficiency is the same as (4.1). However the X is now given as:

$$X = \frac{(\omega_0 L_{M1} + \omega_0 L_{M2})^2}{(r_{12} + r_{22})r_3} \tag{4.12}$$

and the load for maximum efficiency is:

$$R_{Lmax} = \sqrt{r_3 \left[\frac{(\omega_0 L_{M1} + \omega_0 L_{M2})^2}{r_{12} + r_{22}} + r_3 \right]} \tag{4.13}$$

Equation (4.13) is the modified version of the maximum efficiency load equation from [45].

4.2.2 Coupling Coil Size

Fig. 4.7 shows the physical parameters of the coupling coils including the spacing between adjacent transmitters. The lateral coverage between two consecutive transmitters depends on the receiver size. Considering that the overlapping area of the receiver and the transmitter coil contributes dominantly to the mutual inductance, the smaller coil size determines the sum of mutual inductance, $L_{M1} + L_{M2}$. According to (4.6), $L_{M1} + L_{M2}$ determines the constant current in the receiver, I_3. In order to achieve even magnetic field, the design conditions are:

1. The receiver size is first designed according to space limitation.

Table 4.1: Dimension of the transmitters in Fig. 4.7.

Transmitter	w_t(cm)	l_t(cm)	s (cm)	end point position, x (cm)
(a)	40	10	26	36
(b)	40	20	16	36
(c)	40	30	6	36
(d)	40	40	-2	38
(e)	40	50	-4	46
(f)	40	60	-4	56

2. The smaller coil in terms of either width (w_r or w_t) and length, (l_r or l_t) determines the sum of mutual inductance, $L_{M1} + L_{M2}$.

3. If the transmitter is smaller in length than the receiver, the space, s between transmitters should be approximately equal to length of the receiver, l_r minus the length of the transmitter, l_t.

4. If the transmitter is larger in length than the receiver, the space, s is approximately zero. Overlap of transmitters maybe be required and results in negative s value.

Different transmitter designs to achieve constant power during dynamic charging are discussed. The receiver is with l_r and w_r equal to 40 cm mentioned in the last section. Mutual inductance is calculated using Neumann formula. Fig. 4.8 shows the sum of mutual inductance, $L_{M1} + L_{M2}$ when the receiver moves along the charging lane. The width of all the transmitters, w_t is 40 cm, the length, l_t and spacing, s for different transmitters are listed in Table 4.1. The chosen spacing, s is approximately equals to l_r- l_t or zero if transmitter length is equal or larger than receiver. Adjustment of +/-4 cm has been made by trial and error. Overlap of transmitters may occur when transmitter is larger and is represented by negative s value. Sum of mutual inductance increases with transmitter size and saturates when the transmitter size is equal to the receiver size. Charging coverage, x is approximately equals to the receiver length, l_r. Further increased in transmitter length, l_t will only increase the charging coverage. Larger transmitters simplify the underground installation, however the efficiency will be lower as discussed in the Section 4.1.2.
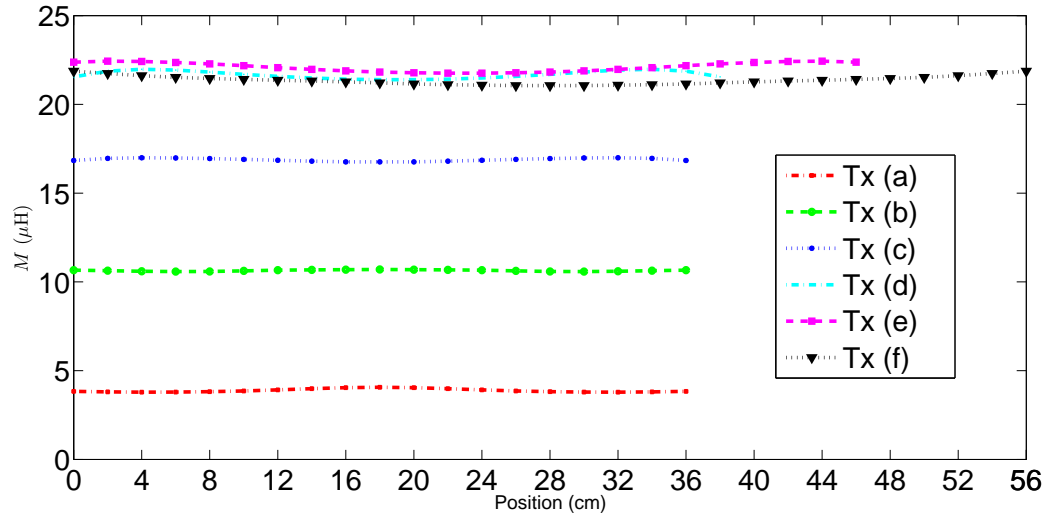
Figure 4.8: Plot of sum of mutual inductance with different transmitter designs vs. lateral positions.

4.2.3 Experiment

Fig. 4.9 shows the coils used for the experiment to verify the proposed method. The dimension of the receiver is (40×40) cm and transmitter (b) from Table 4.2.3. The component parameters are listed in Table III. The horizontal gap between two transmitters is chosen such that the sum $(L_{M1} + L_{M2})$ is constant where L_{M1} is the mutual inductance between the receiver and the left transmitter and L_{M2} is the mutual inductance between the receiver and the right transmitter. Both the transmitters are identical and the vertical gap is 10 cm.
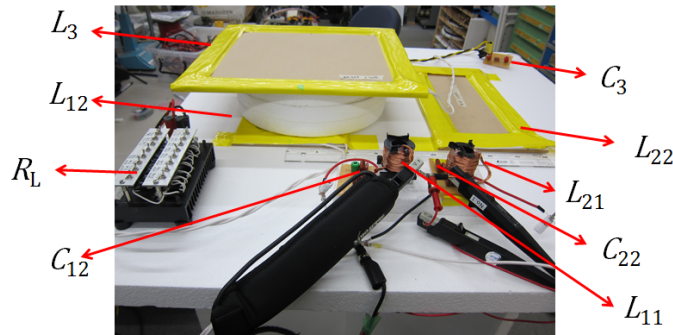
Figure 4.9: Experiment setup.

Table 4.2: Parameter List.

Parameter	Value
V_1	30 V
L_{11}	30 μH
r_{11}	0.1 Ω
C_{11}	110 nF
L_{12}	55.3 μH
r_{12}	0.25 Ω
C_{12}	136 nF
L_{21}	30 μH
r_{21}	0.1 Ω

Parameter	Value
C_{21}	110 nF
L_{22}	56 μH
r_{22}	0.26 Ω
C_{22}	136 nF
L_3	88.9 μH
r_3	0.33 Ω
C_3	38.5 nF
R_L	5 Ω
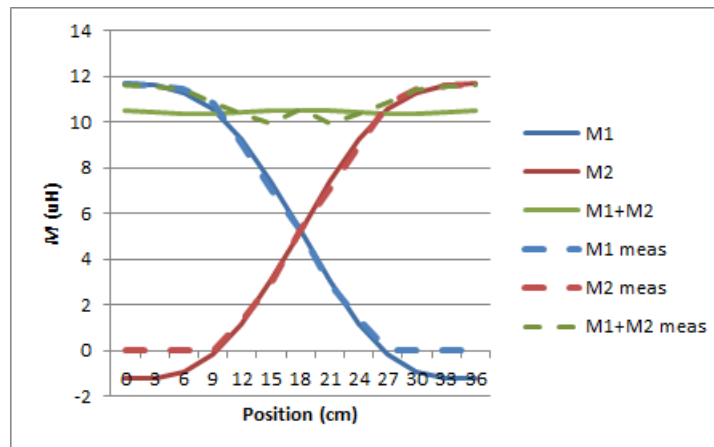
Figure 4.10: Mutual inductance plots.
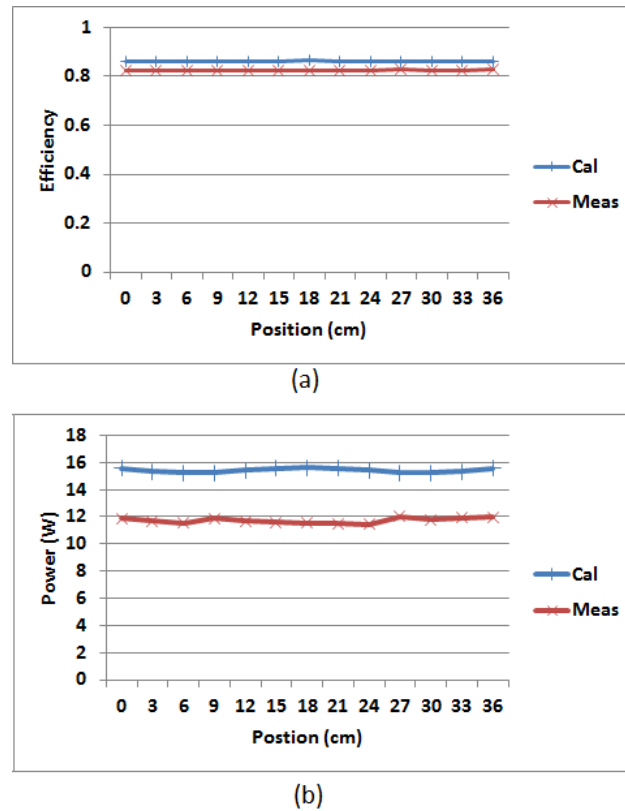
Figure 4.11: (a) Transfer efficiency and (b) power for 0 cm point to 36 cm point.

Plots in Fig. 4.10 show the mutual inductance and the horizontal axis is the position of the center of the receiver. The 0 cm point and 36 cm point are indicated in Fig. 4.7. The solid lines are the calculation data using Neumann Formula implemented in Matlab. The dotted lines are the measurement data using open-short method with a LCR meter. As shown by the plots, the measurement data matches with the calculation data except for the negative mutual inductance region where the open-short method is not valid.

The power supply used is NF HSA4014 high speed bipolar amplifier and the 85 kHz square wave input reference is provided by Tektronix AFG3021 arbitrary/function generator. The voltage and current waveforms are captured using Tektonix MSO3034 mixed signal oscilloscope. Power and efficiency measurements are performed using NFL PPA5530 precision power analyzers. Efficiency plots in Fig. 4.11(a) show that the efficiency remains constant when the center of the receiver travels from 0 cm point to 36 cm point. The
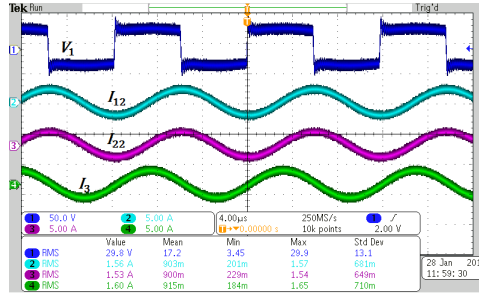
Figure 4.12: Source voltage, V_1, current in the transmitters, I_{12}, I_{22} and current in the receiver, I_3.

measurement data is close enough to calculation data. R_L is chosen to be the optimized load, 5 Ω. The power plots are shown in Fig. 4.11(b), the power across R_L remains constant throughout the experiment region. The lower measured power is due to the reactive impedance seen by the power source that is not accounted by the derived equations. The imaginary impedance is caused by the imperfect matching and harmonics that is present at the power source. Compared to SS configuration, where the resonant circuit is connected directly to the source, these harmonics from square wave voltage output is not filtered at the source.

The voltage source waveform, current waveforms of the transmitters, current I_{12} and current I_{22}, and receiver I_3 are shown in Fig. 4.12. These waveforms remain nearly unchanged throughout the lateral displacement experiment therefore only one of them is shown. The amplitude of the square wave is 30 V and taking only the fundamental components and according to (4.5) the rms transmitter current are:

$$I_{12} = I_{22} = \frac{4}{\sqrt{2} \times \pi} \times jV_1\omega_0 C_{11} = j1.69\,\text{A} \tag{4.14}$$

and according to (4.6), the calculated rms receiver current is

$$I_3 = 1.77\,\text{A} \tag{4.15}$$

where $L_{M1} + L_{M2}$ is taken to be in average of 10.44 μH. The measurements show the actual results are slightly lower than calculation results.

4.3 Chapter Summary

When coupling long coils with small coils of general size EVs, transfer efficiency tend to be lower. This phenomenon is explained using Neumann formula and maximum efficiency formula. Additionally, leakage field may occur as the activated transmitter is not fully covered by the vehicles. However long coils are able to provide steady power flow for certain distance. Therefore, simultaneous power transfer from two short transmitters is proposed to emulate the long coils. LCL circuit is used in each transmitter to allow inverter sharing. The coil arrangement is designed such that, the sum of mutual inductance between the receiver and first transmitter and mutual inductance between the receiver and second transmitter is constant. In this way, receiver is able to receive almost constant power while moving along the dynamic charging lane. The proposed configuration is verified by experiments.

Chapter 5

Steady and Transient State Design of Wireless Power Transfer

5.1 Circular Spiral Coil

In dynamic charging, different power levels are required from the wireless power transfer system. Reference [59] lists the power level during acceleration, deceleration, and various speeds for light and heavy vehicles. Voltage source is fixed at the transmitter side to simplify the construction of ground facility. In this chapter, one-to-one wireless power transfer, series-series compensated wireless power transfer is discussed in terms of steady power and efficiency. Modeling method for ac and dc section of wireless power transfer is also discussed. Furthermore, two power control methods are then proposed using the secondary side dc/dc converter as a preliminary review.

5.1.1 Power and Efficiency Characteristic

Fig. 5.1 shows the equivalent circuit of wireless power transfer. The dc/dc converter control secondary side voltage V_2 and the effective resistance, R_L can be controlled through following equations.

$$A_V = \frac{V_2}{V_1} = \frac{\omega_0 L_m R_L}{r_1 r_2 + r_1 R_L + (\omega_0 L_m)^2} \tag{5.1}$$
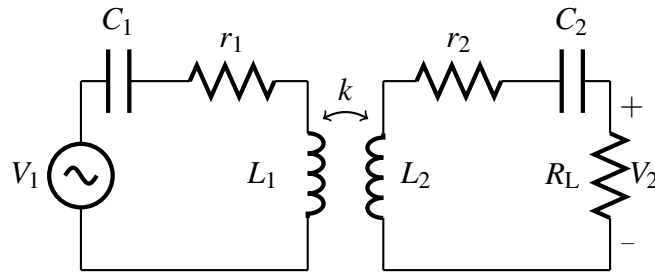
Figure 5.1: Equivalent circuit of the wireless power transfer.

where

$$k = \frac{L_m}{\sqrt{L_1 L_2}} \tag{5.2}$$

$$\omega_0 = 2\pi \times 85\,\text{kHz} \tag{5.3}$$

and capacitor values are always chosen such that

$$C_1 = \frac{1}{\omega_0^2 L_1} \tag{5.4}$$

$$C_2 = \frac{1}{\omega_0^2 L_2} \tag{5.5}$$
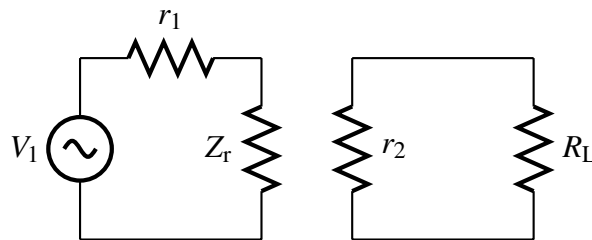
Figure 5.2: Equivalent circuit of the wireless power transfer when in resonance.

As the primary and secondary sides are in resonance, we can omit the reactance values and study the loss using the resistance values that appear in different parts of the circuit shown in Fig. 5.2. Z_r is the reflected impedance from the secondary to the primary [87, 88].

$$Z_r = \frac{(\omega_0 L_m)^2}{r_2 + R_L} \tag{5.6}$$

Transmission efficiency of the wireless power transfer, η is then the efficiency of the primary coil, η_1 multiply the efficiency of the secondary coil, η_2.

$$\eta = \eta_1 \times \eta_2 = \frac{Z_r}{r_1 + Z_r} \times \frac{R_L}{r_2 + R_L} \tag{5.7}$$

The power received by the effective load:

$$P_{norm} = \eta \times \frac{1}{r_1 + Z_r} \, (W/V^2) \tag{5.8}$$

where P_{norm} is the power normalized against V_1^2 and the power received by equivalent load R_L is:

$$P = P_{norm} \times V_1^2 \tag{5.9}$$
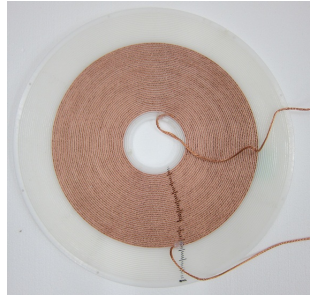
Figure 5.3: Spiral coil wounded using Litz wire.

Consider a wireless power transfer using identical coils shown in Fig. 5.3 to transfer across 25 cm gap. The coils are wounded on Duracon plastic frame using Litz wire consists of 301 strands of individual cooper wire, divided into seven bunches that are twisted together. The Litz wire reduces skin-effect losses and proximity effect losses in high frequency signal [89] compared to a solid round wire. The diameter of the conductor is 1 mm and the diameter of the individual strand is 0.1 mm. Other parameter values are given

Table 5.1: Parameter values of coil in Fig. 5.3.

Gap	25 cm
Turn, n_1, n_2	40
L_1, L_2	337 μH
r_1, r_2	0.56 Ω
D_{in}	10 cm
D_{out}	34 cm
f	85 kHz
k	0.055
Q_1, Q_2	326
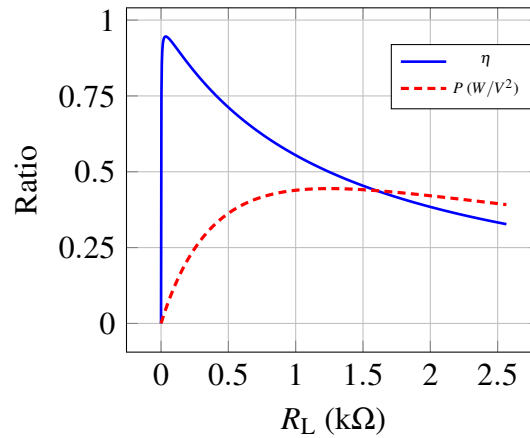
Figure 5.4: Efficiency and power vs R_{L}.

in Table 5.1 and are inputted into (5.7) to (5.8). The self inductance of the coils, L_1 and L_2, and coupling coefficient is calculated using Neumann formula discussed in the previous chapter. The internal resistance of the Litz wire wounded coils is approximated using extended Dowell method [91] for helical coils.

The efficiency and normalized power plots when effective load R_{L} is changing are given in Fig. 5.4. When R_{L} is small, the efficiency increase sharply with increasing R_{L}. The expanded view of this region is given in Fig. 5.5 and the efficiency is separated to primary contribution and secondary contribution. At small value of R_{L}, η_1 in (5.7) is high and the loss is mainly due to the secondary coil. As r_2 is less than 1 Ω, the efficiency increases rapidly as R_{L} rises to a few ohms. This region of operation is undesirable due to the
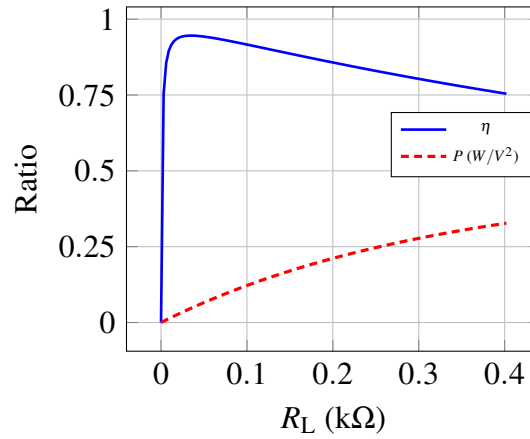
Figure 5.5: Expanded plot at small region of R_L.

heat loss occurs in the vehicle side which is surrounded by other mechanical and electrical parts. Furthermore, the change in efficiency is steep and small decrease in R_L will cause the efficiency to drops significantly. Secondary efficiency, η_2 is ignorable when R_L is further increased. At this time, the total efficiency decreases mainly due to the decrease of η_1. Normalized power, P_{norm}, on the other hand is increasing due to the second term in (5.8) until the maximum power is reached. At this point, efficiency is too low and power does not increase. The optimal operating region is then from the maximum efficiency point towards the right side of the plot until the acceptable efficiency level is reached. For this system, the normalized power at the maximum efficiency point is 0.09. Given the chosen input voltage 120 V, the power transferred is 1296 W and the efficiency is 89% at this point.

The required range of R_L is realizable by choosing the proper dc/dc converter. We can design the coil parameters by omitting R_L and looking only at the efficiency vs. desired power level plot shown in Fig. 5.6. The efficiency changes considerably for different power levels. In order to design the coils optimized for desired power level, two figures of merit are proposed.
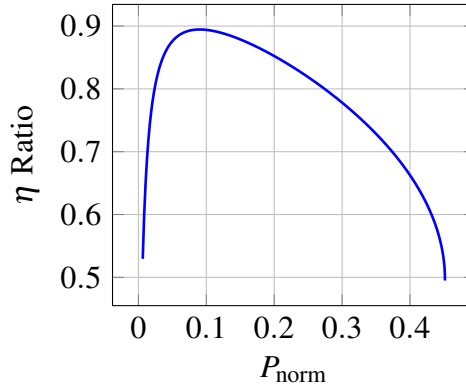
Figure 5.6: Efficiency vs. desired power level.

5.1.2   The Figure of Merit (FOM)

The maximum efficiency is given as:

$$\eta_{\mathrm{max}} = \frac{X}{(1 + \sqrt{1 + X})^2} \tag{5.10}$$

where

$$X = k^2 Q_1 Q_2 = \frac{(\omega_0 L_{\mathrm{M}})^2}{r_1 r_2} \tag{5.11}$$

and

$$Q_1 = \frac{\omega_0 L_1}{r_1},\ Q_2 = \frac{\omega_0 L_2}{r_2},\ k = \frac{L_{\mathrm{m}}}{\sqrt{L_1 L_2}} \tag{5.12}$$

The maximum efficiency equation is the same equation given in Chapter 4, however we will use the equation specifically for series-series compensated wireless power transfer in this chapter. From (5.10), term $k^2 Q_1 Q_2$ should be as large as possible compared to 1 and maximum efficiency, η_{max} will be close to 1 or 100%. First figure of merit, FOM1, $x = k^2 Q_1 Q_2$ determines the highest point in Fig. 5.6 and is in terms of quality factor of primary coil and secondary coil and the coupling coefficient between the two coils.

The normalized maximum power against squared of source voltage, V_1 is given as [45]

$$P_{\mathrm{max}}/V_1^2 = \frac{1}{4r_1[1 + \frac{r_1 r_2}{(\omega_0 L_{\mathrm{m}})^2}]} = \frac{1}{4r_1[1 + \frac{1}{X}]} \approx \frac{1}{4r_1} \tag{5.13}$$

The second figure of merit, FOM2 is equal to $\frac{1}{4r_1}$ which is the approximate maximum power. Term $\omega_0 L_\mathrm{m}$ is typically more than 10 Ω for charging electric vehicles as L_1 and L_2 are in the range of few hundreds μH and k is in medium range (>0.05) to ensure high efficiency. Therefore the second term of the denumerator is usually much smaller compared to 1. FOM2 depends only on the internal resistance of transmitter coil. We can exploit the characteristic of FOM1 and FOM2 to achieve flatter efficiency across different power levels.

In order to demonstrate the characteristic of the two FOMs, namely FOM1$= k^2 Q_1 Q_2$ and FOM2$= \frac{1}{4r_1}$, we compare the efficiency and power level plots by changing only the receiver to a larger one. The desired power level and input voltage remain the same. The new parameters of the receiver are shown in Table 5.2. The new receiver has more turns, larger outer diameter and higher quality factor. The coupling factor is also higher, $k = 0.0716$. With this system FOM1 is higher due to higher k and Q_2 while FOM2 remain the same as the transmitter is not changed. As shown in the plot of Fig. 5.7, maximum power is not changed but with higher maximum efficiency, every power level is improved. The efficiency at the desired normalized power level 0.09 is now 92%, for i.e. to transfer 1296 W with 120 V input voltage.

Table 5.2: New parameters of the receiver.

Transmitter		Receiver	
n_1	40	n_2	57
L_1	337 μH	L_2	781 μH
r_1	0.56 Ω	r_2	0.97 Ω
D_in	10 cm	D_in	10 cm
D_out	34 cm	D_out	44 cm
Q_1	326	Q_2	417

If the transmitter is changed instead of the receiver, both FOM1 and FOM2 are changed. FOM2 is lower due to higher r_1 of transmitter. Although maximum efficiency is higher, we could not achieve improvement at the desired power level 1296 W as shown in plot of Fig. 5.8.
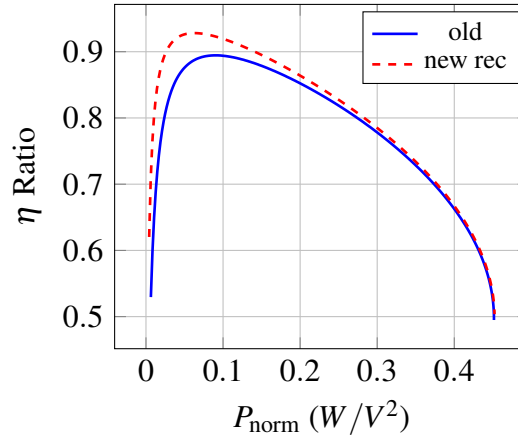
Figure 5.7: Efficiency with larger receiver.

Table 5.3: New parameters of the transmitter.

Transmitter		Receiver	
n_1	57	n_2	40
L_1	781 μH	L_2	337 μH
r_1	0.97 Ω	r_2	0.56 Ω
D_{in}	10 cm	D_{in}	10 cm
D_{out}	44 cm	D_{out}	34 cm
Q_1	430	Q_2	326

5.1.3 Proposed Design Method

As demonstrated from the example in previous section, receiver design only affects FOM1 but not FOM2. Therefore we can design the receiver with highest quality factor possible. For example, the space constraint at the vehicle only allows 44 cm diameter circular coils, the number of turns is varied to find the highest Q_2. In this case, inner diameter and internal resistance are also changed accordingly. The resulted Q_2 vs number of turns is shown in Fig. 5.9.

Next we choose the transmitter by first setting the internal resistance or the cable length to a reference value. With FOM2=$\frac{1}{4r_1}$ fixed, we will choose the transmitter that can provide maximum FOM1=$k^2 Q_1 Q_2$. Quality factor of the receiver, Q_2 at this point is designed. Substituting (5.12) into (5.11), we obtain $k^2 Q_1 = \frac{\omega_0 L_m^2}{L_2}$, therefore a transmitter is designed
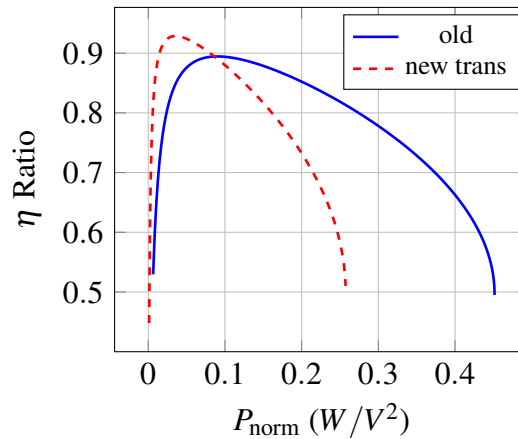
Figure 5.8: Efficiency with larger transmitter.
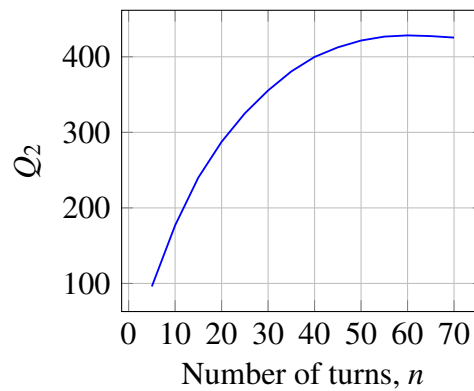
Figure 5.9: Q_2 vs. number of turns of receiver with 44 cm outer diameter.

to maximize L_m. As shown in Fig. 5.10. An optimum number of turns for transmitter can be designed to maximize FOM1 with the designed receiver and chosen r_1. We then repeat the transmitter design procedure to check whether other r_1 could produce a plot with higher efficiency at the desired power level. We begin sweeping values of r_1 by increasing r_1 from the reference value. We can stop increasing r_1 by checking whether the new plot intersects the reference plot at the desired power level or lower power level. As shown in Fig. 5.11, $r_1 = 0.6\,\Omega$ is the starting reference and the desired power level is $0.09\ W/V^2$. Both $r_1 = 0.7\,\Omega$, $r_1 = 0.8\,\Omega$ plots intersect the reference plot at power level lower than $0.09\ W/V^2$ and are unable to improve efficiency at the desired power level. We then begin sweeping at decreasing r_1 from the reference. When the maximum efficiency of the new
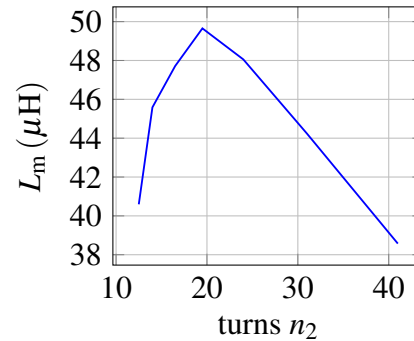
Figure 5.10: Mutual inductance plot vs. number of turns of transmitter coupled with designed receiver.
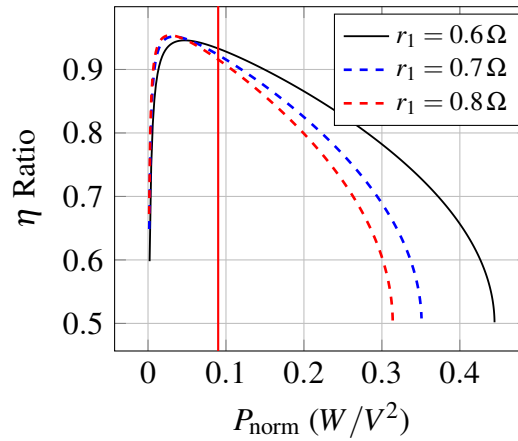
Figure 5.11: Efficiency vs. power level plots for increasing r_1.

plots is lower than the efficiency of the reference plot at the desired power level, we can stop searching the lower r_1 region. The plot with highest efficiency at the desired power level is then chosen. If there are more than one plot with the same/similar efficiency, choose the plot with lowest r_1. As shown in Fig. 5.12, the maximum efficiency of this plot is less than the reference at desired power level when $r_1 = 0.2\,\Omega$. On the other hand, $r_1 = 0.4\,\Omega$ plot has around the same efficiency as $r_1 = 0.6\,\Omega$ reference plot. Therefore we choose this as the final transmitter design as the efficiency across different power range is flatter. We then check whether the desired point is at the left side of the maximum efficiency, if yes, discard the plot and search for next plot with second highest efficiency. The left region is not desirable due to steep changes in efficiency when there is small change in load. The
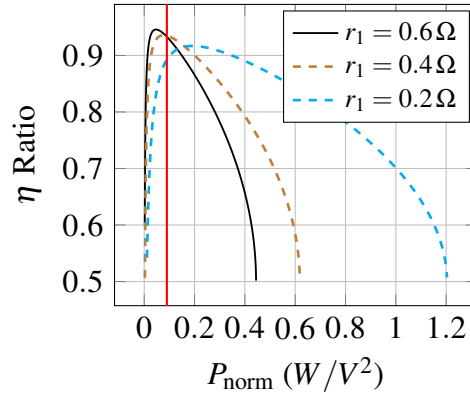
Figure 5.12: Efficiency vs power level plots for decreasing r_1.

design flow chart is shown in Fig. 5.13. With small modification to the design flow, we can optimize efficiency for power level range shown in Fig. 5.14 in red font. In order to perform range modification, we optimized the efficiency at highest desired power level and check whether the lowest desired power level is at the left side of the curve.

5.2 AC Resistance Calculations

The winding losses of the coils are frequency dependent. Skin effect and proximity effect between strands and between bundles alter the current density distribution and increases the resistance of the coils compared to DC losses. Litz wire which consists of many individual insulated strands, up to couple of thousands of strands in a bundle is used to reduce the effects and maintain low winding AC resistance at higher operating frequencies. The coils in above discussion are wounded using Litz wire consists of 301 strands of individual cooper wire, divided into seven bunches that are twisted together. The diameter of the conductor is 1 mm and the diameter of the individual strand is 0.1 mm. Each spiral turn is buried into a 2 mm wide opening and spacing between each turn is 1 mm. The resistance calculation method is using Dowell's equation [91]. The model takes into account of both the proximity effect and skin effects. A factor obtained from real measurements is added to the AC resistance equation as the equation is not accurate for spiral coils. Although the
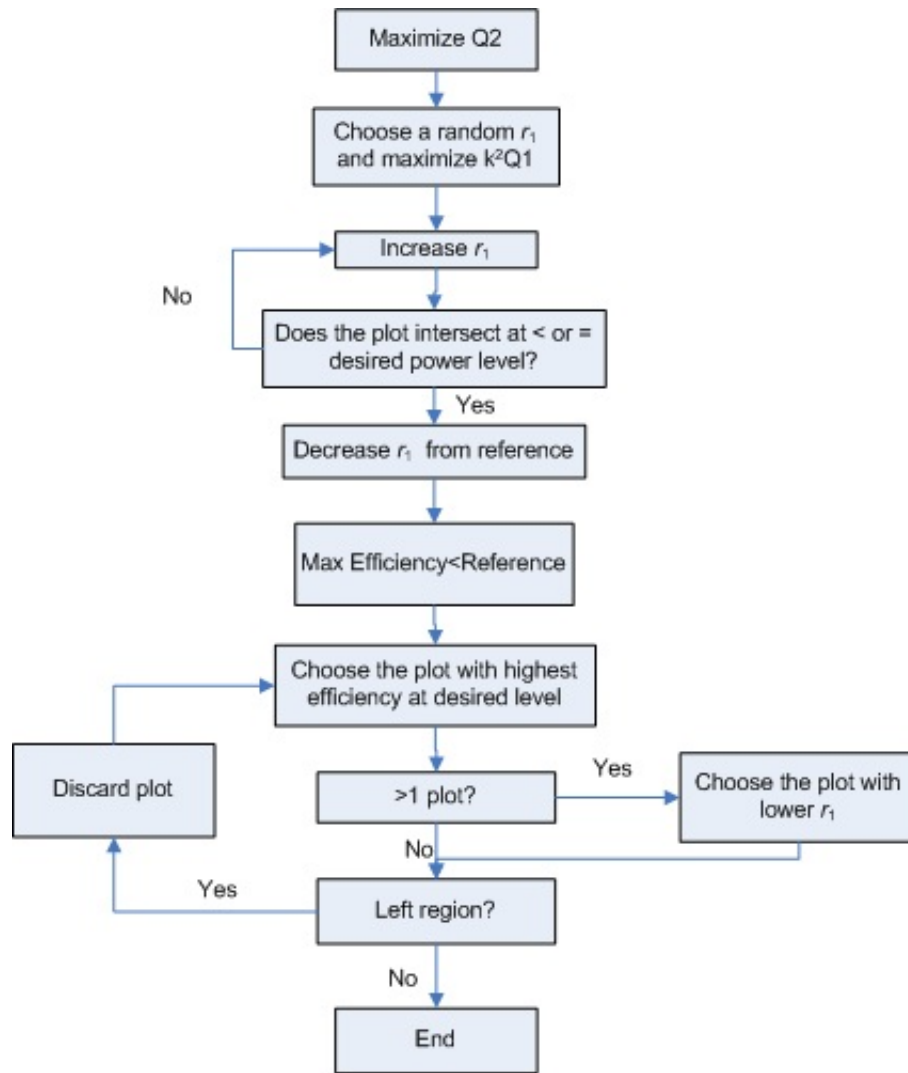
Figure 5.13: Design flow for maximum achievable efficiency at desired power level.
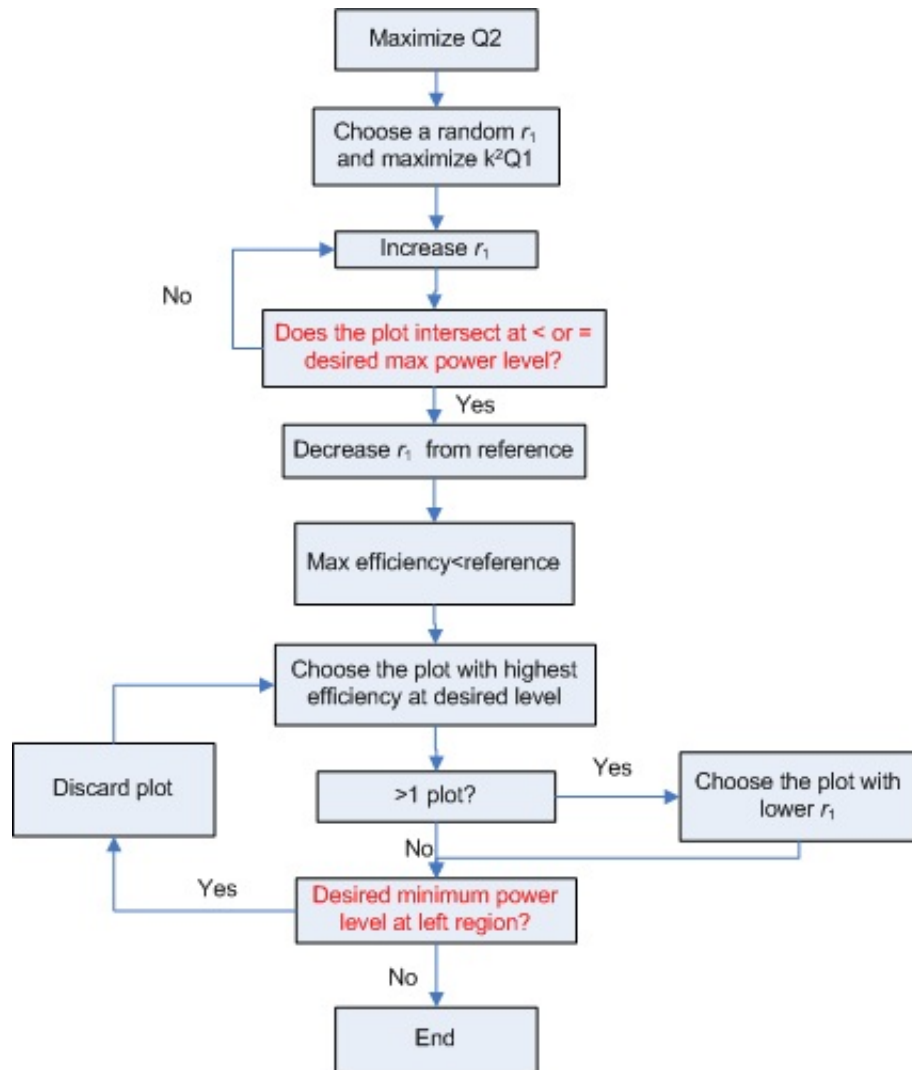
Figure 5.14: Design flow for maximum achievable efficiency at the desired power level range.

equation does not accurately describe the proximity effects in between turns of the spiral coil, the estimation is sufficient to be used in the proposed coil design method.

The DC resistance of a Litz wire winding is

$$r_{dc} = \frac{4\rho l}{k\pi d_{str}^2} \tag{5.14}$$

where k is the number of strands, ρ is the conductor resistivity, d_{str} is the diameter of a single strand, l is the total length of the cable. For spiral coil the total length is:

$$l = (\frac{D_{out} - D_{in}}{2} + D_{in}) \times n \times \pi \tag{5.15}$$

The resistivity of copper is

$$\rho = 1.68 \times 10^{-8}\,\Omega/m \tag{5.16}$$

where n is number of turns. The modified Dowell's equation for AC resistance ratio in Litz wire is:

$$F_R = 1 + \frac{\eta_w^2(5N_{ll}^2 - 1)}{45}(\frac{\pi}{4})^3(\frac{d_{str}}{\delta})^4 \tag{5.17}$$

where η_w is the porosity factor, N_{ll} is the number of layers of strands, and δ is the skin depth. The distance between strands is described by porosity factor. In this calculation the Litz wire is assumed to be tightly pack and the porosity factor, η_w is equal to 1. It also assumed that individual strands are parallel to the axis of the bundle, and each bundle has a square shape, therefore the number of layers is given by:

$$N_{ll} = \sqrt{k} \tag{5.18}$$

where k is 301 in this study. Skin effect, δ is frequency dependent and is equal to:

$$\delta = \sqrt{\frac{2\rho}{\mu_0 \omega_0}} \tag{5.19}$$

where μ_0 is the free-space permeability. The AC resistance of the coil is then:

$$r = r_{dc} \times F_R \tag{5.20}$$

Table 5.4: Dimension of the measured coils.

Coil	Inner Diameter, D_{in}	Inner Diameter, D_{out}	Number of turns, n
1	22.5 cm	43.5 cm	35
2	10 cm	34 cm	40
3	10 cm	44 cm	57
4	43.5 cm	58 cm	25

In this study, the Litz wire used is the same. Only the dimension of the coils is changed. Furthermore, the proximity effect between turns in the spiral coil is not considered in the equation. Therefore, the frequency dependent AC resistance ratio, F_{R} in all coils is equal to

$$F_{\mathrm{R}} = 1 + a\omega_0^2 \tag{5.21}$$

where a is a constant given by:

$$a = \frac{\eta_{\mathrm{w}}^2(5N_{ll}^2 - 1)}{45}(\frac{\pi}{4})^3 d_{\mathrm{str}}^4 \frac{\mu_0^2}{4\rho^2} \tag{5.22}$$

5.2.1   Measurement Results

The AC resistance of four different spiral coils is measured using Agilent Vector Network Analyzer (VNA) from 1 kHz to 150 kHz. The dimension of the coils is given in Table 5.4.

Fig. 5.15 shows the plot of coil resistance vs. frequency for the four different spiral coils. The DC to low frequency resistance matches with calculation from (5.14) and is depending on the cable length of the winding as other parameters of the cable are fixed. As the frequency increases, the measured resistance is less accurate. Fig. 5.2.1 shows the plot of F_{R} for the four coils. The fitted line is obtained by using $a = 5.0884\mathrm{E} - 012$ and the calculated a is 2.2649E-012.
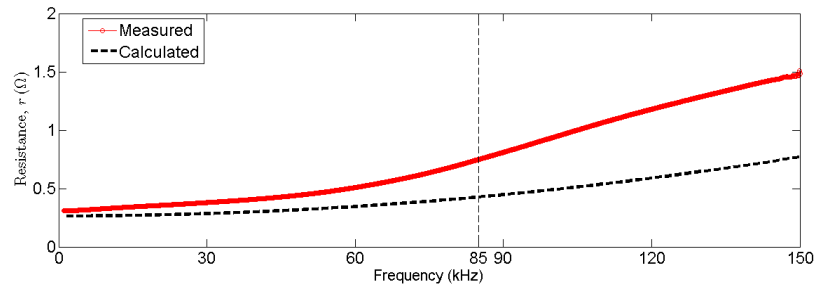
(a)
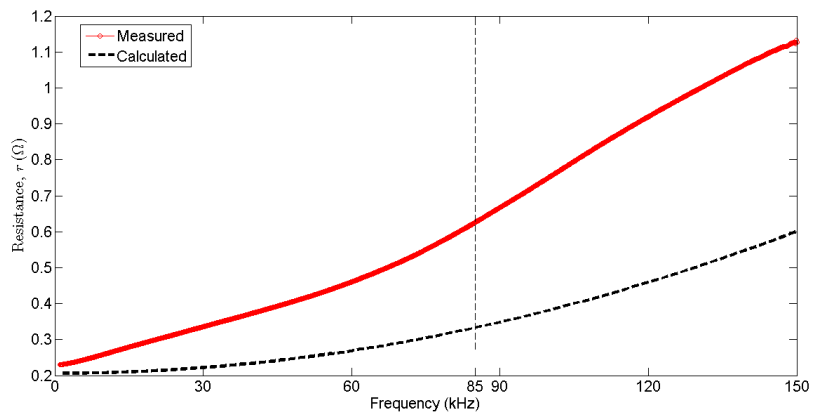
(b)
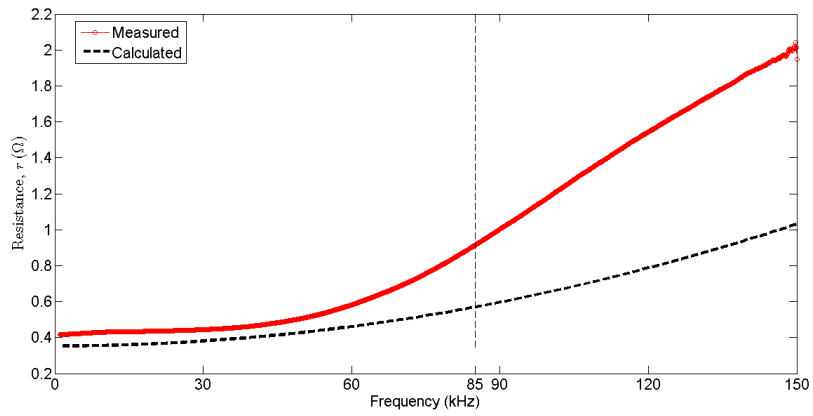
(c)
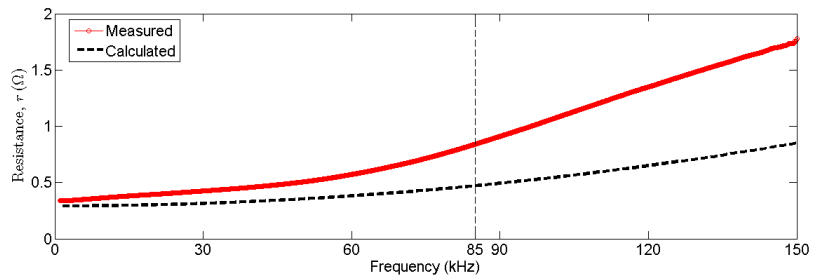
(d)

Figure 5.15: Coil resistance vs. frequency for a) coil 1, b) coil 2, c) coil 3, d) coil 4.
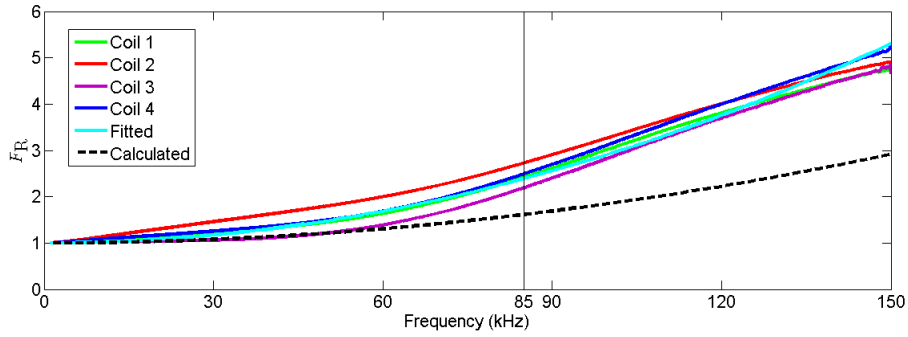
Figure 5.16: F_R ratio of the coils vs frequency.
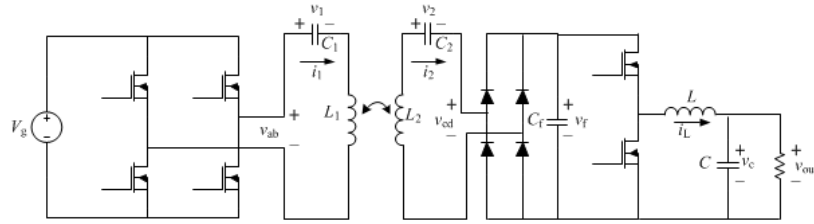
Figure 5.17: Wireless power transfer circuit.

5.3 Generalized State Space Averaging

The equivalent circuits of wireless power transfer for dynamic charging is shown in Fig. 5.17. The inverter converts DC supply power to ac power at resonant frequency and activates the transmitters. The coupled receiver then converts the ac power back to dc via the full bridge rectifier and a dc/dc converter performs charging control where constant current charging is desired [90]. The average equations in one sampling frequency for all the inductors and capacitors are firstly listed:

$$L_1 \frac{di_1}{dt} = v_{ab} - v_1 - l_m \frac{di_2}{dt} \tag{5.23}$$

$$L_2 \frac{di_2}{dt} = -v_2 - v_{cd} - l_m \frac{di_1}{dt} \tag{5.24}$$

$$C_1 \frac{dv_1}{dt} = i_1 \tag{5.25}$$

$$C_2 \frac{dv_2}{dt} = i_2 \tag{5.26}$$

$$C_f \frac{dv_f}{dt} = |i_2| - di_L \tag{5.27}$$

$$L \frac{di_L}{dt} = dv_f - v_C \tag{5.28}$$

$$C \frac{dV_C}{dt} = i_L - \frac{v_C}{R_L} \tag{5.29}$$

(5.23)-(5.26) are the equations for the ac portion of the wireless power transfer and is rearranged to obtain:

$$\frac{di_1}{dt} = \frac{v_{ab}}{L_{eq2}} - \frac{v_1}{L_{eq2}} + \frac{v_2}{L_{eqm}} + \frac{v_{cd}}{L_{eqm}} \tag{5.30}$$

$$\frac{di_2}{dt} = -\frac{v_2}{L_{eq1}} - \frac{v_{cd}}{L_{eq1}} - \frac{v_{ab}}{L_{eqm}} + \frac{v_1}{L_{eqm}} \tag{5.31}$$

$$C_1 \frac{dv_1}{dt} = i_1 \tag{5.32}$$

$$C_2 \frac{dv_2}{dt} = i_2 \tag{5.33}$$

$$L_{eq1} = \frac{L_1 L_2 - l_m^2}{L_1} \tag{5.34}$$

$$L_{eq2} = \frac{L_1 L_2 - l_m^2}{L_2} \tag{5.35}$$

$$L_{eq1} = \frac{L_1 L_2 - l_m^2}{l_m} \tag{5.36}$$

Assuming high quality factor resonant circuit, the excitation input from the inverter is :

$$v_{ab} = \frac{4v_g}{\pi} \sin(\omega_s t) \tag{5.37}$$

Other waveforms are also sinusoidal with phase shift compared to v_{ab} and can be separated into d-q components.

$$x(t) = x_d(t) + jx_q(t) \tag{5.38}$$

Furthermore

$$v_{cd} = \text{sgn}(i_2)V_f = \frac{4}{\pi}\frac{i_{2d}v_f}{i_{2p}} + j\frac{4}{\pi}\frac{i_{2q}v_f}{i_{2p}} \tag{5.39}$$

$$|i_2| = \frac{2}{\pi}i_{2p} \tag{5.40}$$

$$i_{2p} = \sqrt{i_{2d}^2 + i_{2q}^2} \tag{5.41}$$

Separating the signals into their respective d-q components in (5.30) to (5.33), and rearranging:

$$\frac{di_{1d}}{dt} = \frac{v_{ab}}{L_{eq2}} - \frac{v_{1d}}{L_{eq2}} + \frac{v_{2d}}{L_{eqm}} + \frac{4i_{2d}v_f}{\pi i_{2p}L_{eqm}} + \omega_0 i_{1q} \tag{5.42}$$

$$\frac{di_{1q}}{dt} = -\frac{v_{1q}}{L_{eq2}} + \frac{v_{2q}}{L_{eqm}} + \frac{4i_{2q}v_f}{\pi i_{2p}L_{eqm}} - \omega_0 i_{1d} \tag{5.43}$$

$$\frac{di_{2d}}{dt} = -\frac{v_{ab}}{L_{eqm}} - \frac{v_{2d}}{L_{eq1}} + \frac{v_{1d}}{L_{eqm}} - \frac{4i_{2d}v_f}{\pi i_{2p}L_{eq1}} + \omega_0 i_{2q} \tag{5.44}$$

$$\frac{di_{2q}}{dt} = -\frac{v_{2q}}{L_{eq1}} + \frac{v_{1q}}{L_{eqm}} - \frac{4i_{2q}v_f}{\pi i_{2p}L_{eq1}} - \omega_0 i_{2d} \tag{5.45}$$

$$\frac{dv_{1d}}{dt} = \frac{i_{1d}}{C_1} + \omega_0 v_{1q} \tag{5.46}$$

$$\frac{dv_{1q}}{dt} = \frac{i_{1q}}{C_1} - \omega_0 v_{1d} \tag{5.47}$$

$$\frac{dv_{2d}}{dt} = \frac{i_{2d}}{C_2} + \omega_0 v_{2q} \tag{5.48}$$

$$\frac{dv_{2q}}{dt} = \frac{i_{2q}}{C_2} - \omega_0 v_{2d} \tag{5.49}$$

(5.42) to (5.49) are average equations for one sampling frequency. Values of passive elements are assumed to be constant and large signal state variables contain steady state values and small signal variations:

$$A_{st} = \begin{bmatrix} 1 & -\frac{L_{eq2}}{L_{eqm}} & 0 & -\frac{L_{eq2}R_e}{L_{eqm}} & 0 & 0 & -\omega_s L_{eq2} & 0 \\ 1 & -\frac{L_{eqm}}{L_{eq1}} & 0 & -\frac{L_{eqm}R_e}{L_{eq1}} & 0 & 0 & 0 & \omega_s L_{eqm} \\ 0 & 0 & 1 & 0 & \omega_s C_1 & 0 & 0 & 0 \\ 0 & 0 & 0 & 1 & 0 & \omega_s C_2 & 0 & 0 \\ 0 & 0 & -\omega_s L_{eq2} & 0 & -1 & \frac{L_{eq2}}{L_{eqm}} & 0 & \frac{L_{eq2}R_e}{L_{eqm}} \\ 0 & 0 & 0 & -\omega_s L_{eqm} & 1 & -\frac{L_{eqm}}{L_{eq1}} & 0 & -\frac{L_{eqm}R_e}{L_{eq1}} \\ -\omega_s C_1 & 0 & 0 & 0 & 0 & 0 & 1 & 0 \\ 0 & -\omega_s C_2 & 0 & 0 & 0 & 0 & 0 & 1 \end{bmatrix} \tag{5.60}$$

$$i_{1d} = I_{1d} + \hat{i}_{1d} \tag{5.50}$$

$$i_{1q} = I_{1q} + \hat{i}_{1q} \tag{5.51}$$

$$i_{2d} = I_{2d} + \hat{i}_{2d} \tag{5.52}$$

$$v_{1d} = V_{1d} + \hat{v}_{1d} \tag{5.53}$$

$$v_{1q} = V_{1q} + \hat{v}_{1q} \tag{5.54}$$

$$v_{2d} = V_{2d} + \hat{v}_{2d} \tag{5.55}$$

$$v_{2q} = V_{2q} + \hat{v}_{2q} \tag{5.56}$$

Similarly for the state variables in DC portion:

$$v_f = V_f + \hat{v}_f \tag{5.57}$$

$$i_L = I_L + \hat{i}_L \tag{5.58}$$

$$v_c = V_c + \hat{v}_c \tag{5.59}$$

Substituting (5.42) to (5.49) into (5.50) to (5.56) and let the steady state equations equal to zero as differentiating constant we obtain zero, we can solve for all steady states variables.

$$B_{st} = \begin{bmatrix} V_{ab} & V_{ab} & 0 & 0 & 0 & 0 & 0 & 0 \end{bmatrix}^T \tag{5.61}$$

$$X_{st} = \begin{bmatrix} V_{1d} & V_{2d} & I_{1d} & I_{2d} & V_{1q} & V_{2q} & I_{1q} & I_{2q} \end{bmatrix}^T \tag{5.62}$$

$$R_\text{e} = \frac{8}{\pi^2} \frac{R_\text{L}}{D^2} \tag{5.63}$$

$$X_\text{st} = A_\text{st}{}^{-1} B_\text{st} \tag{5.64}$$

And from (5.27) to (5.29) and (5.57) to (5.59)

$$I_\text{L} = \frac{2I_{2\text{p}}}{\pi D} \tag{5.65}$$

$$V_\text{C} = I_\text{L} R_\text{L} \tag{5.66}$$

$$V_\text{f} = \frac{V_\text{C}}{D} \tag{5.67}$$

The linearized small signal equations are given by

$$\frac{d}{dt}\hat{x} = A\hat{x} + B\hat{u} \tag{5.68}$$

$$\hat{y} = C\hat{x} + E\hat{u} \tag{5.69}$$

where

$$A = \begin{bmatrix} \frac{df_1}{dx_1} & \cdots & \frac{df_1}{dx_n} \\ \vdots & \ddots & \vdots \\ \frac{df_m}{dx_1} & \cdots & \frac{df_m}{dx_n} \end{bmatrix} \tag{5.70}$$

and

$$B = \begin{bmatrix} \frac{df_1}{du_1} & \frac{df_1}{du_2} & \frac{df_1}{du_3} \\ \vdots & \vdots & \vdots \\ \frac{df_m}{du_1} & \frac{df_m}{du_2} & \frac{df_m}{du_3} \end{bmatrix} \tag{5.71}$$

The state variables for the wireless power transfer system are:

$$\hat{x} = \begin{bmatrix} \hat{i_{1\text{d}}} & \hat{i_{1\text{q}}} & \hat{i_{2\text{d}}} & \hat{i_{2\text{q}}} & \hat{v_{1\text{d}}} & \hat{v_{1\text{q}}} & \hat{v_{2\text{d}}} & \hat{v_{2\text{q}}} & \hat{v_f} & \hat{i_L} & \hat{v_\text{c}} \end{bmatrix}^T \tag{5.72}$$

and inputs to the system are

$$\hat{u} = \begin{bmatrix} \hat{l_\text{m}} & \hat{v_\text{ab}} & \hat{d} \end{bmatrix}^T \tag{5.73}$$

$\hat{d}$ is the control input whereas $\hat{l}_m$ and $\hat{v}_{ab}$ are the disturbance inputs.

Therefore from (5.42) to (5.49) and (5.27) to (5.29), the small signal state space for the wireless power transfer including secondary dc/dc converter control can be derived. The constants in (5.74) are given as:

$$k_1 = \frac{4V_f}{\pi I_{2p}}\left(\frac{1}{I_{2p}} + \frac{I_{2s}^2}{I_{2p}^3}\right)$$

$$k_2 = \frac{4V_f I_{2s} I_{2p}}{I_{2p}^3}$$

$$k_3 = \frac{4I_{2s}}{\pi I_{2p}}$$

$$k_4 = \frac{4I_{2c}}{\pi I_{2p}}$$

$$k_5 = \frac{2I_{2s}}{\pi I_{2p} C_f}$$

$$k_6 = \frac{2I_{2c}}{\pi I_{2p} C_f}$$

$$k_7 = V_e d_{leq2} - V_{1s} d_{leq2} + V_{2s} d_{leqm} + \frac{4I_{2s} V_f d_{leqm}}{\pi I_{2p}}$$

$$k_8 = -V_{1c} d_{leq2} + V_{2c} d_{leqm} + \frac{4I_{2c} V_f d_{leqm}}{\pi I_{2p}}$$

$$k_9 = -V_e d_{leqm} + V_{1s} d_{leqm} - V_{2s} d_{leq1} - \frac{4I_{2s} V_f d_{leq1}}{\pi I_{2p}}$$

$$k_{10} = V_{1c} d_{leqm} - V_{2c} d_{leq1} - \frac{4I_{2c} V_f d_{leq1}}{\pi I_{2p}}$$

$$A = \begin{bmatrix}
0 & \omega_s & \frac{k_1}{L_{eqm}} & -\frac{k_2}{L_{eqm}} & -\frac{1}{L_{eq2}} & 0 & \frac{1}{L_{eqm}} & 0 & \frac{k_3}{L_{eqm}} & 0 & 0 \\
-\omega_s & 0 & -\frac{k_2}{L_{eqm}} & \frac{k_1}{L_{eqm}} & 0 & \frac{-1}{L_{eq2}} & 0 & \frac{1}{L_{eqm}} & \frac{k_4}{L_{eqm}} & 0 & 0 \\
0 & 0 & \frac{-k_1}{L_{eqm}} & \omega_s + \frac{k_2}{L_{eq1}} & \frac{1}{L_{eqm}} & 0 & -\frac{1}{L_{eq1}} & 0 & -\frac{k_3}{L_{eq1}} & 0 & 0 \\
0 & 0 & -\omega_s + \frac{k_2}{L_{eq1}} & -\frac{k_1}{L_{eq1}} & 0 & \frac{1}{L_{eqm}} & 0 & -\frac{1}{L_{eq1}} & -\frac{k_4}{L_{eq1}} & 0 & 0 \\
\frac{1}{C_1} & 0 & 0 & 0 & 0 & \omega_s & 0 & 0 & 0 & 0 & 0 \\
0 & \frac{1}{C_1} & 0 & 0 & -\omega_s & 0 & 0 & 0 & 0 & 0 & 0 \\
0 & 0 & \frac{1}{C_2} & 0 & 0 & 0 & 0 & \omega_s & 0 & 0 & 0 \\
0 & 0 & 0 & \frac{1}{C_2} & 0 & 0 & -\omega_s & 0 & 0 & 0 & 0 \\
0 & 0 & k_5 & k_6 & 0 & 0 & 0 & 0 & 0 & -\frac{D}{C_f} & 0 \\
0 & 0 & 0 & 0 & 0 & 0 & 0 & 0 & \frac{D}{L} & 0 & -\frac{1}{L} \\
0 & 0 & 0 & 0 & 0 & 0 & 0 & 0 & 0 & \frac{1}{C} & -\frac{1}{RC}
\end{bmatrix} \tag{5.74}$$

$$B = \begin{bmatrix}
k_7 & \frac{1}{L_{eq2}} & 0 \\
k_8 & 0 & 0 \\
k_9 & -\frac{1}{L_{eqm}} & 0 \\
k_{10} & 0 & 0 \\
0 & 0 & 0 \\
0 & 0 & 0 \\
0 & 0 & 0 \\
0 & 0 & 0 \\
0 & 0 & -\frac{I_L}{C_f} \\
0 & 0 & \frac{V_{cf}}{L} \\
0 & 0 & 0
\end{bmatrix} \tag{5.75}$$

$$C = \begin{bmatrix} 0 & 0 & 0 & 0 & 0 & 0 & 0 & 0 & 0 & 0 & 1 \end{bmatrix}^T \tag{5.76}$$

$$E = \begin{bmatrix} 0 & 0 & 0 \end{bmatrix}^T \tag{5.77}$$

5.4 Experiment Verifications

Fig. 5.18 shows the photo of the experiment setup and the parameters in equivalent circuit of Fig. 5.17 are listed in Table 5.5.
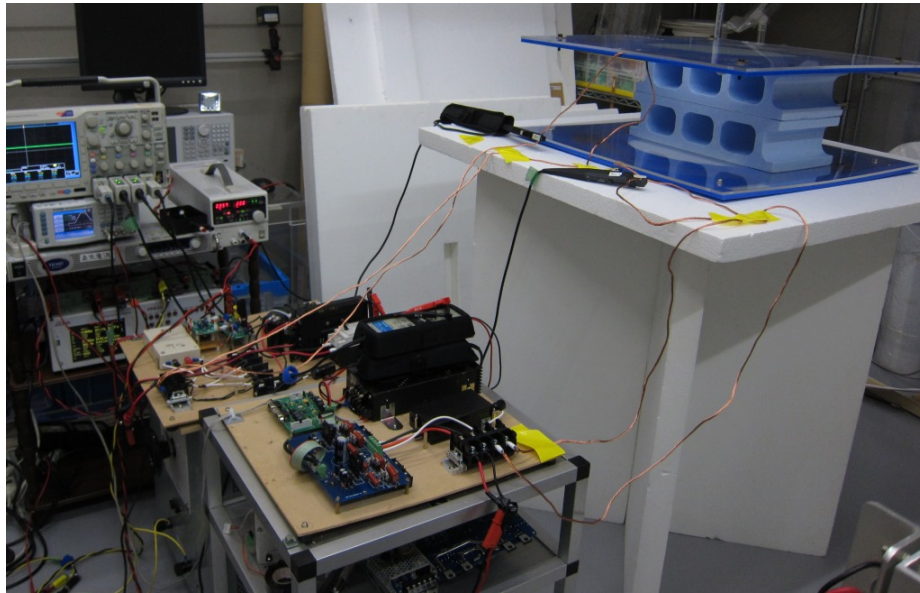
Figure 5.18: Experiment setup for model verification.

5.4.1 Steady State Variables

Fig. 5.19 shows the calculated output voltage from the derived model and experiment measurement plots vs mutual inductance. The results show good agreement between experiments and calculations. The small difference in the plots is due to the internal resistance of coils which are not considered in the model. Fig. 5.20 shows that output voltage vs dc/dc converter duty cycle plots also have good agreement between experiments and calculations.

5.4.2 Dynamic Response

Fig. 5.21 shows that when the primary input voltage is stepped, the output voltage rise time is around 4 s for current experiment setup. The experimental step response in Fig. 5.22 is similar to the model step response.

Both the model mutual inductance step response shown in Fig. 5.23 and experiment mutual inductance step response shown in Fig. 5.24 have around 3 s rise time confirming the derived model.

Table 5.5: Experiment parameters.

Parameters	Values
V_g	5 V
L_1	550 μH
C_1	6.37 nF
L_2	550 μH
C_2	6.37 nF
R_L	48 Ω
C_f	4700 μF
L_m	98 μH
L	1.72 μH
C	200 μF
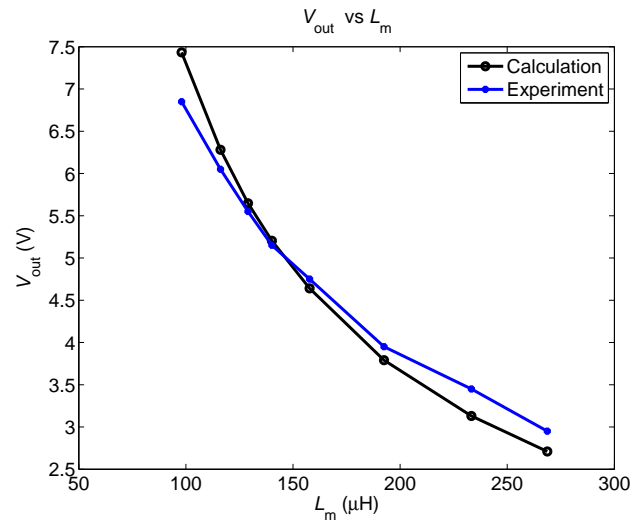
Figure 5.19: Output voltage, V_{out} vs mutual inductance, L_m.
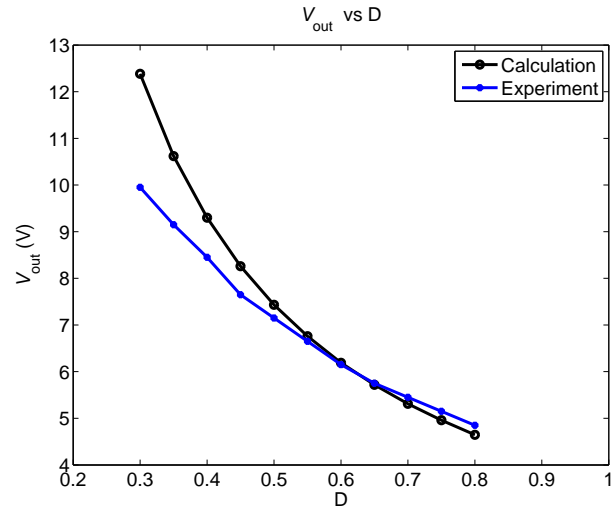
Figure 5.20: Output voltage, V_{out} vs duty cycle, D.
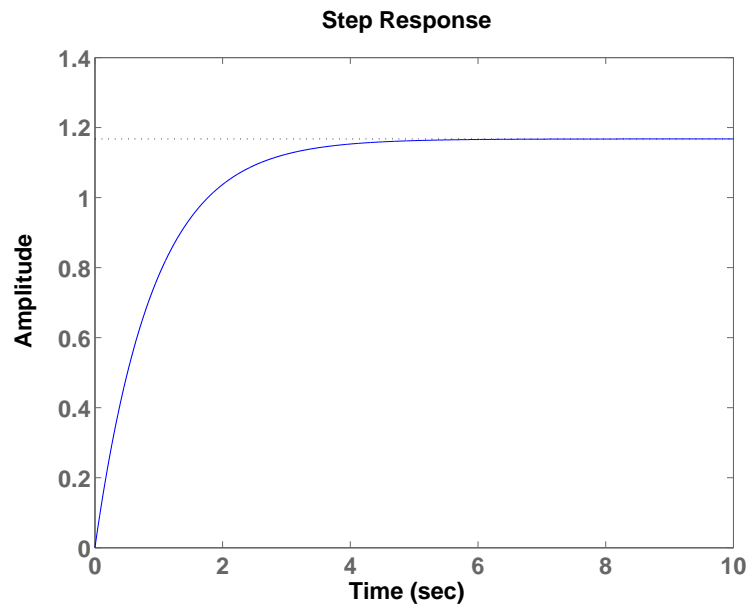
Figure 5.21: Model input voltage step response.
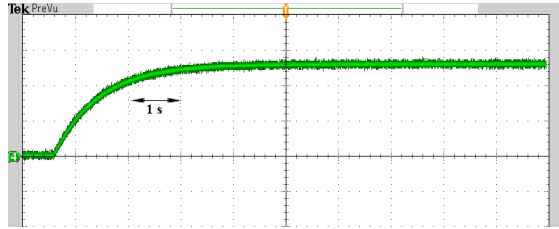
Figure 5.22: Experiment input voltage step response.
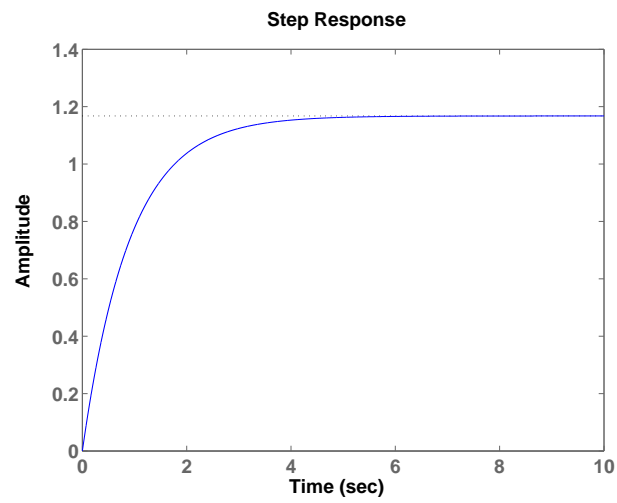
Figure 5.23: Model mutual inductance step response.
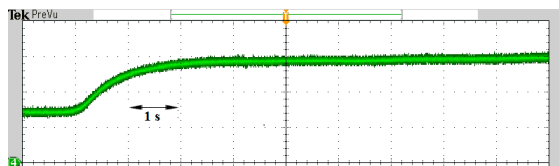
Figure 5.24: Experiment mutual inductance step response
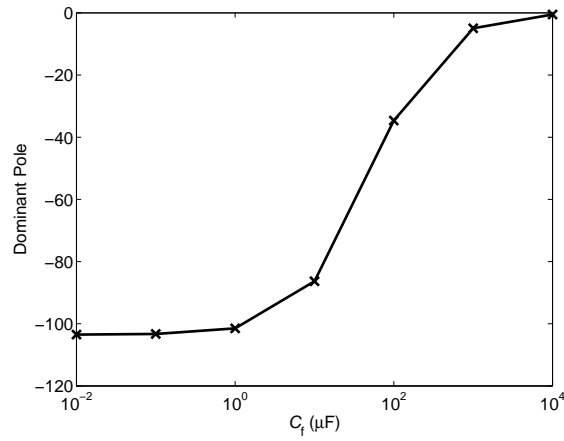
Figure 5.25: Dominant pole location of input voltage to output voltage transfer function for different C_f.
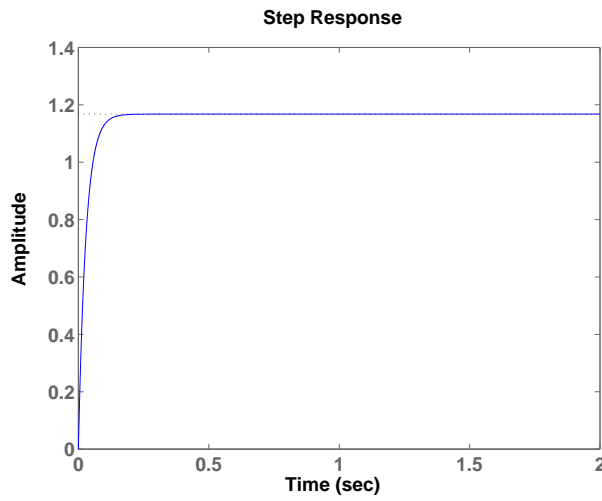
Figure 5.26: Model input voltage step response with small C_f.
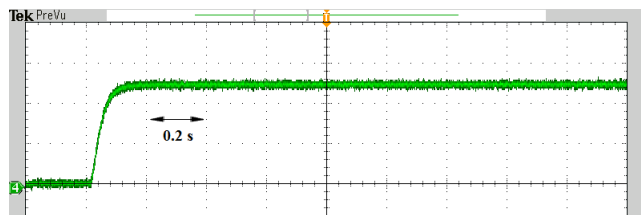
Figure 5.27: Experiment input voltage step response with small C_f.
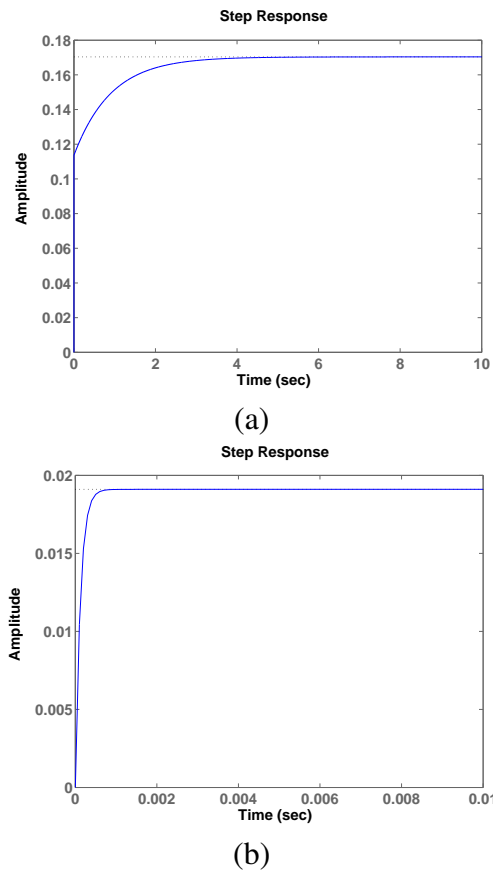
Figure 5.28: Model input voltage step response for: a) primary current, b) secondary current.

One of the reasons for slow rise time is the large filter capacitor used in the experiment setup. Fig. 5.25 shows the dominant pole of input voltage to output voltage transfer function when the capacitance C_f is varied from 0.01 μF to 100000 μF. Large C_f will results in slow response while small C_f will results in large ripple. A new C_f which around 100 μF is chosen where further reduction in C_f will not improve the response time. The dominant pole is affected by the slow pole caused by the capacitor in dc/dc converter Fig. 5.26 shows the model input voltage step response with the rise time improved to less than 0.2 s. Experiment step response is shown in Fig. 5.27.
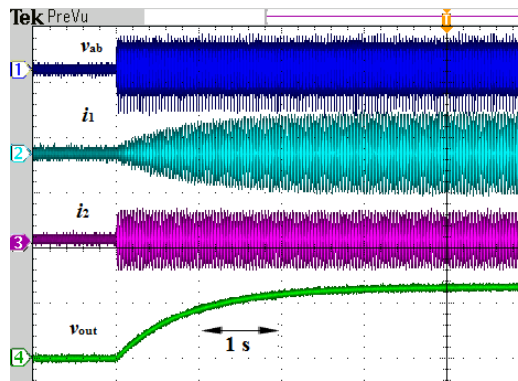
Figure 5.29: Experiment input voltage step response for primary and secondary current.

5.4.3 Generality of Small Signal State Space

The transfer function from inputs to any state variables can be derived easily once the small signal state space is derived. The envelope of the ac waveforms can also be controlled as they are slow varying compared to the switching frequency of either the inverter or dc/dc converter. When the large filter capacitor is used, the primary current, is also rising slowly before steady state is reached. Fig. 5.29 shows the model input voltage step response for primary current, i_1 and secondary current i_2 and experiment step response is shown in Fig. 5.28.

5.5 Compensator Design for Resistor Load

Basic study for vibration suppression due to the LC filter and disturbance rejection using traditional lead-lag compensator has been carried out. The feedback control loop is shown in Fig. 5.30. Compensator G_c is designed to achieve a fast and stable response in the presence of disturbance inputs.
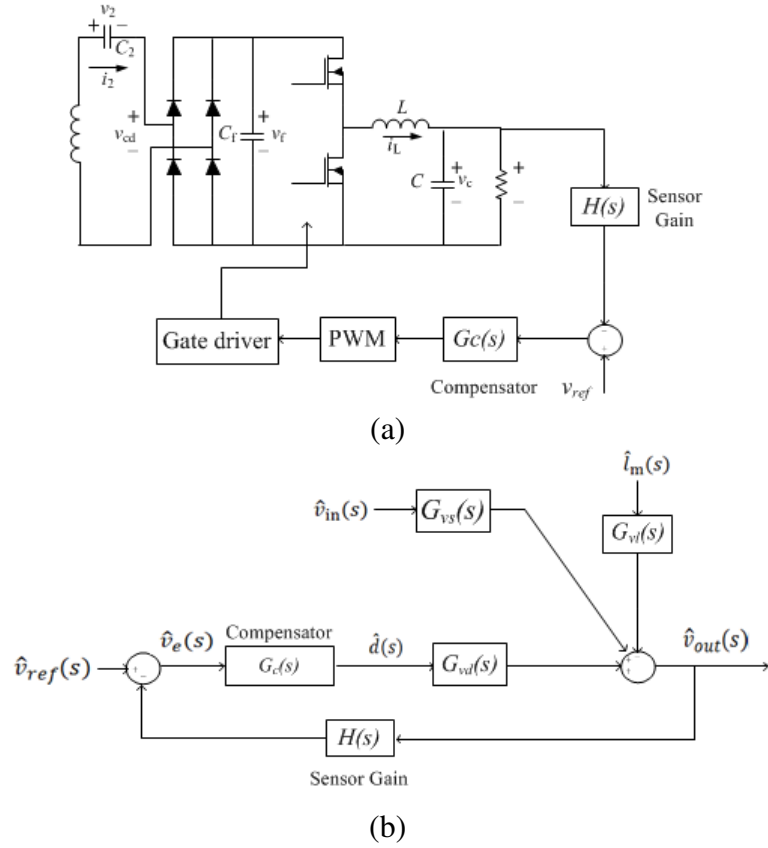
Figure 5.30: Control block diagram: (a) secondary equivalent circuit, (b) block diagram.

The transfer function of the control loop is given as:

$$\hat{v}_{out} = \hat{v}_{ref}\frac{1}{H}\frac{L}{1+L} + \hat{v}_{in}\frac{G_{vs}(s)}{1+L} + \hat{i}_m\frac{G_{vl}(s)}{1+L} \tag{5.78}$$

where

$$L(s) = H(s)G_c(s)G_{vd}(s)/V_M \tag{5.79}$$

G_{vd} are derived from the above small signal state space model. $H(s)$ is the voltage sensor gain. Due to the inductor and filter capacitor in the DC/DC converter, the response of the output from the reference voltage contains ringing. Therefore lead compensator G_{clead} in (5.80) is designed to improve the phase margin and therefore removing the ringing and to achieve a fast response.

$$G_{\text{clead}} = \frac{T_{\text{lead}}s + 1}{\alpha T_{\text{lead}}s + 1} \tag{5.80}$$

The ratio α and T_{lead} are chosen so that the maximum phase lead improvement occurs at 1 kHz which is selected as 10 times lesser than the controller sampling frequency. An optional lag compensator can be added to adjust the gain of the feedback loop, $L(s)$.

$$G_{\text{clag}} = \beta \frac{T_{\text{lag}}s + 1}{\beta T_{\text{lag}}s + 1} \tag{5.81}$$

The final designed compensator:

$$
\begin{aligned}
G_c &= G_{\text{clead}} \times G_{\text{clag}} \tag{5.82} \\
&= (0.124) \frac{\frac{s}{2\pi \times 315} + 1}{\frac{0.1s}{2\pi \times 315} + 1} \times (3.5) \frac{\frac{s}{2\pi \times 200} + 1}{\frac{3.5s}{2\pi \times 200} + 1} \tag{5.83}
\end{aligned}
$$

The bodeplot of the feedback loop is shown in Fig. 58. With lead only the control, the phase margin is improved to 52^0 and the system is stable without ringing. However to achieve 1 kHz crossover frequency, a less than one gain is added to the lead compensator and the steady state error is now large. Small dc gain is unable to reject disturbances in the system. Therefore lag compensator is added at low frequency to achieve higher dc gain. Lower frequency which is 200 Hz is chosen so that the phase margin will not be significantly affected. Fig. 5.32 shows the step response of the closed loop system without feedforward control.

5.6 Feedforward Compensator Design for Battery Load

The equivalent circuit for battery load is given in Fig. 5.33. The parameters are the same as Table 5.5. The battery voltage is 12 V and charging current is 2 A. A feedforward controller is designed for charging current tracking. The plant considering only the DC portion is given in (5.84). A Zero Phase Error Tracking Control (ZPETC) is proposed for charging current control due to the unstable zero in (5.84). The controller block diagram
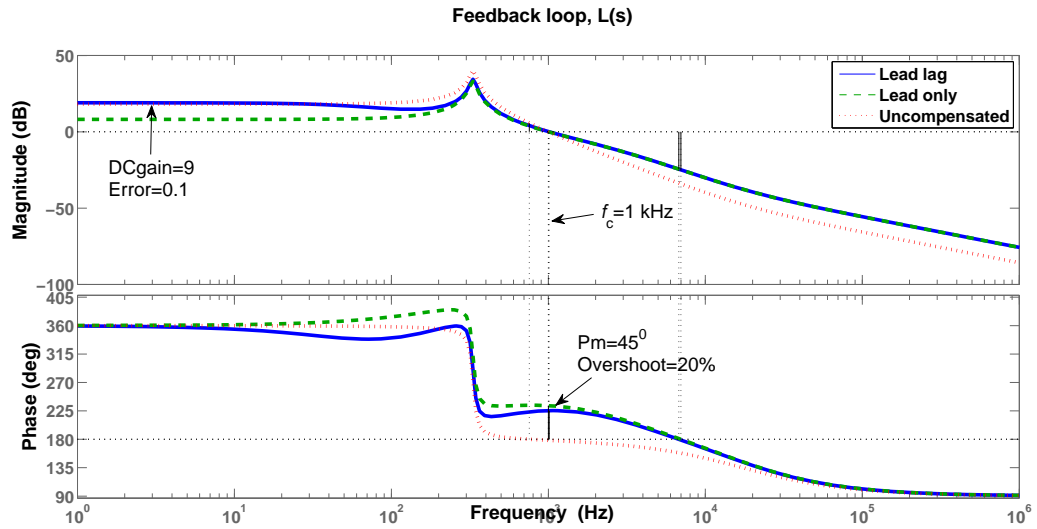
Figure 5.31: Bode plot of the feedback loop transfer function, $L(s)$.
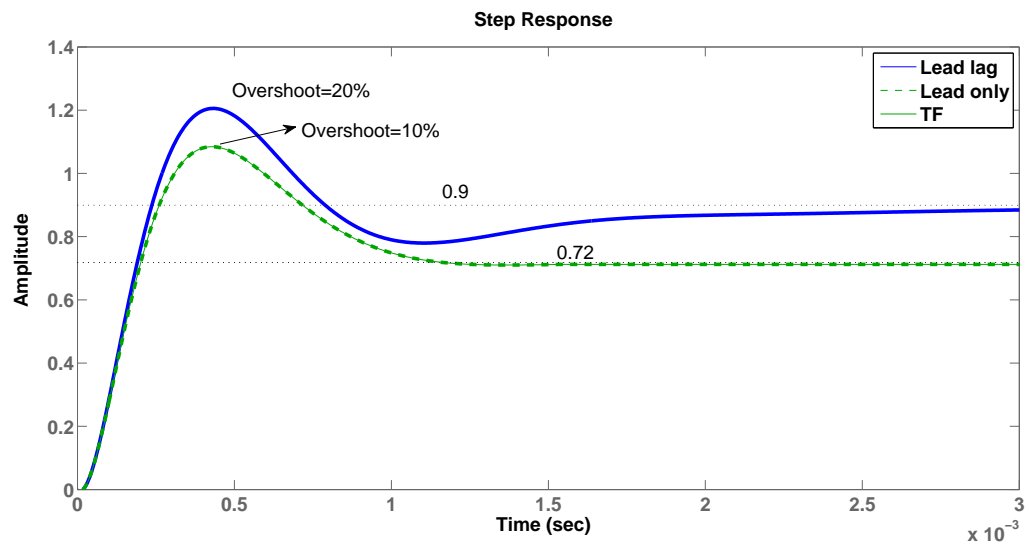
Figure 5.32: Step response of the system with feedback control.
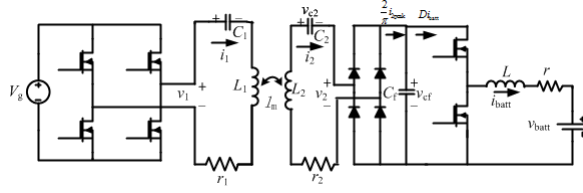
Figure 5.33: Equivalent circuit for battery charging using dc/dc control.
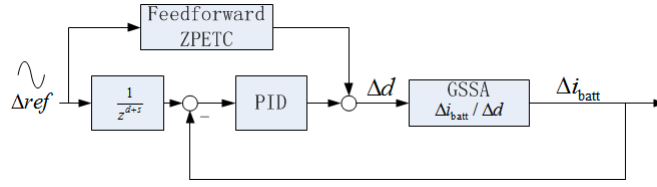
Figure 5.34: Feedforward current control block diagram.

is given in Fig. 5.34. The feedback controller is obtained by pole placement of the fourth root against the plant.

$$\frac{\Delta i_{\text{batt}}}{\Delta d} = \frac{b_1 s + b_0}{s^2 + a_1 s + a_0} \tag{5.84}$$

where $b_1 = \frac{V_{\text{cf}}}{L}$, $b_0 = -\frac{C_{\text{f}} I_{\text{batt}}}{L C_{\text{f}}}$, $a_1 = \frac{r}{L}$ and $a_0 = \frac{D^2}{L C_{\text{f}}}$. The digitized control plant using zero-order hold is represented by [94]:

$$\Delta G(z^{-1}) = \frac{z^{-d} B(z^{-1})}{A(z^{-1})} \tag{5.85}$$

where z^{-d} represents a d-step delay caused by the plant. The feedforward controller:

$$r(k) = \frac{z^d A(z^{-1}) B^-(z)}{B^+(z^{-1}) B^-(1)^2} \tag{5.86}$$

where $B^+(z^{-1})$ is contains the cancelable zeros and $B^-(z^{-1})$ contains the uncancellable zeroes. $B^-(z)$ is obtained by replacing every z^{-1} in $B^-(z^{-1})$ by z

The simulation results are shown in Fig. 5.35. The plot shows that the output is able to track the reference input with the feedforward control.
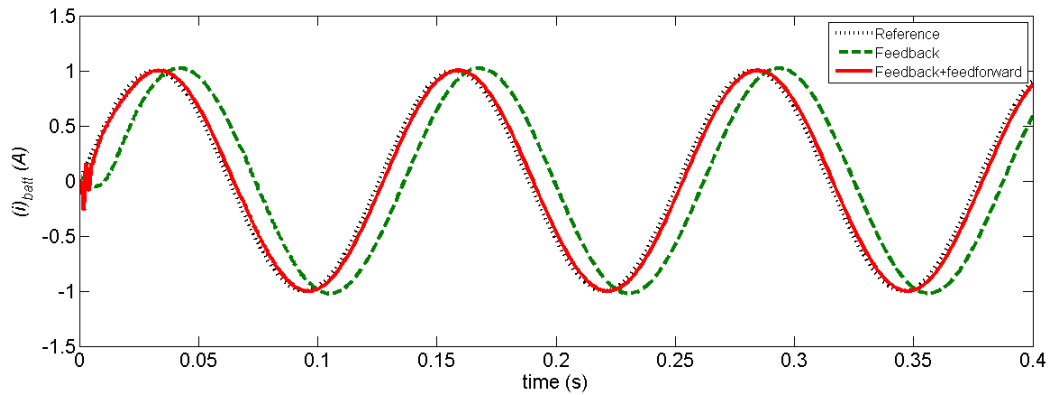
Figure 5.35: Simulation results for feedforward control.

5.7 Chapter Summary

In this chapter, coil design relating to power level and efficiency is discussed. The efficiency depends on both the transmitter and receiver coils but the power level depends only on the transmitter coil. This characteristic of wireless power transfer is exploited to obtain flatter efficiency curve across wider power level. The AC resistance was also calculated using extended Dowell formula but not including the external proximity effect. Fitted data is used to increase the accuracy of AC resistance calculation. Discussion on using general state space averaging method to model the fast varying AC signal of wireless power transfer is also included in this chapter. General state space averaging is a widely used method to model transient of AC signal for example in resonant dc/dc converters and more recently in wireless power transfer. The transient in the DC portion of the receiver side is much slower than the AC portion due to larger filter capacitors compared to the resonant capacitors. Feedback control is proposed for the resistor load using lead-lag design. For battery load, the plant contains an unstable zero and feedforward control ZPETC is proposed.

Chapter 6

System Design and Experiment

Fig. 4.5 from Chapter IV shows the whole system overview of the hardware setup. The hardware system constructed supports three transmitters connected in parallel to the inverter via impedance inverter LCL circuit. AC switches are used to activate and deactivate each transmitter. The position of the electric vehicle is sensed by magnetic sensors and each sensor has Zigbee communication unit to communicate with the controller at the transmitter side. The receiver side at the electric vehicle consists of a rectifier to convert the ac power from the receiver to dc power and a dc/dc converter for power control to the battery.

6.1   Vehicle Positioning

Fig. 6.1 shows the vehicle positioning unit. Permanent magnet is installed at the vehicle, and a sensitive magnetic sensor with three axes is installed in between two consecutive transmitters to measure the magnetic field strength. As the magnetic sensors are installed at the same plane as the transmitters, the magnetic field from wireless power transfer only affects the vertical axis. While the permanent magnet moves as the vehicle is moving, the position can be sensed in the horizontal axis by measuring magnetic field strength. Threshold strength is defined and each magnetic sensor is responsible of turning off the previous transmitter and turning on the next transmitter. When the electric vehicle enters the effective area of a sensor defined by the magnetic field threshold, the next transmitter is turned on. When the electric vehicle exits the effective area of the sensor, the previous
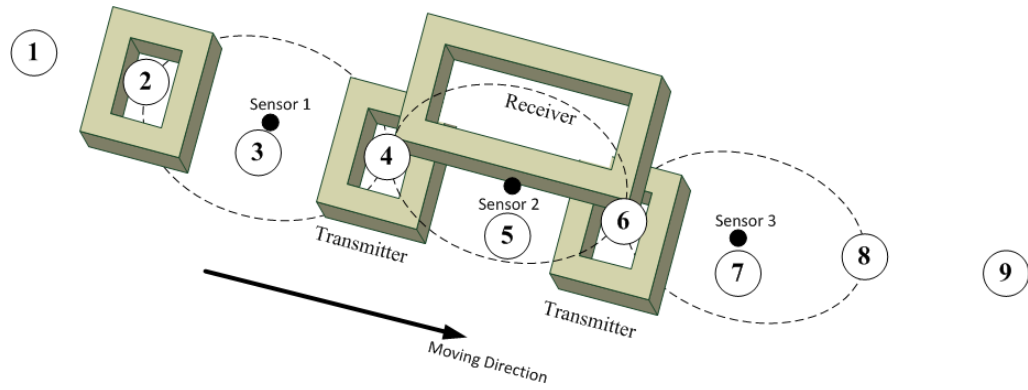
(a)

(b)

Figure 6.1: Vehicle positioning unit: a) block diagram of the configuration, b) experiment setup.
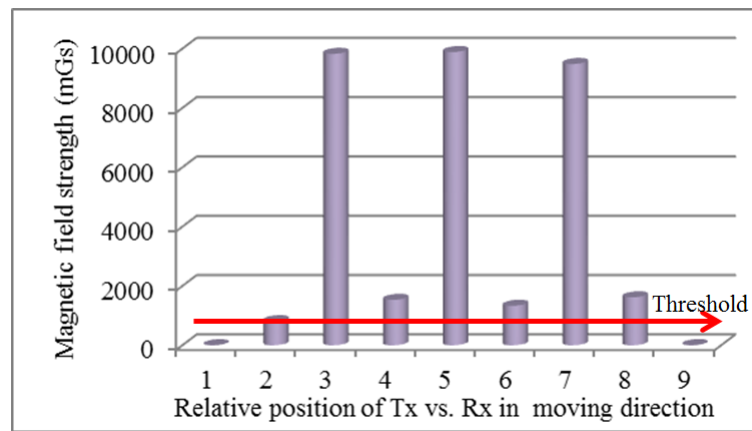
Figure 6.2: Measurement results of magnetic field strength by magnetic sensors in the moving direction.

transmitter is turned off. At the same time, the next sensor is also activated and therefore the third transmitter is turned on.

Considering Fig. 6.1(a), when the EV moves away from the first transmitter and arriving at the center point of the second transmitter. Prior to this, the first and second transmitter are turned on. The magnetic field strength sensed by the magnetic sensor labeled as '1' drop to below defined threshold and the controller turns off the first transmitter. At the same time, the magnetic field strength sensed by the magnetic sensor labeled as '2' increase to above defined threshold and turns on the third transmitter. Each time, only one or two transmitters are activated to achieve balanced magnetic field for wireless power transfer when the vehicle is moving. Fig. 6.2 shows the magnetic field strength measured while the vehicle is moving, the relative positions are labelled in Fig. 6.1(a). The measurement period is 6 ms and the sensitivity of the sensor is 5 mGs.

6.2 Transmitter module

Fig. 6.3 shows the transmitter module. The module consists of a H-bridge inverter, a main control board and three LCL resonators connected in parallel via AC switches. The main controller (ARM STM32VET6) is used to generate four PWM driving signals for the H-inverter. The controller also turns on and off the AC switches using the measurement from
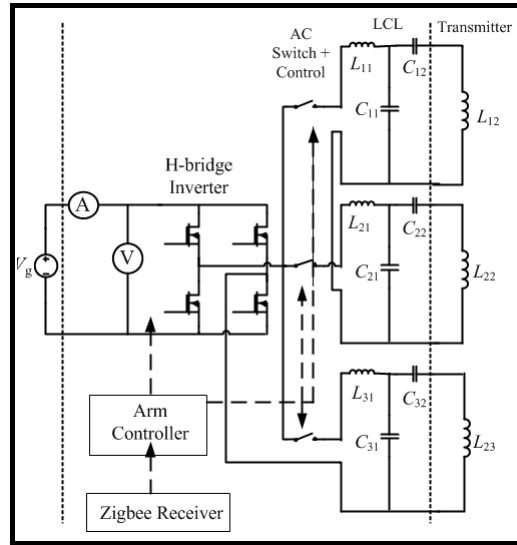
(a)
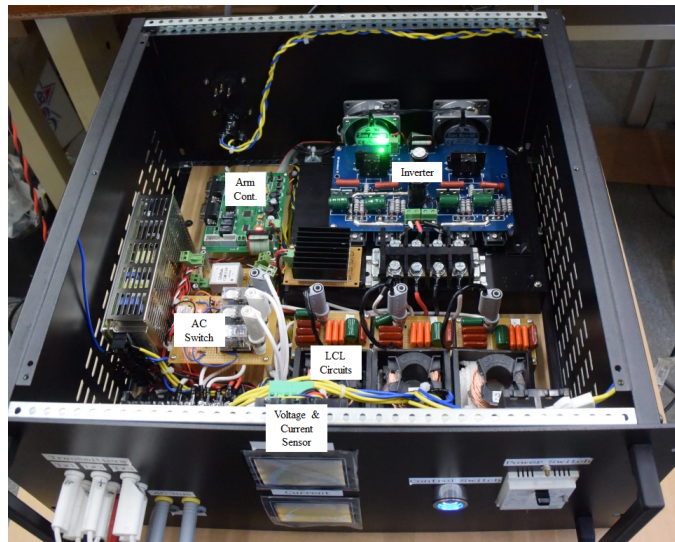
(b)

Figure 6.3: Transmitter module: a) equivalent circuit, b) photo of the actual unit

the magnetic sensors which is transmitted to the controller via Zigbee modules. The values of the components in equivalent circuit in Fig 6.3(a) are given in table 6.1. The high voltage capacitors are from Nippon Chemi-con. The maximum voltage and current specifications for various capacitance can be found in [93]. The dimension of the transmitters is 40 cm X 20 cm and 20 turns.

Table 6.1: Parameters of components in the primary model.

	Value
L_{11}	25 μH
L_{12}	233 μH
L_{21}	25 μH
L_{22}	233 μH
L_{31}	25 μH
L_{32}	233 μH
C_{11}	140 nF
C_{12}	35 nF
C_{21}	140 nF
C_{22}	35 nF
C_{31}	140 nF
C_{32}	35 nF

6.3   Receiver module

Fig. 6.4 shows the receiver module. The module consists of a serial resonant compensation network, a rectifier and a dc/dc converter. The ac power received from the receiver is converted to dc power and a dc/dc converter is installed for power flow control to the battery. The modeling and control to be implemented are described in the previous chapter. The controller is TMS320F28335 DSP. The parameters of the components are given in Table 6.2. The dimension of the receiver is 20 cm X 20 cm and 20 turns.
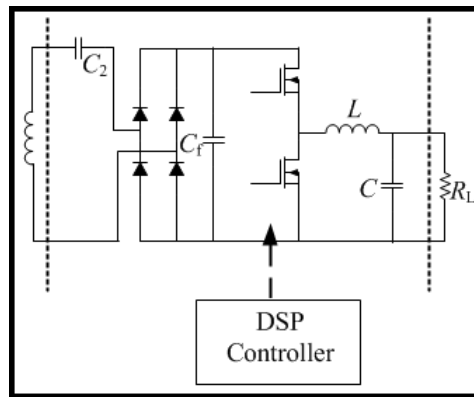
(a)
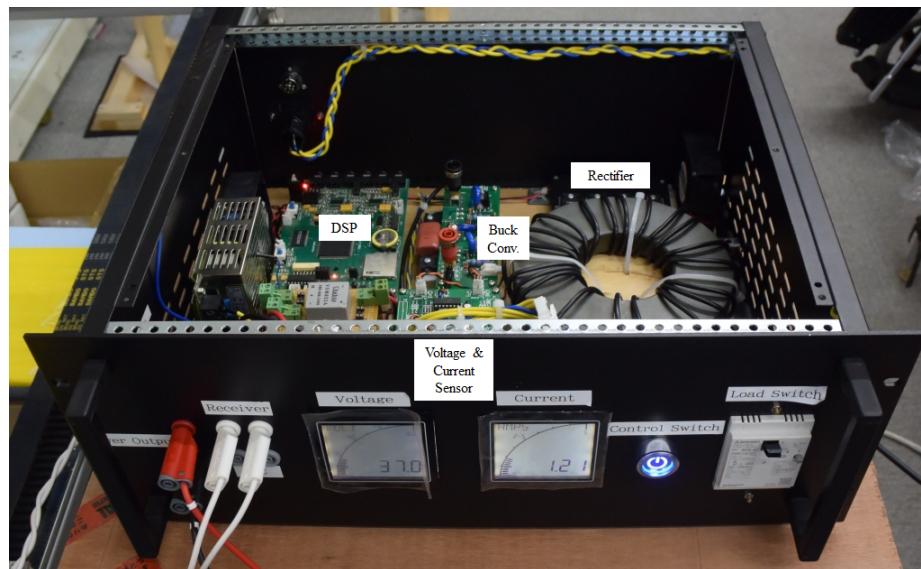
(b)

Figure 6.4: Receiver module: a) equivalent circuit, b) photo of the actual unit

Table 6.2: Parameters of components in the receiver module.

	Value
L_2	233 μH
C_2	15 nF
L	1.72 mH
C	100 μF
C_F	200 μF
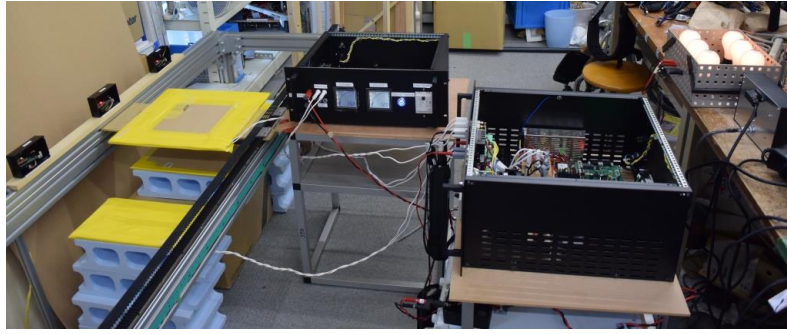
Figure 6.5: Experiment setup.

6.4 Experiment results

Fig. 6.4 shows the whole experiment setup powering light bulb loads. As the receiver is moved across the transmitters, two transmitters are activated simultaneously and the power received by the load is flatten. Fig. 6.6 shows the efficiency and power plot when the receiver is move along from 0 cm point to 70 cm point. The effective resistance including the light bulb, dc/dc converter and rectifier is the maximum efficiency resistance, 15 Ω. The input voltage is 50 V. Lateral position refers to the position of the center of the receiver with respect to the transmitters. The 0 cm point is when the center of the receiver is above the center of the first transmitters.
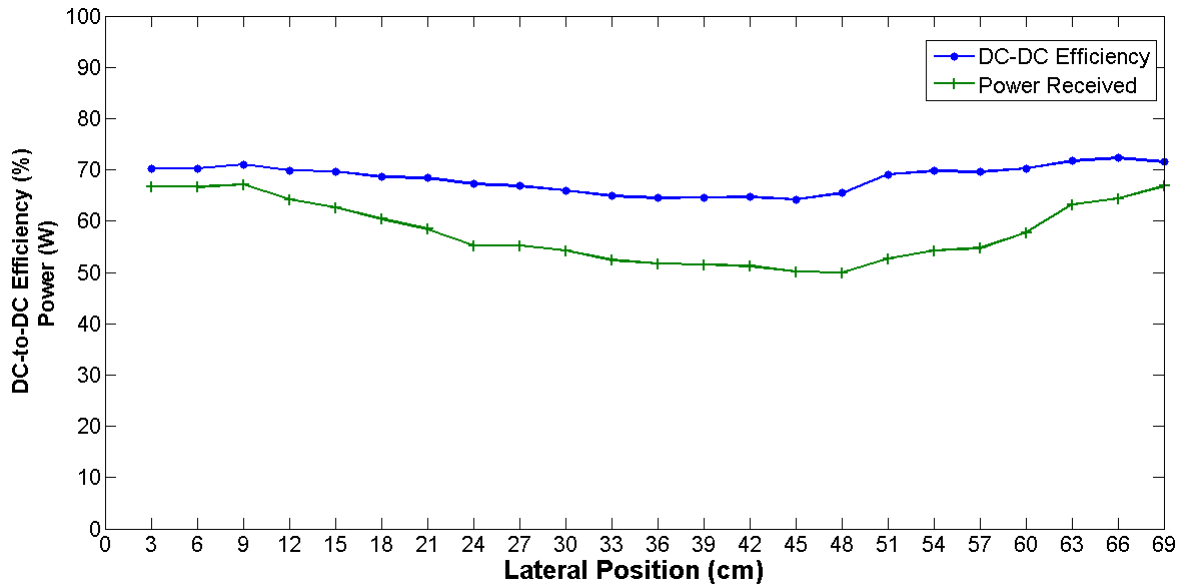
Figure 6.6: Measured power and efficiency vs. lateral position.

6.5 Chapter Summary

The hardware including the transmitter module, receiver module and position sensing module for even magnetic field configurations is built. The measurements from magnetic sensors are sent to the controller and transmitters are turned on only when the vehicle is approaching and turned off when the vehicle is leaving. The dimension and gap are designed such that even magnetic field is achieved. The measurements from along the track shows that the dc/dc efficiency is around 70% and constant power around 65 W is achieved.

Chapter 7

Conclusion

Using resonance and high quality factor coils, magnetic resonant coupling is able to extend from short transfer range of induction to mid-range wireless power transfer. Considerable amount of power can be transferred over a distance few times of the radius of the coils. The system is also robust towards positional shift of the coils. With the increasing use of portable devices and electric vehicles, mid-range wireless power transfer can be implemented to increase convenience of everyday life. Other applications including powering moving robots, implementable medical device, and power supply for sensor network for underground radioactive waste monitoring.

Due to small physical length compared to signal wavelength, the coils in magnetic resonant coupling can be estimated as lumped elements and the whole system is represented by equivalent circuits. However for various applications, powering multiple receivers simultaneously is needed. Furthermore, repeaters may be added to expand the transferable range. As more resonators are added to the system, conventional equivalent circuit equations are complex. In this work, impedance inverter representation of coupling is proposed so that the power transmission path is systematically divided into transfer stages. Coupled resonators can be thought as connected through an impedance inverter in between them.

In multi-receiver case, impedance viewed from transmitter towards each receiver through representative impedance inverter is connected in series. Therefore the power

division ratio is simply equals to the impedance ratio. In transmission path containing repeaters, the impedance is inverted once for each repeater. Combining equations from multi-receiver and repeaters, generalized equation is derived for power division and impedance matching of wireless power transfer consists of arbitrary number of receivers and repeaters. Also, impedance inverter representation simplifies analysis of wireless power transfer of various configurations. Analysis of a dead zone phenomena caused by repeaters where power cannot be transferred to receiver even though the coils are coupled is provided. The phenomenon is then divided into two general cases for arbitrary number of repeaters.

Using derived theory for wireless power transfer as basis, dynamic charging configuration which is using double transmitters is proposed to achieve high efficiency and even magnetic field. The hardware is constructed including the receiver position sensor and automated switching of transmitters as the vehicle move along the charging lane. The experiment is performed using operating frequency of 85 kHz as proposed by Society of Automotive Engineers as the frequency for interoperability. The physical dimension of the transmitter is smaller or up to the size of the receiver as long transmitter lowers the transfer efficiency. Multiple transmitters are connected to a common power source via impedance inverter circuit for cost saving. Method for determining the spacing in between transmitters is also proposed to achieve even magnetic field. Additionally, cross coupling between the transmitters do not affect the designed power level due the LCL impedance inverter circuit.

In the next chapter, the steady state and transient analysis of one-to-one wireless power transfer are discussed. In series-series compensated wireless power transfer, the maximum efficiency depends on both the receiver and transmitter. However the maximum power depends dominantly on the transmitter. This characteristic is exploited to achieve a flatter efficiency curve across different power levels as different power is required when the vehicle is at different moving speeds. A design flow is then proposed using efficiency vs. power level curve. The design method is discussed using round spiral coils and the ac resistance is approximated using extended Dowell formula. However the method can be applied to other coils once the ac resistance calculation method is developed. The transient

of the wireless power transfer is then studied using general state space averaging (GSSA).

Future work of this dissertation:

1. Even magnetic field for vehicles of different sizes.

2. Improved AC resistance calculation for coil designs.

3. Application of the automated coil design method in chapter 5 for proposed even magnetic field configuration.

4. Dynamic configuration design for constant power load.

Bibliography

[1] J. P. Curty, M. Declercq, C. Dehollain, N. Joehl, *Design and optimization of passive UHF RFID systems,* Chapter 2, pp. 2-15, Springer US, 2007.

[2] A. Karalis, J. D. Joannopoulos, and M. Soljacic, "Efficient Wireless Non- Radiative Mid-Range Energy Transfer," *Ann. Phys.*, Vol. 323, No. 1, Jan. 2008, pp. 34-38, doi:10.1016/j.aop.2007.04.017.

[3] A. Kurs et al., Wireless power transfer via strongly coupled magnetic resonances, Sci. Exp., vol. 317, Jul. 2007, pp. 83-86, doi:10.1126/science.1143254.

[4] *The WiTricity Story*. Available: http://witricity.com/technology/the-witricity-story/.

[5] S. Rajagopal, F. Khan, "Multiple receiver support for magnetic resonance based wireless charging," *2011 IEEE Int. Conf. on Communications Workshops (ICC)*, Jun. 2011, pp. 1-5.

[6] Z. N. Low, J. J. Casanova, and J. Lin, "A loosely coupled planar wireless power transfer system supporting multiple receivers," *Adv. Power Electron.*, vol. 2010, pp. 1–13, 2010.

[7] W. Ahn et. al, "Design of coupled resonators for wireless power transfer to mobile devices using magnetic field shaping," IEEE International Symp on Electromagnetic Compatibility (EMC), DOI: 10.1109/ISEMC.2012.6351667, pp. 772 - 776, 2012.

[8] F. Zhang, et al., "In Vitro and In Vivo Studies on Wireless Powering of Medical Sensors and Implantable Devices," *IEEE/NIH Life Science Systems and Applications Workshop (LiSSA 09)*, April 2009, pp. 84-87.

[9] X. Luo, S.Niu, S. L. Ho and W. N. Fu, "A design method of magnetically resonating wireless power delivery systems for bio-implantable devices," *IEEE Trans. Magn.*, vol. 47, no. 10, pp. 3833-3836, Oct. 2011

[10] K. V. Schuylenbergh and R. Puers, *Inductive powering: basic theory and application to biomedical systems,* Springer, 2012.

[11] R. Koma, S. Nakamura, S. Ajisaka, and H. Hashimoto, "Basic analysis of the circuit model using relay antenna in magnetic resonance coupling position sensing system," *2011 IEEE/ASME Int. Conf. Advanced Intelligent Mechatronics (AIM)*, Jul. 2011, pp. 25-30.

[12] B. Griffin, and C. Detweiler, "Resonant wireless power transfer to ground sensor from a UAV," *2012 IEEE Int. Conf. Robotics and Automation (ICRA)*, May 2012, pp. 2660-2665.

[13] C. Nagai et. al., "Electromagnetic Analysis of Wireless Power Transfer for Geological Disposal Monitoring," *2013 Fall Meeting of the Atomic Energy Society of Japan*, pp. 685, 2013. (In Japanese)

[14] V. Jiwariyavej, et. al., "Basic experimental study on effect of bentonite to efficiency of wireless power transfer using magnetic resonance coupling method," *33rd International Telecoommunications Energy Conference (INTELEC 2011)*, DOI: 10.1109/INTLEC.2011.6099772, 2011.

[15] C. Nagai et. al., "Application of wireless power transfer for geological disposal monitoring," *2011 Fall Meeting of the Atomic Energy Society of Japan*, pp. 4, 2011. (In Japanese)

[16] L. Chen, J. T. Boys and G. A. Covic, "Power management for multiple-pickup IPT systems in materials handling applications," *IEEE Journal of Emerging and Selected Topics in Power Electronics*, doi: 10.1109/JESTPE.2014.2316803, pp. 163-176, Apr. 2014.

[17] G. A. J. Elliott, G. A. Covic, D. Kacprzak, and J. T. Boys, "A new concept: Asymmetrical pick-ups for inductively coupled power transfer monorail systems," *IEEE Trans. Magn.*, vol. 42, no. 10, pp. 3389–3391, Oct. 2006.

[18] P. Sergeant and A. Van den Bossche, "Inductive coupler for contactless power transmission," *IET Electr. Power Appl.*, vol. 2, pp. 1–7, 2008.

[19] T. Imura, H. Okabe, and Y. Hori, "Basic experimental study on helical antennas of wireless power transfer for electric vehicles by using magnetic resonant couplings," *IEEE Vehicle Power and Propulsion Conf. (VPPC 09)*, Sep. 2009, pp. 936-940.

[20] T. Hori, "Future vehicle society based on electric motor, capacitor and wireless power supply," *2010 Int. Power Electronics Conf. (IPEC)*, Jun. 2010, pp. 2930-2934.

[21] M. Yilmaz and P. T. Krein, "Review of battery charger topologies, charging power levels, and infrastructure for plug-in electric and hybrid vehicles," *IEEE Trans. Power Electron.*, vol. 28, no. 5, pp. 2151 - 2169, May. 2013.

[22] G. A. Covic and J. T. Boys, "Modern trends in inductive power transfer for transportation applications, "*IEEE Journal of Emerging and Selected Topics in Power Electronics*, doi: 10.1109/JESTPE.2013.2264473, pp. 28-41, Apr. 2014.

[23] A. E. Umenei, "Understanding Low Frequency Non- Radiative Power Transfer," Wireless Power Consortium, Fulton Innovation LLC, Ada, MI, Jun. 2011.

[24] S-H. Lee, and R. D. Lorenz, "Development and validation of model for 95% efficiency, 220 W wireless power transfer over a 30cm air-gap," *2010 IEEE Energy Conversion Congress and Exposition (ECCE)*, Sep. 2010, pp. 885-892.

[25] T. Imura, and Y. Hori, "Maximizing Air Gap and Efficiency of Magnetic Resonant Coupling for Wireless Power Transfer Using Equivalent Circuit and Neumann Formula," *IEEE Trans. Ind. Electron.*, vol. 58, no. 10, pp. 4746-4752, 2011.

[26] W. Zhong, C. K. Lee and S. Y. Hui, "General analysis on the use of Tesla's resonators in domino forms for wireless power transfer," *IEEE Trans. Power Electron.*, vol. 60, no. 1, pp. 261-270, Jan. 2013.

[27] A. Kurs, R. Moffatt, M. Soljacic, "Simultaneous mid-range power transfer to multiple devices," *Appl. Physics Lett.*, vol.96, no.4, pp. 044102-044102-3, Jan. 2010.

[28] J.W. Kim et al., "Analysis of wireless energy transfer to multiple devices using CMT," *2010 Asia-Pacific Microwave Conf. Proc. (APMC)*, Dec. 2010, pp.2149-2152.

[29] B. L Cannon, J. F. Hoburg, D. D. Stancil, and S. C. Goldstein, "Magnetic resonant coupling as a potential means for wireless power transfer to multiple small receivers," *IEEE Trans. Power Electron.*, vol. 24, no. 7, pp. 1819-1825, Jul. 2009.

[30] M. Dionigi, M. Mongiardo, "CAD of EfficientWireless Power Transmission systems," *IEEE MTT-S Int. Microwave Symposium Digest (MTT 11)*, Jun. 2011, pp. 1-4.

[31] I. Awai, T. Komori, "A Simple and Versatile Design Method of Resonator-Coupled Wireless Power Transfer System," *2010 Int. Conf. Communications, Circuits and Systems (ICCCAS)*, Jul. 2010, pp. 616-620.

[32] I. Awai, T. Komori, T. Ishizaki, "Design and experiment of multi-stage resonator-coupled WPT system," *2011 IEEE MTT-S Int. Microwave Workshop Series on Innovative Wireless Power Transmission: Technologies, Systems, and Applications (IMWS)*, pp.123-126, May. 2011.

[33] C. S. Wang, O. H. Stielau, G. A. Covic, "Design considerations for a contactless electric vehicle battery charger," *IEEE Trans. Ind. Elect.*, vol. 52, no. 5, pp. 1308-1314, Oct. 2005.

[34] J. Shin et al., "Design and implementation of shaped magnetic resonance based wireless power transfer system for roadway-powered moving electric vehicles," *IEEE Trans. Ind. Electron.,* 2013.

[35] H. H. Wu, G. A. Covic, J. T. Boys, "Robertson, D.J. A series-tuned inductive-power-transfer pickup with a controllable ac-voltage output," *IEEE Trans. Power Electron.*, vol. 26, no. 1, pp. 98 - 109, Jan. 2011.

[36] H. Irie and H. Yamana, "Immittance converters suitable for power electronics," Electrical Engineering in Japan Electrical Engineering in Japan, vol. 124, no. 2, pp. 53 - 62, Jul. 1998.

[37] H. Irie, N. Minami, H. Minami and H. Kitayoshi, "Noncontact energy transfer system using immittance converter," Electrical Engineering in Japan Electrical Engineering in Japan, vol. 136, no. 2, pp. 58 - 64, Jul. 2001.

[38] C. E Zell and J. G. Bolger, "Development of an engineering prototype of a roadway powered electric transit vehicle system: A public/private sector program," *Proc. IEEE 32nd Vehicular Technology Conf.*, 1982.

[39] SAE International (2013, Nov 14). *SAE International Task Force Announces Agreement on Frequency of Operation and Power Classes for Wireless Power Transfer for its Electric and Plug-In Electric Vehicle Guideline* [online]. Available: http://www.sae.org/

[40] J. Deng, et. al., "Compact and efficient bipolar coupler for wireless power chargers: design and analysis," *IEEE Trans. Power Electron.*, vol 30., no. 11, pp. 6130 - 6140, Nov. 2015.

[41] C. Ma et al., "Wireless Charging of a Supercapacitor Model Vehicle Using Magnetic Resonance Coupling," *ASME 2013 Int. Design Engineering Technical Conferences and Computers and Information in Engineering Conf.*, doi:10.1115/DETC2013-12530.

[42] R. Gehm (2011, Aug 8). *Inductive charging gets green flag* [online]. Available: http://articles.sae.org/10097/

[43] S. Ahn, N. P. Suh, D-H. Cho, "Charging up the road," *IEEE Spectrum*, vol. 50, no. 4, pp. 48 - 54, Mar. 2013.

[44] H. Kohara, "Research trend for EV's in National Institute for Land and Infrastructure Management," *Transactions of the Society of Automative Engineers of Japan,* vol. 130, no. 1, pp. 84-92, 2010. (In Japanese).

[45] M. Kato, "Wireless Power Transfer for Electric Vehicle via Magnetic Resonant Coupling," Ph.D. dissertation, Dept. of Advanced Energy, the University of Tokyo, Kashiwa, Chiba, Japan, 2014. (In Japanese).

[46] S. Lee et al., "On-line electric vehicle using inductive power transfer systems," *2010 IEEE Energy Conversion Congress and Exposition (ECCE)*, pp. 1598-1601, Sep. 2010.

[47] M. Budhia, G. A. Covic, and J. T Boys, "Design and Optimization of Circular Magnetic Structures for Lumped Inductive Power Transfer Systems," *IEEE Trans. Power Electron.*, vol 26., no. 11, pp. 3096-3108, Apr. 2011.

[48] M. L. G. Kissin, G. A. Covic and J. T. Boys, "Estimating the output power of flat pickups in complex IPT systems," *IEEE Power Electronics Specialists Conf.*, pp. 604-610, Jun. 2008.

[49] M. L. G. Kissin, G. A. Covic and J. T. Boys, "Interphase Mutual Inductance in Poly-Phase Inductive Power Transfer Systems,*" IEEE Trans. Ind. Electron.*, vol. 56, no. 7, Jul. 2009.

[50] G. A. Covic, "A past present and future perspective on wireless power transfer for electric vehicles," *2013 IEEE Energy Conversion Congress & Exposition*, invited talk, Denver, Colorado, Sep. 2013.

[51] P. Kotchapansompote et al, "Electric Vehicle Automatic Stop using Wireless Power Transfer Antennas", *The 37th Ann. Conf. of the IEEE Industrial Electronics Society*, pp. 3840-3845, 2011

[52] S. Pakorn, B. M. Nguyen, and H. Fujimoto, "Estimation of Lateral Displacement of Electric Vehicle to Wireless Power Transmitter in Dynamic Charging Scenario", *IEE of Japan Industry Applications Society Conference*, No. 4-5, pp.109-112, 2014.

[53] S. Shin et. al., "Hybrid inverter segmentation control for online electric vehicle," *2012 IEEE Int. Electric Vehicle Conference (IEVC)*, doi: 10.1109/IEVC.2012.6183257.

[54] M. Yilmaz, V. T. Buyukdegirmenci, and P. T. Krein, "General design requirements and analysis of roadbed inductive power transfer system for dynamic electric vehicle charging," *2012 IEEE Transportation Electrification Conference and Expo (ITEC).*

[55]]W. Zhang, S.-C. Wong, C. K. Tse, and Q. Chen, "A study of sectional tracks in roadway inductive power transfer system," in *Proc. IEEE Energy Convers. Congr. Expo.*, Sep. 2011, pp. 822–826.

[56] J. G. Bolger, F. A. Kirsten, and L. S. Ng, "Inductive power coupling for an electric highway system," in *Proc. IEEE Veh. Technol. Conf.*, Mar. 1978, pp. 137–144.

[57] G. A. J. Elliott, J. T. Boys, and A. W. Green, "Magnetically coupled systems for power transfer to electric vehicles," in *Proc. Int. Conf. Power Electron. Drive Syst.*, 1995, pp. 797–801.

[58] G. A. Covic, J. T. Boys, M. Budhia, and C.-Y. Huang, "Electric vehicles—Personal transportation for the future," *World Electr. Veh. J.*, vol. 4, pp. 693–704, Jan. 2011.

[59] Highways England. *Feasibility study: Powering electric vehicles on England's major roads* [online]. Available: http://www.highways.gov.uk/knowledge/publications/1902/.

[60] J. M. Miller et. al., "Demonstrating Dynamic Wireless Charging of an Electric Vehicle," *IEEE Power Electronics Magazine*, vol. 1, no. 1, pp. 12 - 24, Mar. 2014.

[61] L. Chen, G. R. Nagendra, J. T. Boys and G. A. Covic, "Double-Coupled Systems for IPT Roadway Applications," *IEEE Journal of Emerging and Selected Topics in Power Electronics,* vol. 3, no. 1, pp. 37-49, Mar. 2013.

[62] H. Hao, G. A. Covic and J. T boys, "An approximate dynamic model of LCL-T-based inductive power transfer power supplies," *IEEE Journal of Emerging and Selected Topics in Power Electronics*, doi: 10.1109/TPEL.2013.2293138, pp. 5554 - 5567, Nov. 2013.

[63] A. P. Sample, D. A. Meyer, and J. R. Smith, "Analysis, experimental results, and range adaptation of magnetically coupled resonators for wireless power transfer," *IEEE Trans. Ind. Electron.*, vol. 58, no. 2, pp. 544-554, Feb. 2011.

[64] K. E. Koh, T. C. Beh, T. Imura, and Y. Hori "Novel band-pass filter model for multi-receiver wireless power transfer via magnetic resonance coupling and power division," *2012 IEEE 13th Annu. Wireless and Microwave Technology Conf. (WAMI-CON)*, pp. 1-6.

[65] B. L Cannon, J. F. Hoburg, D. D. Stancil, and S. C. Goldstein, "Magnetic resonant coupling as a potential means for wireless power transfer to multiple small receivers," *IEEE Trans. Power Electron.*, vol. 24, no. 7, pp. 1819-1825, Jul. 2009.

[66] T. Imura, "Study on maximum air-gap and efficiency of magnetic resonant coupling for wireless power transfer using equivalent circuit," *IEEE Int. Symp. Ind. Electron. (ISIE 10)*, pp. 3664-3669.

[67] T. Beh, M. Kato, T. Imura, S. OH, and Y. Hori, "Automated impedance matching system for robust wireless power transfer via magnetic resonance coupling," *IEEE Trans. Ind. Electron.*, vol. 60, no. 9, pp.3689-3698, Sep. 2013.

[68] T. Imura and Y. Hori, "Maximizing air gap and efficiency of magnetic resonant coupling for wireless power transfer using equivalent circuit and neumann formula," *IEEE Trans. Ind. Electron.*, vol. 58, no. 10, pp. 4746-4752, Oct. 2011.

[69] S. Cheon et al., "Circuit-model-based analysis of a wireless energy-transfer system via coupled magnetic resonances," *IEEE Trans. Ind. Electron.*, vol. 58, no. 7, pp. 2906-2914, Jul. 2011.

[70] F. Z. Shen, W. Z. Cui, W. Ma, J. T. Huangfu and L. X. Ran, "Circuit analysis of wireless power transfer by "coupled magnetic resonance"," *IET Int. Communication Conf. Wireless Mobile and Computing (CCWMC 2009)*, pp. 602-605.

[71] J. W. Kim, H. C. Son, K. H. Kim and Y. J. Park, "Efficiency analysis of magnetic resonance wireless power transfer with intermediate resonant coil," *IEEE Antennas Wireless Propag. Lett.*, vol. 10, pp. 389-392, May 2011.

[72] N. Oodachi, K. Ogawa, H. Kudo, H. Shoki, S. Obayashi and T. Morooka, "Efficiency improvement of wireless power transfer via magnetic resonance using transmission coil array," *2011 IEEE Int. Symp. Antennas and Propagation (APSURSI)*, pp. 1707 - 1710.

[73] W. Fu, B. Zhang and D. Qiu, "Study on frequency-tracking wireless power transfer system by resonant coupling," *IEEE 6th Int. Power Electronics and Motion Control Conf.*, pp. 2658-2663.

[74] J. Park, Y. Tak, Y. Kim, Y. Kim and S. Nam, "Investigation of adaptive matching methods for near-field wireless power transfer," *IEEE Trans. Antennas Propag.*, vol. 59, no. 5, pp. 1769-1773, May 2011.

[75] T. Imura and H. Yoichi, "Optimization using transmitting circuit of multiple receiving antennas for wireless power transfer via magnetic resonance coupling," *2011 IEEE 33rd Int. Telecommunications Energy Conf. (INTELEC)*, pp. 1-4.

[76] C. Ma, X. Zhu, and M. Fu, "Wireless charging of electric vehicles: A Review and Experiments," in *ASME 2011 Int. Design Engineering Technical Conferences and Computers and Information in Engineering Conf.*, pp. 881-887.

[77] Y. Yokoi, A. Taniya, M. Horiuchi, and S. Kobayashi, "Developement of KW class wireless power transmission system for EV using magnetic resonant method," presented at 1st Int. Electric Vehicle Technology Conference, Yokohama, Japan, 2011.

[78] R. E. Collin, *Foundations for Microwave Engineering,* 2nd ed., NJ:John Wiley and Sons, Inc., 2001.

[79] J. D. Irwin , R. M. Nelms, *Basic Engineering Circuit Analysis.* 10th ed., NJ:John Wiley & Sons, Inc., 2010.

[80] G. L. Matthaei, L. Young, and E. M. T. Jones, *Microwave Filters, Impedance Matching Networks and Coupling Structures*. Norwood, MA: Artech House, 1980.

[81] Z. N. Low, J. J. Casanova, and J. Lin, "A loosely coupled planar wireless power transfer system supporting multiple receivers," *Adv. Power Electron.*, vol. 2010, pp. 1–13, Mar. 2010.

[82] J. W. Kim et al., "Wireless power transfer for free positioning using compact planar multiple self-resonators," *2012 IEEE MTT-S Int. Microwave Workshop Series on Innovative Wireless Power Transmission: Technologies, Systems, and Applications (IMWS),* pp. 127-130, May. 2012.

[83] T. Imura, "Equivalent circuits for repeater antennas used in wireless power transfer via magnetic resonance coupling," *Elect. Eng. Jpn.*, vol. 183, pp. 51-62, doi: 10.1002/eej.22360, Jan 2013.

[84] K. E. Koh, T. C. Beh, T. Imura, Y. Hori., "Multi-receiver and repeater wireless power transfer via magnetic resonance coupling – impedance matching and power division utilizing impedance inverter," The 15th Int. Conf. on Electrical Machines and Systems (ICEMS2012), 2012.

[85] Agilent Technologies (2010) *Agilent E5061B Network Analyzer Help.* Version 2.0. Agilent Techonologies.

[86] K. V. Schuylenbergh and R. Puers, "Inductive powering: basic theory and application to biomedical systems," Springer, 2009.

[87] C. Wang, G. A. Covic and O. H. Stielau, "Power transfer capability and bifurcation phenomena of loosely coupled inductive power transfer systems," *IEEE Trans. Ind. Electron*, vol. 5, no. 1, Feb. 2004.

[88] K. E. Koh, T. C. Beh, T. Imura, and Y. Hori, "Impedance Matching and Power Division Using Impedance Inverter for Wireless Power Transfer via Magnetic Resonant Coupling," *IEEE Trans. Ind. Appl.*, vol. 50, no. 3, pp. 2061-2070, Oct. 2013.

[89] C. R. Sullivan, "Optimal choice for number of strands in a litz-wire transformer winding," *IEEE Trans. Power Electron.*, vol. 14, no. 2, pp. 283-291, Aug. 2002.

[90] T. Kudo, T. Toi, Y. Kaneko and S. Abe, "Contactless power transfer system suitable for low voltage and large current charging for EDLCs," *The 2014 Int. Power Electronics Conf.*, pp. 1109 - 1114, May 2014.

[91] R. P. Wojda, M. K. Kazimierczuk, "Winding resistance of litz-wire and multi-strand inductors," *IET Power Electronics*, vol. 5, no. 2, pp.257-268, Feb. 2012.

[92] R. W. Erickson, *Fundamentals of Power Electronics* 2nd ed., Springer US, 2001.

[93] *Electronic Equipment Film Capacitor HACD Series Data Sheet*, Nippon Chemi-con.

[94] M. Tomizuka, "On the Design of Digital Tracking Controllers," *ASME. J. Dyn. Sys., Meas.*, Control. 1993;115(2B):412-418. doi:10.1115/1.2899081.

Publication

Journal

1. K. E. Koh, T. C. Beh, T. Imura, and Y. Hori, "Impedance Matching and Power Division Using Impedance Inverter for Wireless Power Transfer via Magnetic Resonant Coupling," *IEEE Trans. Ind. Appl.*, vol. 50, no. 3, pp. 2061 - 2070, Oct. 2013.

2. K. E. Koh, T. Imura, and Y. Hori, "Analysis of Dead Zone in Wireless Power Transfer via Magnetic Resonant Coupling for Charging Moving Electric Vehicles," *Int. Journal of Intelligent Transportation Systems Research*, DOI: 10.1007/s13177-015-0110-y, Feb 2015.

Conference (with review)

1. K. E. Koh, T. C. Beh, T. Imura, and Y. Hori, "Novel Band-Pass Filter Model for Multi-Receiver Wireless Power Transfer via Magnetic Resonance Coupling and Power Division," *13th Ann. IEEE Wireless and Microwave Technology Conf. (WAMICON 2012)*, doi: 10.1109/WAMICON.2012.6208428, Apr. 2012.

2. K. E. Koh, T. C. Beh, T. Imura, and Y. Hori, "Impedance Matching and Power Division algorithm Considering Cross Coupling for Wireless Power Transfer via Magnetic Resonance Coupling," *34th Int. Telecommunication Energy Conf. (INTELEC 2012)*, doi: 10.1109/INTLEC.2012.6374468, Sep. 2012.

3. K. E. Koh, T. C. Beh, T. Imura, and Y. Hori, "Multi-receiver and Repeaters Wireless Power Transfer via Magnetic Resonance Coupling – Impedance Matching and Power

136

Division Utilizing Impedance Inverter," *The 15th Int. Conf. on Electrical Machines and Systems (ICEMS 2012)*, Sapporo, Oct. 2012.

4. K. E. Koh, T. Imura, and Y. Hori, "Impedance Inverter based Analysis of Wireless Power Transfer via Magnetic Resonant Coupling for Charging Moving Electric Vehicles," *20th ITS World Congress*, Tokyo, Oct. 2013.

5. K. E. Koh, T. Imura, and Y. Hori, "New Wireless Power Transfer via Magnetic Resonant Coupling for Charging Moving Electric Vehicle," *Int. Electric Vehicle Technology Conf. & Automotive Power Electronics*, Yokohama, 2014.

6. K. E. Koh, K. Song, P. Sukprasert, T. Imura, and Y. Hori, "Two-Transmitter Wireless Power Transfer with LCL Circuit for Continuous Power in Dynamic Charging," I*EEE PELS Workshop on Emerging Technologies: Wireless Power (2015 WoW)*, DOI: 10.1109/WoW.2015.7132851, Jun. 2015.

7. K. Song, C. Zhu , K. E. Koh, T. Imura, and Y. Hori, "Wireless Power Transfer for Running EV Powering Using Multi-Parallel Segmented Rails," *IEEE PELS Workshop on Emerging Technologies: Wireless Power (2015 WoW)*, DOI: 10.1109/WoW.2015.7132808, Jun. 2015.

8. K. Song, K. E. Koh, D. Kobayashi, T. Imura, and Y. Hori, "Modeling and Design of Dynamic Wireless Power Transfer System for EV Applications," *The 41st Annual Conf. of the IEEE Industrial Electronics Society IECON2015*, Nov. 2015.

Book Chapter

1. K. Song, C. Zhu, J. Jiang K. E. Koh, X. Huang, "Dynamic Wireless Power Transfer for In-Motion Electric Vehicles," InTech: Wireless Power. (Accepted)

Others (without review)

1. K. E. Koh, T. Imura, and Y. Hori, "Impedance Inverter based Analysis of Wireless Power Transfer Consists of Repeaters via Magnetic Resonant Coupling," *IEICE Technical Report*, WPT2012-38, Yokosuka, Kanagawa, pp.41-45, 2012